POSITIVE KAON DECAY INTO NEUTRAL PION, POSITRON, AND NEUTRINO RELATIVE BRANCHING RATIO MEASUREMENT IN THE E865 EXPERIMENT AT THE BROOKHAVEN NATIONAL LABORATORY

by

Alexander Sher

Diploma of Higher Education, Novosibirsk State University, Russia, 1992

Submitted to the Graduate Faculty of

School of Arts and Sciences, Physics and Astronomy Department in partial fulfillment

of the requirements for the degree of

Doctor of Philosophy

University of Pittburgh

2002

DISSERTATION ADVISOR:
Prof. Julia A. Thompson

DISSERTATION COMMITTEE MEMBERS:
Prof. Anthony H. Duncan

Prof. Steven Dytman

Prof. Steven Levitan

Prof. Vittorio Paolone

POSITIVE KAON DECAY INTO NEUTRAL PION, POSITRON, AND NEUTRINO RELATIVE BRANCHING RATIO MEASUREMENT IN THE E865 EXPERIMENT AT THE BROOKHAVEN NATIONAL LABORATORY

Alexander Sher, PhD

University of Pittsburgh, 2002

Experiment E865 at the Brookhaven National Laboratory collected about 70,000 $K^+ \to \pi^0 e^+ \nu$(Ke3) events with the purpose of measuring the Ke3 branching ratio relative to the mix of the $K^+ \to \pi^+\pi^0$, $K^+ \to \pi^0\mu^+\nu$, and $K^+ \to \pi^+\pi^0\pi^0$ decays. The obtained result is $BR(K^+ \to \pi^0 e^+ \nu)/KDAL = 0.1998 \pm 0.0008_{stat} \pm 0.0036_{sys}$, where $KDAL = 0.990 \times BR(K^+ \to \pi^+\pi^0) + 0.990 \times BR(K^+ \to \pi^0\mu^+\nu) + 0.995 \times BR(K^+ \to \pi^+\pi^0\pi^0)$. Using the Particle Data Group fit values for the branching ratios in the denominator we can infer $BR(K^+ \to \pi^0 e^+ \nu) = (5.16 \pm 0.02_{stat} \pm 0.09_{sys} \pm 0.04_{norm})\%$. This result is about 3 standard deviations higher than the current Particle Data Group fit of the previous experimental results. The measurement, analysis and result implications for the CKM matrix unitarity are discussed in the thesis.

ACKNOWLEDGEMENTS

First of all, I would like to express my gratitude to Julia Thompson. Her devotion to science and her invaluable advise helped me to stay on the right track all the way through the course of my research. By providing me with the right mix of independence and guidance she helped me to develop my skills as an independent research scientist.

David Kraus taught me a lot about being an experimental researcher. I am sure that the use of his inquisitive and systematic approach will help me in my present and future work.

Mike Zeller was not just the experiment's spokesman, but an endless source of enthusiasm about the high energy physics, and was always there to discuss and advise.

Hong Ma always provided me with a very constructive scientific view of any problem I ever came to his office with. He was an invaluable source of ideas and information.

Andrey Poblaguev and Stefan Pislak were my "next door" people at the Lab. They not only helped me numerous times with my analysis, but were also there for many absolutely not physics related (but absolutely necessary) chats.

Vladimir Issakov and Grisha Atoyan made the transition from Novosibirsk BINP to BNL much easier than it could have been without them.

Don Lazarus was very generous with his knowledge about AGS and life in general. Jim Lowe always brought wonderful coffee from Albuquerque (except for when he arrived directly from Birmingham). Heinz Kaspar's presence at BNL always made routine experiment's tasks much more enjoyable (I am still not sure how).

I would like to thank all the rest of the E865 wonderful crew for making the experiment happen.

I would like to express my special gratitude to my first advisor, Gennadij Fedotovich, who first put me on the track of the experimental high energy physics in 1989 in Novosibirsk.

While all of these people made an invaluable contribution to my work, I would have never finished the thesis without my wife. Ania, your love and trust were what made it possible in the end.

I would like to thank my parents and my grandmother whom I love very much.

Dawn, my friend, I will always miss you living downstairs.

Arie Baratt was and continues to be a good friend. I hope that some day we will be much closer geographically.

I am very grateful to Chris and Fah, who welcomed me in Santa Cruz, and to Sergei for being who he is and making me feel very comfortable in my current research project.

TABLE OF CONTENTS

LIST OF TABLES

LIST OF FIGURES

CHAPTER 1
INTRODUCTION

1.1 Overview

This thesis presents a new high statistics branching ratio measurement of the charged kaon decay $K^+ \to \pi^0 e^+ \nu$ (Ke3) by the E865 experiment at the Brookhaven National Laboratory. Two Ke3 data sets were collected by the E865 experiment: one in 1997 and one in 1998. Because of the reasons described in Chapter 10, we decided to use 1998 data for the final result and to use 1997 data only for a consistency check. Therfore, any reference in this thesis to the E865 Ke3 data means 1998 Ke3 data (unless explicitly specified otherwise).

Knowledge of the Ke3 decay ($K \to \pi e \nu$) branching ratio allows for the derivation of the most precise value of the V_{us} element of the Cabibbo-Kobayashi-Maskawa (CKM) matrix [1, 2].

The CKM matrix unitarity test as it relates to the elements of the first row disagrees with unitarity by ≈1.5-3 standard deviations (depending on the value of the V_{ud} element used). The most recent $K^+ \to \pi^0 e^+ \nu$ branching ratio measurement was done in 1987 [5] with all the previous ones performed around 1970. The largest statistics in any single measurement was about 4,000 events. The Particle Data Group fit gives $B.R.(K^+ \to \pi^0 e^+ \nu) = (4.82 \pm 0.06)\%$ [2].

1.2 Standard Model and CKM Matrix Unitarity [3],[4]

The Standard Model of elementary particle physics has been very successful in describing and predicting the experimental results obtained to date. In the Standard Model, the fundamental forces arise from the local gauge symmetries. Vector fields (massless bosons) are introduced in order to preserve the invariance of the theory under local gauge transformations and become the "carriers" of the corresponding force. While the carriers of the electromagnetic force (photons) and the strong force (gluons) are indeed believed to be massless, the electroweak bosons' ($W^\pm$ and Z^0) masses are introduced through the Higgs mechanism; two groups forming electroweak symmetry ($SU_L(2)$ and $U_Y(1)$) are broken separately and give rise to the masses of

$W^{\pm}$ and Z^0 respectively. At the same time, the product $SU_L \times U_Y(1)$ retains the symmetry $U_Q(1)$ which allows for the photon to stay massless. Different fermion masses are generated by different strength Yukawa couplings of different fermions to the Higgs field.

Before the discovery of c (charm) quark in 1974, the observed suppression of the strangeness changing decays led to Cabibbo theory; the d quark present in electroweak currents was declared to be really a mix of mass eigenstates of d and s quarks.

$$d' = d\cos\theta_C + s\sin\theta_C \tag{1.1}$$

where the Cabibbo angle θ_C is small ($\approx 13^o$). While successful in predicting many measured decay rates, Cabibbo theory predicted the value of the $K^0 \to \mu^+\mu^-$ decay rate to be much larger than the experimentally observed limit.

A solution to this discrepancy was proposed in 1970 by Glashow, Iliopoulos, and Maiani (GIM). The so called GIM mechanism predicted existence of the fourth quark c (charm) that formed weak isospin doublet with the s quark. The lower components of the two doublets (u,d') and (c,s') were related to their mass eigenstates d and s by the orthogonal transformation defined by Cabibbo matrix:

$$\begin{pmatrix} d' \\ s' \end{pmatrix} = \begin{pmatrix} \cos\theta_C & \sin\theta_C \\ -\sin\theta_C & \cos\theta_C \end{pmatrix} \begin{pmatrix} d \\ s \end{pmatrix} \tag{1.2}$$

The introduction of the charm quark led to the additional amplitudes in the $K^0 \to \mu^+\mu^-$ decay that removed the discrepancy between the observed and predicted $K^0 \to \mu^+\mu^-$ decay rate. The GIM mechanism was astonishing in that it predicted the charm quark four years before any experimental confirmation of its existence.

The important implication was that we have to make a distinction between weak interaction eigenstates (d') that enter interactions and mass eigenstates (d) that have definite mass through the Higgs mechanism.

When all known fermions (quarks and leptons) are considered, their weak interaction eigenstates describe the gauge invariant theory. The fermionic mass matrices can be diagonalized in the mass eigenstate basis which relates to the weak eigenstate basis by unitary transformation. As a result, the weak eigenstates of quarks are presented as a mixture of their mass eigenstates. The mixing can be limited to either u type or d type quarks but customarily it is chosen to have d, s and b quarks mixed, while u, c and t quarks remain unmixed.

$$\begin{pmatrix} d' \\ s' \\ b' \end{pmatrix} = \begin{pmatrix} V_{ud} & V_{us} & V_{ub} \\ V_{cd} & V_{cs} & V_{cb} \\ V_{td} & V_{ts} & V_{tb} \end{pmatrix} \begin{pmatrix} d \\ s \\ b \end{pmatrix} \tag{1.3}$$

The unitary matrix in Equation 1.3 was introduced by Kobayashi and Maskawa and is referred to as Cabibbo-Kobayashi-Maskawa(CKM) matrix.

It is important to note that while the CKM matrix describes mixing in the quark sector, the assumption of zero neutrino mass results in the analogous matrix for the lepton sector to be equal to one and consequently in the absence of any mixing between different lepton generations. In the face of recent experimental results [6][7], the assumption of the zero neutrino mass becomes less valid and is a subject of much experimental effort.

Parameters of the CKM matrix have to be determined experimentally and any observed deviation from the matrix's unitarity would either undermine the validity of the Standard Model or indicate the existence of a fourth generation of fermions. For a 3×3 matrix, there are nine unitarity constraints. In this thesis, I will talk about one constraint that involves only the first row elements:

$$|V_{ud}|^2 + |V_{us}|^2 + |V_{ub}|^2 = 1 \tag{1.4}$$

The current values of the first row CKM matrix elements are:

$$\begin{aligned} |V_{ud}| &= 0.9740 \pm 0.0005 \\ |V_{us}| &= 0.2196 \pm 0.0023 \\ |V_{ub}| &= 0.0036 \pm 0.0010 \end{aligned} \tag{1.5}$$

The V_{us} value was derived from Ke3 decays [1, 2]. The value of the V_{ud} is obtained from nuclear superallowed Fermi beta decays [8]. V_{ub} is determined from the semileptonic decays of B mesons [2] and due to its small value has negligible effect on the unitarity test (1.4).

Using the values from (1.6) we obtain:

$$|V_{ud}|^2 + |V_{us}|^2 + |V_{ub}|^2 = 0.9969 \pm 0.0014 \tag{1.6}$$

The result is different from unity by 2.2 standard deviations. If we follow the suggestion of the Particle Data Group [2] and increase the error of V_{ud} from 0.0005 to 0.0010, the discrepancy with unitarity decreases to 1.4 standard deviations.

It is important to note that the result of this test depends strongly on the choice of the V_{ud} value used. Table 1.1 shows how the deviation from unity of the left side of Equation 1.4 varies with the value of the V_{ud} element.

Table 1.1: Deviation from unity (δ) of the sum of the squares of the first row elements of the CKM matrix for different values of the V_{ud} element. First two rows correspond to the two different estimates of the uncertainty of the V_{ud} value obtained from the Nuclear beta decays.

$\|V_{ud}\|$ value	Obtained from	δ
0.9740 ± 0.0005	Superallowed Nuclear Beta Decays [8]	$(3.1 \pm 1.4) \times 10^{-3}$
0.9740 ± 0.0010	Superallowed Nuclear Beta Decays [2]	$(3.1 \pm 2.2) \times 10^{-3}$
0.9728 ± 0.0012	Neutron Decays Average [2]	$(5.4 \pm 2.5) \times 10^{-3}$
0.9735 ± 0.0012	Neutron and Beta Decays Average [2]	$(4.1 \pm 2.5) \times 10^{-3}$
0.9713 ± 0.0013	New Neutron Decays Result [9]	$(8.3 \pm 2.7) \times 10^{-3}$

While we can not say that the test (1.6) shows a definite discrepancy with unitarity, its results are certainly provocative and call for some resolution. While experimental and theoretical effort to determine the value of V_{ud} continues (the result from the last row of the Table 1.1 was published in 2002), the value of V_{us} listed by the Particle Data Group was obtained in 1984[1] and while theoretical contributions to it were reevaluated recently [11],[12], there was no new experimental input on the Ke3 branching ratio. Taking into account that the contribution of the uncertainty in V_{ud} to the uncertainty of the unitarity sum becomes comparable (equal if we take the V_{ud} value from [8]) to the contribution from the V_{us} uncertainty, a new determination of the V_{us} value might provide an additional insight.

Theoretical and experimental aspects of the V_{us} determination are discussed in the following section.

1.3 V_{us} element and $K^+ \to \pi^0 e^+ \nu$(Ke3) decay

The value of the V_{us} element can be determined from hyperon decays and from $K \to \pi e \nu$ (Ke3) decays. The important difference between the two is that while both axial and vector currents are present in hyperon decays, only the vector current contributes to the Ke3 decays. Theoretical input to the V_{us} calculation can be divided into two parts: vector and axial couplings between hadronic states and radiative corrections. In the limit of SU(3) symmetry, the vector current hadronic coupling can be described by Clebsch-Gordan coefficients, while the vector-axial current includes two empirical parameters. In addition, the Amodello-Gatto [10] theorem states that the effects of the SU(3) symmetry breaking are suppressed to the second order for vector currents; there is no such suppression for axial currents. This gives a smaller theoretical uncertainty to the determination of the V_{us} value from pure vector current processes (such as Ke3).

Both charged and neutral kaons can decay into pion, electron/positron, and neutrino; the neutral and charged Ke3 decays are both used for the V_{us} value determination. In the E865 experiment only charged Ke3 decay was detected; therefore any reference in this thesis to the Ke3 decay is the reference to the charged Ke3 decay (unless noted otherwise)

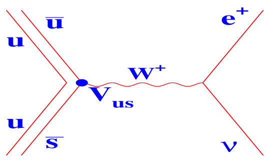

Figure 1.1: Ke3 decay diagramm

The matrix element of the Ke3 decay (without radiative corrections) is

$$M = \frac{G_F}{\sqrt{2}} V_{us} \frac{1}{\sqrt{2}} \left(f_+(t) \left[(P_K + P_\pi)_\mu \bar{e} \gamma_\mu (1+\gamma_5) \nu \right] + f_-(t) \left[m_e \bar{e} \gamma_\mu (1+\gamma_5) \nu \right] \right) \qquad (1.7)$$

where G_F is the weak coupling constant, P_K and P_π are four-momenta of the kaon and the pion, $t = (P_K - P_\pi)^2$, and $f_\pm(t)$ are vector form-factors that originated from the hadronic current and are conventionally parameterized as $f_\pm(t) = f_\pm(0)(1 + \lambda_\pm(t/m_\pi^2))$.

Since the term with f_- is proportional to the electron mass, it is negligible in the Ke3; this is not the case for the Kμ3 decay.

As a result, the Ke3 decay rate is proportional to

$$d\Gamma(K \to \pi e \nu) \propto |V_{US}|^2 \times |f_+(0)|^2 \times [1 + \lambda_+ \left(\frac{t}{m_\pi^2} \right)]^2 dt \qquad (1.8)$$

where the three contributions are uncorrelated. The relative uncertainty of the V_{us} value determined from the Ke3 decay rate can be expressed as

$$\sigma_{|V_{US}|} = |V_{US}| \left[\pm 0.5 \frac{\sigma_\Gamma}{\Gamma} \pm 0.047 \frac{\sigma_{\lambda_+}}{\lambda_+} \pm \frac{\sigma_{f_+(0)}}{f_+(0)} \right] \tag{1.9}$$

In Equation 1.9, the error associated with the correct theoretical calculation and application to the experimental result of the radiative corrections is convoluted into the uncertainty of the decay rate. Radiative corrections were reevaluated recently in the framework of chiral perturbation theory [12].

The value of the vector form-factor slope λ_+ is obtained empirically. Two very recent experiments [15],[16] performed new measurements of this slope. Their results are consistent both with each other and with the previous measurements; they also excluded a previous indication [13] of tensor and scalar contributions, not allowed by the Standard Model. The $f_+(0)$ is calculated theoretically in the framework of the Chiral Perturbation Theory. New calculation of this parameter to the full order p^6 CHPT is underway [11].

Table 1.2 shows the most accurate experimental data on the $K^+ \to \pi^0 e^+ \nu$ branching ratio.

Table 1.2: The most accurate experimental data on the branching ratio of the $K^+ \to \pi^0 e^+ \nu$ decay.

Measured	Result	$\Gamma(Ke3)/\Gamma_{tot}$	N Ke3	Year
$\Gamma(Ke3)/\Gamma(\pi^+\pi^+\pi^-)$	0.850 ± 0.019 [17]	4.75 ± 0.1	4385	1971
$\Gamma(Ke3)/\Gamma_{tot}$	4.86 ± 0.1 [35]	4.86 ± 0.1	3516	1972
$\Gamma(Ke3)/\Gamma(\pi^+\pi^0)$	0.221 ± 0.012 [18]	4.67 ± 0.25	786	1973
$\Gamma(Ke3)/\Gamma(\pi^+\pi^+\pi^-)$	0.867 ± 0.027 [5]	4.85 ± 0.15	2768	1987

Particle Data Group fit to all K^+ decay data yields

$$BR(K^+ \to \pi^0 e^+ \nu) = (4.82 \pm 0.06)\% \tag{1.10}$$

Table 1.3 summarizes different contributions to the uncertainty of the V_{us} element.

As different experiments that contributed to the fitted Ke3 decay rate treated radiative corrections in different ways, the error due to the radiative corrections is not included in the Table 1.3 and is equal $\approx 0.5\%$ as estimated in [1].

As shown in Table 1.4, the Ke3 branching ratio required by the CKM matrix unitarity is at least 5% different from the current PDG fit. While $f_+(0)$ should be recalculated theoretically, a new high statistics measurement of the Ke3 branching ratio with consistent treatment of the radiative corrections should be an integral part

Table 1.3: Summary of different contributions to the error of the V_{us}. For decay rate and form-factor slope, the uncertainties were taken from the PDG fits. $f_+(0)$ uncertainty was taken from [12].

Source of uncertainty	$\sigma(X)/X$	Contribution to $\sigma(V_{us})/V_{us}$
Decay rate	1.2%	0.6%
Form-factor slope λ_+	9.6%	0.45%
Form-factor at zero momentum transfer $f_+(0)$	0.85%	0.85%

of the effort to resolve the CKM first row unitarity test.

Table 1.4: Table shows the relative (compared to the current PDG fit) Ke3 branching ratio calculated assuming CKM matrix unitarity and following prescription of [1]. Errors are connected with the uncertainty of the V_{ud} value used and of the $f_+(t)$ form-factor slope, and its value at the zero momentum transfer.

$\lvert V_{ud}\rvert$ value	Obtained from	$\frac{BR(Ke3)_{CKM}}{BR(Ke3)_{PDG}}$
0.9740 ± 0.0005	Superallowed Nuclear Beta Decays [8]	(1.053 ± 0.027)
0.9740 ± 0.0010	Superallowed Nuclear Beta Decays [2]	(1.053 ± 0.044)
0.9728 ± 0.0012	Neutron Decays Average [2]	(1.101 ± 0.052)
0.9735 ± 0.0012	Neutron and Beta Decays Average [2]	(1.073 ± 0.052)
0.9713 ± 0.0013	New Neutron Decays Result [9]	(1.161 ± 0.056)

1.4 Outline of the experimental goal

In the light of the discussion in the previous section, it was decided to perform a new high statistics Ke3 branching ratio in the E865 experiment at Brookhaven National Laboratory AGS. The E865 detector resided in a 6GeV/c unseparated beam containing about 10^7 K^+, 2×10^8 π^+ and 1.7×10^8 protons per 2.8 second AGS pulse. The detector was designed to search for the decay $K^+ \to \pi^+\mu^+e^-$ and detected all kaon decay modes containing at least three charged particles in the final state. The major kaon decay modes are listed in Table 1.5. The $K^+ \to \mu^+\nu$ decay was the only major decay not detected by the E865 experiment. The π^0 was detected through $\pi^0 \to e^+e^-\gamma$ ($B.R. = 0.0198 \pm 0.00032$ [2]). Since the E865 experiment did not measure the kaon flux, only a relative Ke3 branching ratio measurement was possible.

Table 1.5: Kaon decay modes (and their branching ratios [2]) that account for 99.99% of its total decay rate. These modes with the exception of the $K^+ \to \mu^+\nu$ decay were detected by the E865 experiment. π^0 in the final state was detected through the $\pi^0 \to e^+e^-\gamma$ decay.

Decay	B.R.
$K^+ \to \mu^+\nu$	$(63.51 \pm 0.18)\%$
$K^+ \to \pi^+\pi^0$	$(21.16 \pm 0.14)\%$
$K^+ \to \pi^+\pi^+\pi^-$	$(5.59 \pm 0.05)\%$
$K^+ \to \pi^+\pi^0\pi^0$	$(1.73 \pm 0.04)\%$
$K^+ \to \pi^0\mu^+\nu$	$(3.18 \pm 0.08)\%$
$K^+ \to \pi^0e^+\nu$	$(4.82 \pm 0.06)\%$

I decided to measure the Ke3 branching ratio relative to the sum of the three other major kaon decay modes containing π^0 in the final state. The use of these decays reduced the possible particle detection and identification systematic uncertainties and eliminated the error connected with the experimental uncertainty of the B.R.($\pi^0 \to e^+e^-\gamma$). Thus, my purpose was to measure the following quantity:

$$\frac{BR(K^+ \to \pi^0 e^+\nu)}{Kdal} = \frac{N_{Ke3}/Acc^{Ke3}}{N_{Kdal}/Acc^{K\pi2}} \tag{1.11}$$

where

$$\begin{aligned} Kdal = \quad & BR \quad (K^+ \to \pi^+\pi^0) \\ +(Acc^{K^+\to\pi^0\mu^+\nu}/Acc^{K^+\to\pi^+\pi^0})\times \quad & BR \quad (K^+ \to \pi^0\mu^+\nu) \\ +(Acc^{K^+\to\pi^+\pi^0\pi^0}/Acc^{K^+\to\pi^+\pi^0})\times \quad & BR \quad (K^+ \to \pi^+\pi^0\pi^0) \end{aligned} \tag{1.12}$$

N_{Ke3} and N_{Kdal} are the number of data events for the signal and normalizer respectively, and Acc^{PROC} is the total acceptance for the decay mode $PROC$. The ratios of acceptances were close to one.

Signal (Ke3) and normalizer (Kdal) can be separated on an event by event basis using particle identification (separation of electrons from pions and muons) alone. Full reconstruction of the π^0 provided a valuable test of the result's stability as well as an estimate of the background.

$K^+ \to \pi^+\pi^+\pi^-$ events used for calibration can be selected using kinematics requirements alone.

CHAPTER 2
EXPERIMENT E865

The E865 experiment began taking data in 1994 and finished in the end of 1998, and was designed primarily to search for the Lepton Flavor Number violating decay $K^+ \to \pi^+\mu^+e^-$. This search defined the experiment design. As this thesis is not connected with the $K^+ \to \pi^+\mu^+e^-$ measurement, I will leave out the discussion of the detector overall design and of the particular requirements on its parameters implied by the $K^+ \to \pi^+\mu^+e^-$ search. Such discussion can be found in [19],[20]. The experimental setup was also extensively described in [21].

2.1 The E865 Detector overview

The elevation view of the E865 detector with a simulated $K^+ \to \pi^+\mu^+e^-$ event is presented in Figure 2.1.

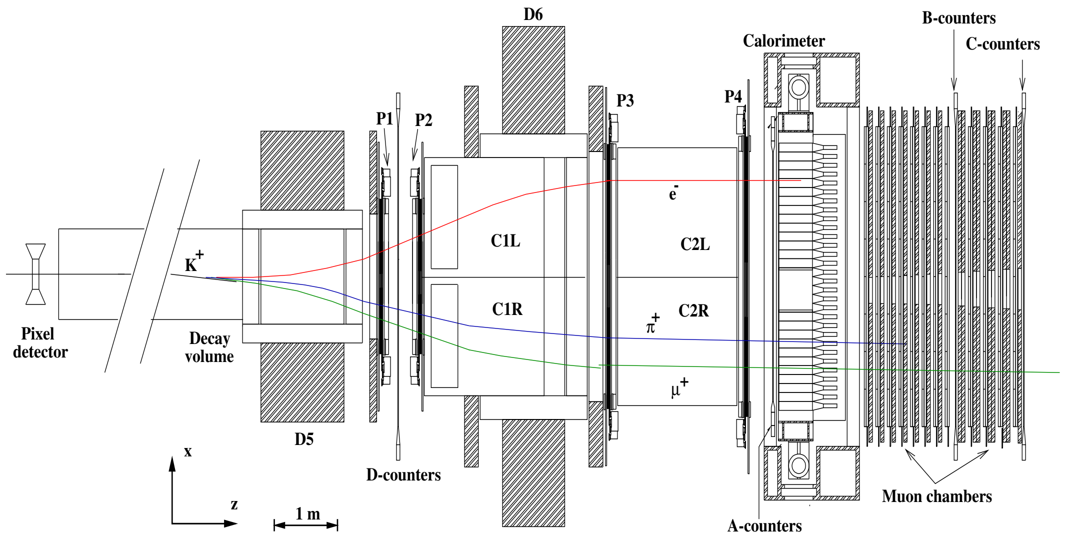

Figure 2.1: Elevation view of the E865 detector with the simulated $K^+ \to \pi^+\mu^+e^-$ event

The detector was located in the specially designed A2 beam line[21] that delivered the 6GeV/c unseparated kaon beam. For the Ke3 data taking, the beam flux was approximately 10^7 K^+, 2×10^8 π^+, and 2×10^8 protons per 2.8 second pulse. A 5m-long decay volume was evacuated to about 1μ of mercury, and provided for a sufficiently low probability of beam interactions (about 10^{-9} of a nuclear interactions length). Downstream of the decay volume a dipole magnet (D5) separated the particle trajectories by charge with negative particles going mostly to the left and positive to the right side of the apparatus. It also steered the decay products away from the dead region that was left in all of the detector elements for the passage of the beam.

The spectrometer, used to determine decay product momenta and trajectories, consisted of four proportional wire chambers (P1-P4) and a second dipole magnet (D6) with 0.833Tm field integral.

The particle identification system consisted of the following three parts:

1. Two large threshold Cerenkov counters (C1 and C2) filled with CH_4 at atmospheric pressure with 8 and 32 photomultipliers(PMTs) respectively in C1 and C2 counters. Each Cerenkov counter was divided into two (left and right) parts providing for the independent particle identification of the positive and negative tracks and allowing different gases to be used on the left and the right sides (a feature not used for the Ke3 data collection). The Cerenkov energy thresholds in CH_4 are about ($16.8MeV$; $3.5GeV$; $4.7GeV$) for electron, muon and pion respectively.

2. An electromagnetic calorimeter of the Shashlik design [25]. The calorimeter consisted of 600 modules (11.4cm by 11.4cm by 15 radiative lengths each) assembled in a 30x20 array.

3. A muon system, consisting of 24 planes of proportional tubes interspaced by iron plates.

Using these systems, an electron was identified as a track that left a signal in the Cerenkov counters and had energy deposition in the calorimeter consistent with its momentum. A pion should have no signal in the Cerenkov counters and should have energy deposition in the calorimeter consistent with that of a minimum ionizing particle or a hadron shower. A muon should have a signal in the muon system, minimum ionizing deposit in the calorimeter and no signal in the Cerenkov counters.

Four scintillator hodoscope arrays (A, B, C and D HOD) were available for trigger purposes.

A pixel hodoscope was installed upstream from the vacuum decay volume only during the 1997 run period and combined with the coordinate of the decay vertex was used to determine the direction of the kaon.

2.2 The Spectrometer

2.2.1 Magnets

The first dipole magnet (D5) was used to steer the decay products away from the dead region of the detector left for the passage of the beam; it also separated particles by charge. The D5 magnet had a 48 inch wide horizontal aperture and 24 inch vertical gap. The depth (along the beam axis) of the magnet was 48 inches. The D5 field provided a 240Mev/c horizontal momentum kick.

The second dipole (D6) served as a spectrometer magnet. It had a size of (120×36) inch^2 (width$\times$depth) with a vertical gap of 50 inches and provided 255Mev/c horizontal momentum kick opposite in direction from the one provided by the D5 magnet.

Measurement of the magnetic field map of both dipoles is described in Section 5.2.

2.2.2 Proportional Wire Chambers

Four proportional wire chambers (PWCs) were used (in conjunction with the D6 magnet) to determine momentum and trajectory of the kaon decay products. Multi-wire proportional wire chambers were chosen over drift chambers because of the high expected rate (about 50MHz of secondary particles passing through the active regions of the chambers during the standard running conditions).

Each PWC had four sensitive planes in order to have enough redundancy for the unambiguous location of the hit in the high rate environment and to lessen the effects of chamber inefficiencies. Wire spacing was chosen to be 2mm as a trade-off between spatial resolution and mechanical and electrostatic limitations. The sizes of the four chambers are presented in the Table 2.1.

Table 2.1: Total and dead region areas of the four proportional wire chambers. Areas are given in horizontal times vertical dimensions.

	P1	P2	P3	P4
Total area	$160\times 80cm^2$	$160\times 80cm^2$	$300\times 140cm^2$	$320\times 160cm^2$
Dead area	$19\times 9cm^2$	$30\times 10cm^2$	$55\times 16cm^2$	$70\times 26cm^2$

Each chamber consisted of four wire planes with wires in vertical, horizontal and $\pm19.4^o$ inclined with respect to the vertical direction. Figure 2.3 shows schematically the order of assembled wire, cathode and ground plates.

The anodes (20μm diameter gold-plated tungsten wires) and the high voltage planes (50μm mylar coated by 40μm graphite) were supported on the outer edges by G10 frames. Each of the H.V. planes was divided into four areas (Figure 2.2). Dead zones had lowered high voltage on them to quench the signal from the beam passage area (≈2GHz rate).

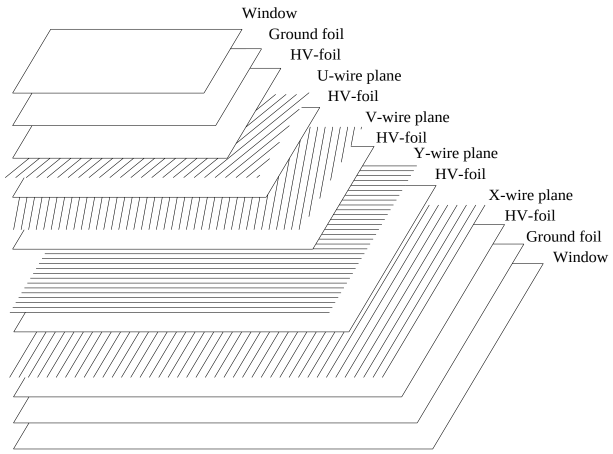

Figure 2.2: PWC cathode plane design. Dead zones correspond to the place where the beam passed and the cathode planes were kept at lower voltage.

Outer H.V. planes were followed by ground planes to equalize the electrostatic attraction between outer H.V. planes and outer anode planes. Gas windows (17μm mylar and 17μm aluminum pressed together) complete the outer layer. Rubber O-rings along the G10 frames were used to make the assembled chamber air-tight.

In order to have a sufficiently short readout gate (preferably of the order 20ns), the gas in the chambers should have high electron drift velocities combined with a high ion mobility. Aging properties of the gas were also important. The thin windows (to reduce multiple scattering) required gas at atmospheric pressure. With all of these considerations taken into account, a 50%:50% mixture of CF_4:isobutane was used in P1/P2; a 79.5%:20%:0.5% mixture of argon/isobutane/CF_3Br was chosen for P3/P4 in order to reduce electrostatic forces between planes in these larger chambers, allowing a lower operation voltage.

The PWC readout system (PCOS4) was custom made [22]; signal amplifiers, discriminators, controlled delay lines and a coincidence scheme with an external gate were put on the readout cards connected directly to the chambers. Each card read out information from 16 wires. Each group of 16 cards were connected in daisy-chain to a common motherboard. Control and connection between mother-boards and the

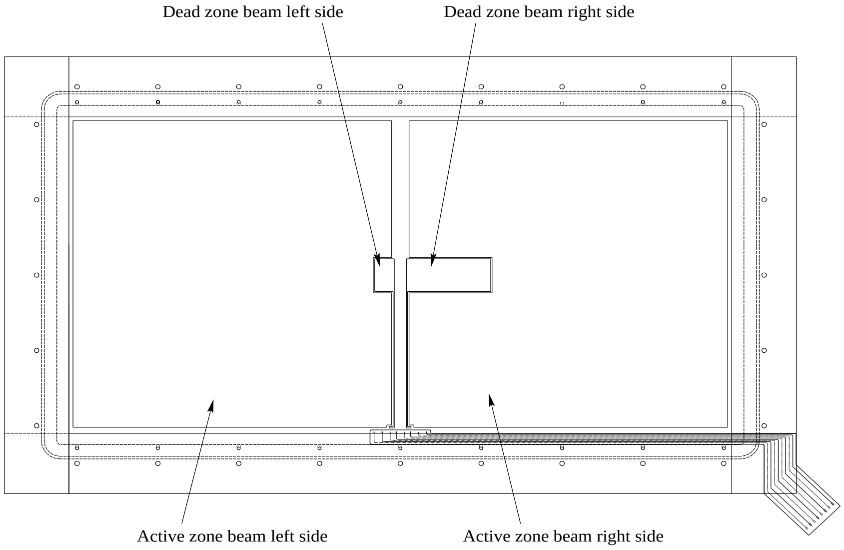

Figure 2.3: Schematic cross-section of the PWC showing wire, high voltage, ground and gas window planes.

data acquisition system was accomplished through LeCroy Camac modules.

2.3 Particle Identification

2.3.1 Cerenkov Counters

Threshold Cerenkov counters played a crucial role in e^+/e^- identification, and pion/muon rejection required for the $K^+ \rightarrow \pi^+\mu^+e^-$ search. The counters were designed, constructed, and maintained by the University of Pittsburgh part of the E865 collaboration.

David Kraus conceived the design and supervised the construction, PMT selection and studies, gas system, overall installation, and testing. Julia Thompson did the detailed optical design, supervised construction, installation, and alignment of the optics as well as managing the monitoring and early analysis. Research associates David N. Brown (construction, optics and early analysis), Christoph Felder (magnetic shielding, optics and monitoring), Robin Appel (monitoring, simulation code), Naipor Cheung (monitoring, calibration and optics), and Peter Lichard (monitoring, code development, analysis) all made substantial contributions. Graduate researcher H.M. Gach did early PMT tests and participated in early running and monitoring. High school teacher Ivan Ober (construction, monitoring, PWC studies) and several undergraduates contributed to the construction and optics. The contributions of some (optics: Elizabeth Battiste, Tim Stever, Cindy Miller; construction: Tuan Lu, John Hotmer; and PMT tests and optics:M. Nickelson) were substantial enough to be credited in the detector instrumentation paper[21].

I joined the group in 1995, and participated in early tests of the Cerenkov counter. I took over the PMT testing from H. Michael Gach, and participated in running and monitoring during the bulk of the E865 runs. With the support of Kraus and Thompson I proposed the Ke3 run, developed the special trigger and running conditions for that run, over-saw the run itself, and developed an independent analysis chain (within the E865 analysis framework) including independent assessment of the Cerenkov efficiencies.

Design considerations

The design goals for each of the Cerenkov counters were:

- Less than 0.2% probability of π^-/μ^- misidentification as e^-; high e^- identification efficiency.
- High (at least 98%) e^+ identification efficiency, to avoid e^+ misidentification as π^+/μ^+; insensitivity to π^+/μ^+ originating from beam kaon decays (momentum range of up to $\approx$3.4GeV/c).

These differing requirements stemmed from the $K^+ \to \pi^+\mu^+e^-$ contamination sources being different for positively and negatively charged products of the $K^+ \to \pi^+\mu^+e^-$ decay.

As described earlier, positive and negative particles were separated by the first dipole magnet (D5) with positively charged particles going to the right and negative ones to the left side of the apparatus. This allowed for the use of different gases in the left and right sides of the Cerenkov counters. Use of hydrogen in the left (e^-) side, with a threshold gamma of about 52, provided momentum independent light yield to all electrons in our momentum range while setting a threshold momentum of about $7GeV/c$ and $5GeV/c$ for pions and muons respectively, well above the momentum range of any beam kaon decay products. A heavier gas (methane) was used in the right side (e^+) of the Cerenkov counters. It resulted in increased light yield for positrons, but lower threshold for pions and muons (3.5GeV and 4.7Gev for muons and pions respectively), that allowed some muons from the beam kaon and pion decays to make a signal in the Cerenkov counters.

The decision to use atmospheric pressure threshold Cerenkov counters implied relatively low light yield and thus an emphasis on efficient light collection both spatially and down to as low wavelength as reasonably possible. In order to reduce the probability of π^- producing knock-on electrons, low mass mirrors were required (especially in C1). The ideal goal of 100% coverage of all phase space occupied by tracks of interest was complicated in C1 by the magnetic field of D6 and in C2 by the large phase-space occupied by the low momentum electrons which presented a background to $K^+ \to \pi^+\mu^+e^-$ decay.

For both counters a tight gas system ($270 ft^3$ in C1 and $670 ft^3$ in C2) was required to allow separate filling of left and right sides of the counters with different gases and to minimize contamination by oxygen. Oxygen would increase scintillation effects and cut off low wavelength photons.

Optical design. General Remarks

The Liouville theorem for photons in optical systems states that

$$(\delta X \delta Y) \times (\delta \sin(\theta_X) \delta \sin(\theta_Y)) = const \tag{2.1}$$

It indicates that it is possible to reduce the area occupied by photons by increasing their angular spread.

Low energy electrons/positrons from the decay chain ($K^+ \to \pi^+\pi^0$; $\pi^0 \to e^+e^-\gamma$) occupy a large phase space (Figure 2.4) that covers the phase space of most of the other kaon decay products. Therefore, simulation of this decay chain was used for the Cerenkov counters' optical design. In C1, low energy e^+/e^- occupy about $100 cm^2 sr$. Since the usable area of a 5inch diameter photomultiplier(PMT) is about $100 cm^2$, and 2π sr can be subtended at the exit aperture of a standard Winston cone, only a modest number of PMTs was required if appropriate collectors could transform the phase space to a small spatial area and an angular distribution symmetric about the PMT axis. Effects of small gaps in optics (e.g., between the exit aperture and PMT surface) were addressed in the design.

Optical design: Challenges and innovative aspects

Cerenkov counters had to cover large photon phase space and combine high efficiency with minimum material introduced in the path of the particles. Therefore, the issue of fabrication and support of thin mirrors and the challenge of designing customized

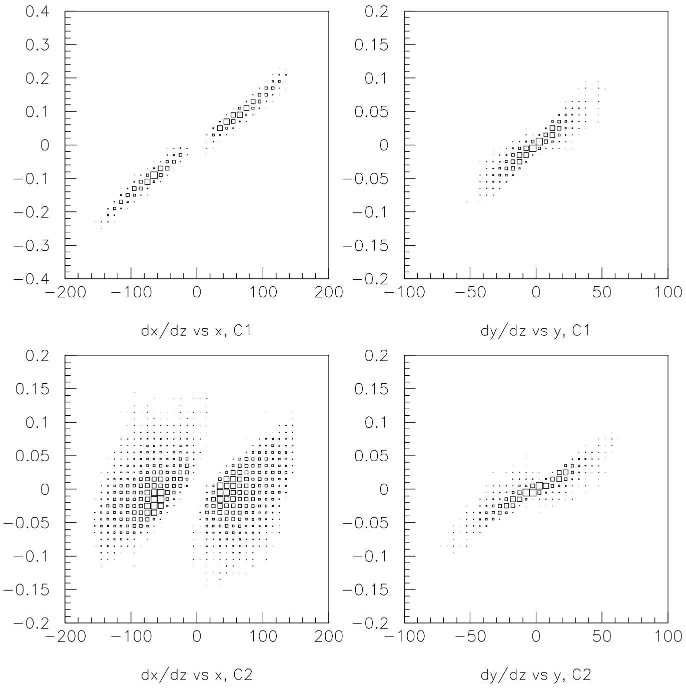

Figure 2.4: Phase space occupied by photons from the low invariant mass e^+e^- pair originating from the simulated $K^+ \to \pi^+\pi^0$; $\pi^0 \to e^+e^-\gamma$ decay chain.

optics had to be addressed.

Several possibilities for mirror manufacturing and support were considered and the chosen solution was to use Venetian blind arrays of mirror "slats" that can be shaped and oriented individually. Slats were made of thin aluminized acrylic (later replaced by polycarbonate in C1). The substrate was 0.51mm$(1.5 \times 10^{-3} X_0)$ and 0.81mm$(2.3 \times 10^{-3} X_0)$ thick for mirrors in C1 and C2 respectively.

Mirrors were supported by stiff lightweight frames of curved polyimide foam (Rohacell 51: Roehm GmbH, Darmstadt, Germany). A mirror slat was attached and held to the shape of the frame by one spot of glue and several flexible polyurethane bands. This technique helped to avoid problems connected with differential expansion of two materials. In order to minimize the amount of material, frames were made of ribs, rather than a solid piece. Each slat was supported by three ribs along its length connected by a few cross-pieces.

Slats were positioned roughly vertically with the primary curvature along the vertical direction. The horizontal curvature of the array was achieved by individual slats' orientation. The venetian blind design allowed continuous coverage for photons traveling away from the beam. Light collection was improved by introducing a small secondary curvature along the horizontal (short) dimension of the mirror slats. This curvature helped to better approximate a continuous mirror array. Distortions were well controlled by adding additional frame cross pieces. However, distortion at the very ends (beyond the final point of mirror attachment) of thinner mirrors in C1 proved to be problematic and was addressed by stiffening the mirror ends at the expense of increasing the material at the edges to $\approx 0.3\% \quad X_0$.

The design of the mirror array allowed for configuration of large and thin reflective surfaces of non-spherical form to be customized with respect to the detector requirements without constraints usually set by pressure vessels, ovens, and evaporators.

Construction of the array from differential elements allowed us flexibility in choice of the PMT and concentrator positions, quick modification and/or replacement of degraded elements, and fine-tuning of the shape to minimize the number of bounces and maximize light collection.

Horizontal bending in the D6 magnetic field results in dissimilar vertical and horizontal phase space occupation (Figure 2.4). In order to match these differences, we used modified compound elliptical concentrators [23] with the elliptical side in the bending and simple flat sides in the non-bending directions. Small mirror patches were used to rescue photons that would otherwise fall into the gaps between the square exit aperture of the concentrator and the circular PMT photocathode.

Optical design: C1 and C2 optics designs

Individual elements of each primary mirror array were oriented roughly vertically and pointed at a concentrator/photomultiplier assembly. While in C1 only one PMT corresponded to each mirror array, in C2 two PMTs collected photons from mirror arrays close to the beam. In C1, the intermediate mirrors were used to position PMTs in a region with lower magnetic field. More space in C2 allowed photons to be reflected directly to concentrator/PMT assemblies. Elevation drawings of C1 and C2 are presented in Figures 2.5 and 2.6.

Both C1 and C2 were left-right symmetric except for the beam-holes cut away in the primary mirrors, and for the hydrogen-filled beam tubes made to provide passage for the beam on the right side of the counters. Light collection was somewhat worse at the boundaries between mirror arrays and much worse at the outer edges of the aperture (e.g., close to magnet in C1). The latter was mostly due to photons traveling outside of the covered phase-space. Fortunately the outer edges of the aperture were only scarcely populated by the particles of interest.

Photons from the $K^+ \to \pi^+\pi^0$; $\pi^0 \to e^+e^-\gamma$ (Dal) decay chain were used for the

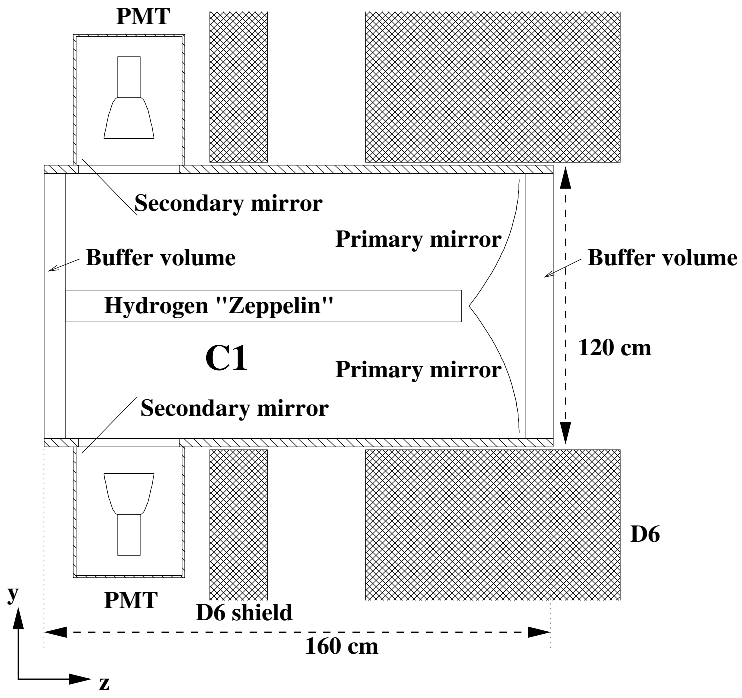

Figure 2.5: Elevation drawing of the right side of C1 Cerenkov counter. Shell, primary, secondary mirrors, and concentrator/PMT assemblies are shown. Two of the four PMTs are shadowed by the two that are shown, bringing the total number of PMTs to eight (four on each side of the counter). "Zeppelin" refers to to the hydrogen filled enclosure for the beam passage (beam tube). The left side of the counter is a mirror reflection of the right one except for the absence of the Zeppelin and different beam hole in the primary mirrors (not shown). D6 and the D6 shield refer to the pole and magnetic shielding of D6 spectrometer magnet.

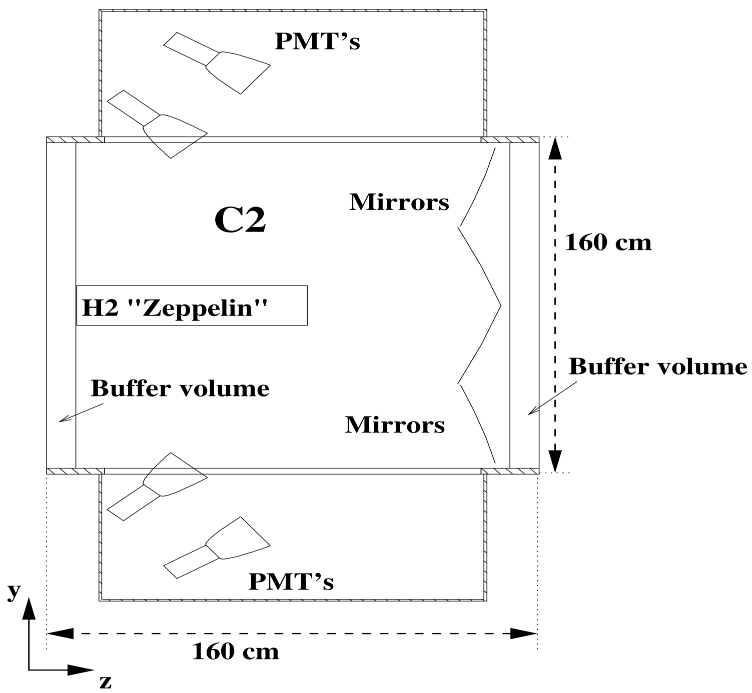

Figure 2.6: Elevation drawing of the right side of C2 Cerenkov counter. Shell, primary mirrors and concentrator/PMT assemblies, and H_2 filled beam tube (Zeppelin) are shown. Each PMT closest (vertically) to the beam shadows three PMTs behind it; each PMT furthest from the beam shadows one PMT behind it for a total of twelve PMTs per one side or 24 in C2.

testing of the C1 and C2 designs. The increase of the occupied phase space in C2 (Figure 2.4) was due to the large bending angles of the low momentum tracks. Two PMTs associated with each mirror assembly were used to account for that. Some of the photons from the low momentum electrons in C2 were travelling horizontally in the direction of the beam and were trapped between overlapping mirror slats if reflected close to the edge of the slats. These losses were found to be small compared to the other sources of inefficiencies.

The intermediate mirrors in C1 added on average an additional 0.75 bounce per photon. Computer simulation showed that the average number of bounces was approximately three in C1 and two in C2.

Each of the C1 primary mirror quadrants consisted of 14 slats (10cm wide; 60cm tall). C2 quadrants consisted of 24 slats (14cm wide; 40cm tall) arranged in 4 subarrays of 6 slats each. C1 mirror arrays reflected photons to the same side (vertically) of the beam. C2 mirror arrays closest to the beam reflected photons to the vertically opposite side of the beam. This was done to increase the radiative path for the highly populated area close to the beam. Mirror arrays furthest from the beam in C2 reflected photons to the same side of the beam to eliminate optical path obstruction.

Optics tests and construction: Metallization and reflectivity

Commercially available (Madico Inc., 45 Industrial Pkwy, Woburn, MA 01801-1919) aluminized mylar foil was used for the flat sides of the concentrators. While substantially cheaper than aluminized surfaces, it yielded high reflectivity in the visible spectrum and showed higher than 65% reflectivity down to 190nm.

Mirror slat substrates were metallized by electron beam evaporation of aluminum (80nm thick) followed by an additional coating in order to prevent formation of aluminum oxide that has poor reflective characteristics.

Initially, all mirrors were coated with 30nm MgF_2. This coating while providing for the good reflectivity, was susceptible to the degradation with humidity [24]. Alternative coating of SiO_2 was more durable, but was difficult to manufacture without adding $Si0$ admixture that caused low ultraviolet reflectivity. By 1997, an optimized SiO_2 coating was developed in cooperation with Clausing company (P.A. Clausing Inc., Skokie, IL 60076-3438). This coating showed reflectivity of $\approx 75-80\%$ in the wavelength range of 225-270nm. In Figure 2.7 measured reflectivities for different mirrors are shown. The mirrors designated EM were metallized by EMI with an evaporation method and MgF_2 overcoat and were used in early C1 tests. Because of their susceptibility to humidity and distortion, we switched to the CM... mirrors for the main E865 running (prepared by Clausing with an electron beam deposition method and MgF_2 overcoat). Because of accidental exposure of the left side of C1 to humidity, and the additional stress on efficient light collection in C1 because of the particle trajectories' bending throughout the collection volume, much of the C1 optics (all of the left primary mirrors, all of the intermediate mirrors, all of the collectors, and the outside top and bottom right primary mirrors) was replaced before the 1997 run with mirrors coated with SiO_2/SiO. (The overcoat was not pure SiO_2, but had substantially better reflectivity than pure SiO would have had). On the upper left plot, the x's correspond to the outer bottom primary mirrors and the crosses correspond to the outer top primary mirrors. We hypothesized that the lower reflectivity of the top mirrors resulted from their facing upward and therefore catching small dust or other particles on the surface. Such particles then served as a "seed" for areas of degradation of the thin reflective coating and overcoating.

Reflectivity was measured using an ordinary He-Ne laser for the long and D_2 arc lamp for the short wavelength photons respectively. A set of ultraviolet filters was used as a spectrometer. Reflectivity of the initially considered samples and of most of the finally installed mirrors was measured as a function of wavelength and position on the slat.

Optics tests and construction: Optical alignment

Relative optical alignment of the assembled mirror arrays was tested by scanning them with a laser beam. Special ray-tracing code was developed that could follow photons through the predefined optics. All elements of the optical design were modeled and optimized with this code.

Simulation showed that the vertical displacement is more critical than the horizontal (Figure 2.8). Based on the simulation results the limit of 1-2cm in Y and 2-3cm in X was set on the acceptable deviation of mirror's center of curvature position from the ideal one. This displacement was measured by using a laser beam and comparing the position of the returned beam with the expected one. The displacement of the returned beam was about two times larger than the mirror center displacement. Continuity of phase-space coverage was tested by sweeping the mirror array with the laser beam and checking for a reasonably continuous return beam.

Final tests of alignment with the arrays in the counters used about 80 test rays per one side of C1 and C2. The results showed that the final in-counter alignment

Figure 2.7: Reflectivity of different mirrors with different coating as a function of wavelength.

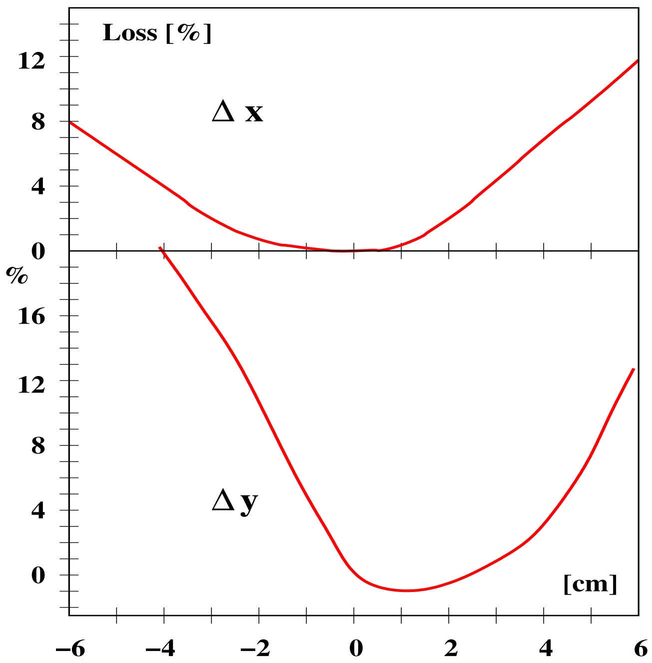

Figure 2.8: Simulated dependence of the photon loss on the displacement of the mirror's center of curvature. Deviation of the returned beam was about two times larger than the mirror curvature center displacement.

increased the loss of Cerenkov photons by about 5-10% (compared to simulation) and introduced one extra bounce (about 20% light loss per each bounce).

Mechanical design and construction

The Cerenkov counters' shell was fabricated of half inch thick aluminum plates. Windows were constructed from kevlar strengthened mylar ($75\mu m$ thick). Windows were attached to the shell by polyurethane gasket. Tests showed no helium leaks through windows or gaskets up to 150% of the design pressure (12"H_20).

Hydrogen-filled beam tubes were constructed of $40\mu m$ polyurethane surrounded by rohacell ribs for support. Early tests showed that the leakage of hydrogen from the beam tubes into surrounding gas was below $300 cm^3/h$. Gas pressure inside beam tubes had to be kept constant. Accidental overinflation of beam tubes occurred only once during the course of the experiment. It led to breaking of the rohacell frames, but integrity of the polyurethane shell was not breached. As a result, some parts of Cerenkov counters' primary mirrors were obscured by the deformed (without rohacell frame support) beam tubes. Fortunately, the obscured parts were located on the edge of the counters' acceptance and did not lead to any substantial data quality degradation.

Explosive gas volumes in both Cerenkov counters were surrounded by buffer volumes that were constantly purged with inert gas. Potential gas window failure was prevented by constant pressure monitoring (including electronic alarm system) and by providing low impedance (3cm diameter tubes and large bubblers) paths for the gas. The gas system allowed for as much as three exchanges of the whole C2 volume in about 8 hours. Counters were kept under a low but constant flow of inert gas (N_2) between data taking runs and were purged by N_2 before and after filling with either hydrogen or methane. After each purge, samples from each counter were tested for the relevant contamination concentration down to 0.5%.

Comparison of the measured efficiencies in N_2 (high absorption below 200nm) and CH_4 (low absorption) showed that photons with wavelength below 200nm were either absorbed by residual oxygen contamination or attenuated by optics.

Photomultipliers: Overview

The following requirements were considered when choosing the photomultiplier model;

- Ability to detect efficiently photons down to about 200nm. This required low UV absorption photocathode glass and/or wavelength shifter coating.
- High first dynode electron gain. This was necessary to provide good separation between one and two photoelectron signals: expected average electron signal in C1 in hydrogen was about 2-3 photoelectrons and separation of one-photoelectron signals coming from scintillation and/or delta electrons was crucial.
- Size of the photocathode: a larger size of the photocathode was desirable to reduce the number of cracks in optical coverage
- Price and availability of different photomultipliers.

After comparison of several photomultipliers, we chose the Burle(RCA) 8854 PMT, which provided a combination of large (12.7cm diameter) photocatode, high (20 compared to 10 in other tested PMTs) first dynode gain, and acceptable UV cutoff (240nm). In addition, Burle 8854 PMTs were available free of charge from the E777 BNL experiment.

Photomultipliers: Magnetic shielding

PMTs were located in regions with about 90G and 40-80G magnetic fields for C1 and C2 respectively. In C1 the primary magnetic field component was perpendicular and in C2 had an angle of about 45 degrees to the symmetry axis of the the PMT.

In C1, while the precise value of the field was not measured inside the magnetic shield, the PMT performance test with and without the magnetic field was acceptable. The magnetic shielding in C2 was more complicated. The final magnetic shielding design in C2 reduced the magnetic field at the photocathode to the levels of less than 1G. Extensive bench and in-counter tests showed that the residual magnetic field in C2 resulted in about 10% reduction in C2 PMTs' gain. We also discovered that much larger reduction in gain, initially observed for some photomultipliers, was due to residual magnetization of Kovar PMT shields. This residual magnetization was successfully removed with a coil producing about 50G in its center.

Photomultipliers: Wavelength shifter (WLS).

Application of wavelength shifting coating of the PMT photocathode window has an obvious advantage of extending PMT response into the short wavelength region, but might degrade timing characteristics of the photomultiplier response. P-terphenyl coating is the most commonly used one due to its short response time.

In order to test the effect of WLS coating on Burl 8854, senior researcher David Kraus and I constructed test setup where the Hamamatsu deuterium lamp was used as a light source. Aside from its high stability, the deuterium lamp offered a photon spectrum in the range between 200nm and 350nm similar to the one produced by Cerenkov radiation in transparent media. Light was delivered to the PMT photocathode through a pinhole aperture that had the first diffraction order image of about 1mm at 400nm wavelength. The resulting one photoelectron signal rate was at the level of 0.5MHz.

The light from the deuterium lamp was filtered through the set of thin film UV filters allowing for the measurement of PMT response to several bands of the lamp spectrum. Filters were mounted on a filter wheel that was operated (rotated) under computer (PC and CAMAC) control. The PMT was mounted on a frame that could be moved across the light beam by the motorized screw also controlled by computer. While this setup did not provide for an absolute quantum efficiency measurement, it allowed for stable and reproducible relative quantum efficiency determination and was used initially to predict improvement in photoelectron yield due to WLS coating

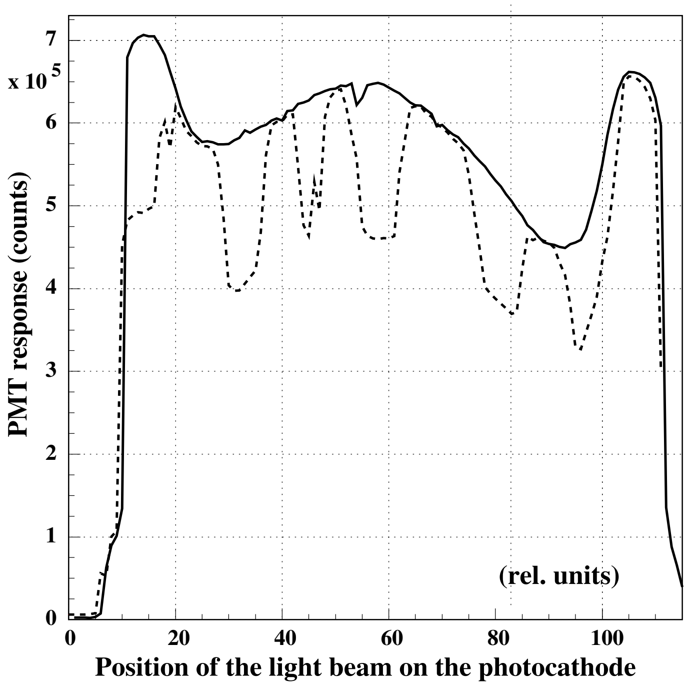

Figure 2.9: PMT response (in one-photoelectron counts per second) to the deuterium lamp light as a function of the relative position of the deuterium light beam on the PMT photocathode. Solid line shows PMT response with p-terphenyl WLS coating. Dotted line shows the same PMT response after several patches of WLS coating were scrubbed off.

and later for the quality control of PMTs coated with p-terphenyl in Fermi National Laboratory (FNAL). The filter wheel assembly was also used for the reflectivity measurement of the mirror slats that were put in C1 counter in 1997.

Response of one of the PMTs with and without the WLS coating to the unfiltered deuterium lamp light is presented in Figure 2.9.

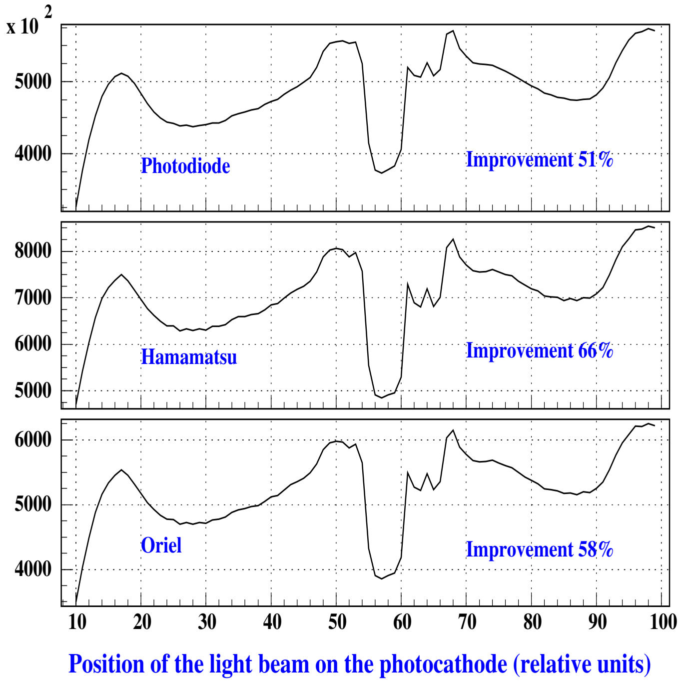

Figure 2.10: The inferred PMT response (in one-photoelectron counts per second) to the Cerenkov light as a function of the relative position of the light on the PMT photocathode. Three plots correspond to the three assumptions about the deuterium lamp spectrum: my spectrum measurement with photodiode (upper), Hamamatsu specifications (middle), and specifications from the third company (lower). The dip in the middle of the distributions corresponds to the place where WLS coating was scrubbed off.

Use of filters allowed us to seperate the deuterium lamp spectrum in several wavelength bands. Improvement of the PMT response due to the WLS was measured in each band. The relative photon flux between Cerenkov radiation and the deuterium lamp light in each band was used to infer the PMT response to the Cerenkov light modulated by the primary mirror reflectivity. This allowed us to make a prediction about improvement in the PMT performance under the real experimental conditions. Figure 2.10 shows the inferred response to Cerenkov light of one of the PMTs. For this particular PMT, analysis of its response with and without WLS to deuterium lamp light filtered through the set of UV filters yielded a prediction of $(58 \pm 10)\%$

improvement in photoelectron response to the Cerenkov radiation. Note that this was an estimate of the minimum improvement, as the test was done in the air with all photons below $\approx 195nm$ being absorbed by oxygen. The uncertainty of this prediction was determined by the uncertainty of the deuterium lamp spectrum in the region above 350nm: my measurements of this spectrum significantly disagreed with Hamamatsu specifications, and my communications with Hamamatsu technical support did not clarify this discrepancy. However, as the improvement itself was much larger than the error margin, we decided to install several WLS coated PMTs in the Cerenkov counters and measured photoelectron yield in the real data taking conditions. This was done in the very beginning of the 1997 running period. After these test results showed improvement in photoelectron yield compatible with the test-bench predictions, all of the PMTs in C1 and C2 counters were replaced by ones with WLS coating. Relative quantum efficiency of all PMTs was measured prior to their shipment to FNAL (where they were coated with p-terphenyl) and upon their arrival back to BNL. Measured response improvement varied from 30% to 65% for different PMTs. As some cases of very low improvement were traced back to contamination of the vacuum chamber used for coating, we assume that some of this variation was due to the PMT surface preparation and overall cleanliness of the chamber. Prior to their installation in the counters, PMTs were sorted according to their relative efficiency with better PMTs going into most occupied (by radiation from particles of interest) parts of the counters.

Installation early in the 1997 data taking run of the wavelength shifter coated PMTs together with the new SiO_2 coated mirrors in C1 led to 25-55% improvement (range is determined by PMT to PMT variations and includes variations in improvement due to mirror reflectivity and changes in mirror alignment). Agreement of the observed improvement with the prediction confirmed that photons with wavelengths below 200nm were not detected in the counters.

It is important to note that while some degradation in the timing response for signals of order of one photoelectron was observed, it did not significantly affect the particle separation probability.

Photomultipliers: Bases

Placement of PMTs inside the gas volume of the counters had several advantages:

- Avoiding short wavelength photon loss during their passage through an additional window

- Simplifying mechanical design
- Increasing flexibility in the optics designs

At the same time, location of PMTs inside the counters resulted in more stringent requirements on the reliability of the PMT/base assembly. Special care had to be taken to avoid any sparks between high voltage components and surrounding magnetic shielding. The latter was achieved by careful design of PMT isolation from its inner magnetic shield; the consequent extensive tests performed in the air and with a dummy (burned out) tube and high voltage supply connected through the high resistive chain showed reliability of the design. As an additional precaution, high voltage was supplied to the bases only after oxygen concentration dropped below 0.5% (about ten times lower than the explosive limit).

Zener diodes were added to the dynode high voltage distribution chain to avoid high currents through the resistors. The base components were potted into the cylinder around the neck of the inner PMT magnetic shield. Each base was put though a 200 hour burn-in cycle prior to putting it into the counter and aside from two occurrences (cold solder joint and failed resistor) there were no failures through all of the experiment. Base performance was stable up to 10MHz, about two times higher than the 4MHz detected by the most busy PMTs during the course of the experiment.

Readout electronics

The initial readout consisted of ADC and TDC channels. However, sometimes, an unrelated preceding pulse could prevent the discriminator and subsequently the TDC to fire if, by the time of the pulse of interest, the preceding pulse tail was still above the discriminator threshold (about 10mV). The resulting loss of TDC information occurred at rates as high as 5% in high-intensity PMTs. A second set of TDC channels with discriminator thresholds set above one photoelectron (above 30mV) was installed in 1997. Auxiliary electronics with an additional, more tightly timed ADC and TDC channel and with another ADC channel gated to detect signals that occurred prior to the main trigger were installed before the 1998 run.

Performance and monitoring

The performance (electron detection efficiency) of Cerenkov counters was monitored by the University of Pittsburgh group on a daily basis using special Cerenkov efficiency triggers collected with prescaled rate. This monitoring allowed for a timely response to any degradation of the counters performance. One example was the observed reduction in efficiency around beam tubes in 1998 that was traced to their overinflation and resulted in a modified inflation procedure that minimized the inefficiency.

The average (over one side of the counter) efficiencies were measured to be above 99% in CH_4 and about 90% in H_2 (after WLS application). These efficiencies can be transformed into an implied average number of photoelectrons assuming Poisson statistics: $N_{av} = ln(1 - efficiency)$. Comparison of this number with the observed number of photoelectrons in the ADC gave good agreement in hydrogen but about 20-30% disagreement in methane. This disagreement was attributed to the high sensitivity of the implied number of photoelectrons for the efficiencies above 99% to the small statistical inaccuracies in the measured efficiencies. An additional error for methane measurements was introduced by higher beam background (translated into higher contamination of the efficiency test sample) on the methane-filled right side of the counters.

Another complication was connected with the non-gaussian form of the one photoelectron response. Figure 2.11 shows the response of a typical one of the Burle 8854 PMT's used in the E865 Cerenkov counters. This plot shows a tube exposed to light of approximately 275 nm, in a spectrometer setup, with a marker at the pedestal position. Qualitatively the one p.e. peak dominates the signal region, with a small 2 p.e. contribution visible to the right of the one p.e. peak, and a low pulseheight plateau visible to the left of the one p.e. peak. For careful assessment of number of photoelectrons, the low pulseheight plateau must be taken into account. We do not know the origin of this effect. The qualitative features of the plot (position of one p.e. peak, low pulseheight plateau, etc) were observed with several experimental variations: thermionic emission from the photocathode, illumination at selected wavelengths between 200nm and 500nm, pulsed illumination with LED's (which permitted gating at intensities which guaranteed a percent or less of 1p.e. per gate, and scanning with a few mm beam which established the presence of the pedestal with roughly uniform strength for all areas of the photocathode. The ratio of the low pulseheight plateau to the one p.e. peak varies from about 10% to 30% for the collection of thirty or so tubes observed. Initial tests of the PMTs' response were performed by Michael Gach.

With less efficient hydrogen filled counters being less susceptible to these uncertainties, we took the photoelectron yields observed in hydrogen as a figure of merit of the counters. These yields translated into 57photoelectrons/cm/$\sin^2\theta$ for C1 and 66 for C2. Taking into account the observed insensitivity to photons below 200nm,

Figure 2.11: Response of one of the Burle 8854 PMTs to the light of approximately 275nm wavelength. Response is shown in ADC counts. Sharp spike at the very low amplitudes corresponds to the ADC pedestal.

5-10% PMT losses in magnetic field, 5-10% losses due to alignment imperfections and $\approx$ 20% losses per photon bounce, these results are compatible with simulation predictions.

Timing resolution of the electron signal in the Cerenkov counters after individual PMT offsets and slewing (time-pulseheight dependence) corrections was measured to be about 0.6-0.7ns (Section 5.4.2/Figure 5.2) and did not change significantly after WLS application.

2.3.2 Electromagnetic Calorimeter

The electromagnetic calorimeter was an array of 30(horizontally) and 20(vertically) Shashlyk type modules [25] (Figure 2.12).

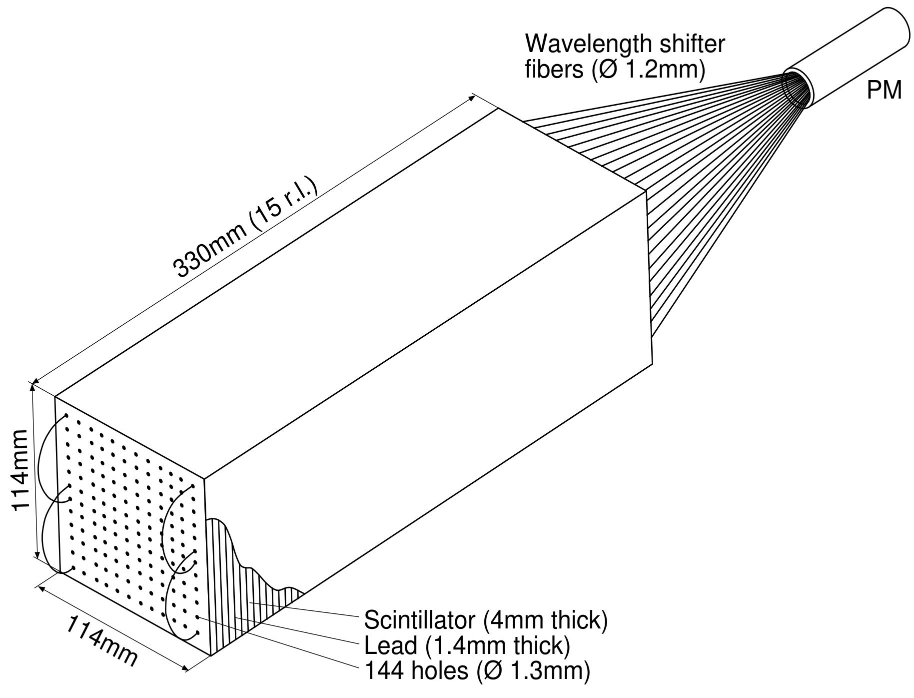

Figure 2.12: Calorimeter module drawing

Modules were constructed from perforated interleaved lead (1.4 ± 0.005mm thick) and plastic scintillator (4.0 ± 0.05cm thick) plates. White paper was used as a reflector on both sides of each scintillator plate. Light was collected through wavelength shifter fibers with 144 fibers going through each plate. In order to minimize the effect of longitudinal shower fluctuations, each fiber was looped in front of the module with both ends optically coupled to the photomultiplier located behind the module (from the beam direction). Each module had an $(11.4 \times 11.4)\text{cm}^2$ profile facing the beam and had a total depth of 15 radiation lengths.

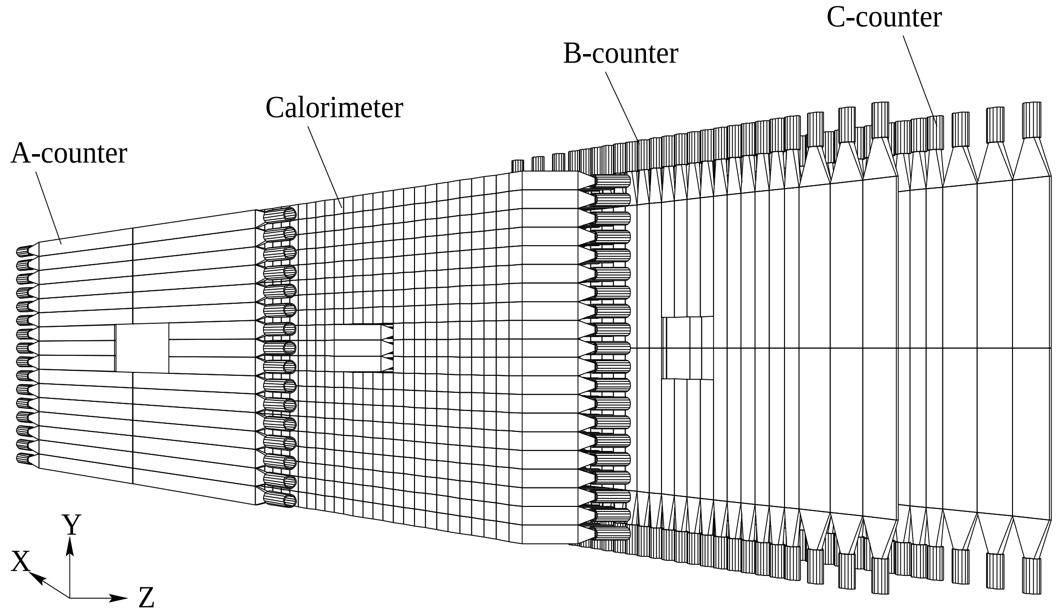

Figure 2.13: Calorimeter and scintillator hodoscope positioning. The A-counter was moved in this drawing by 1.5m upstream to allow for the unobscured view of the calorimeter

Figure 2.13 shows the calorimeter and the scintillator hosocope arrays. In the middle of the calorimeter, a 6×3 module hole was left for the passage of the beam.

Signals from the modules were split into ADC and TDC channels. The TDC channel went through a low threshold discriminator (1-20mV threshold set through a CAMAC controller). The discriminator output (20nsec wide ECL signals) was routed to the TDC modules and to the trigger logic. Due to the relatively large size of the full calorimeter digitized readout, it was sparsified to allow the storage (to tape) only of the signals above an ADC threshold. These thresholds were determined individually for each module from periodically taken special unsparsified data runs.

The energy resolution of the calorimeter was parameterized as

$$\sigma_E/E = \left(a^2 + \frac{b^2}{E}\right)^{1/2} \tag{2.2}$$

My analysis of the 1998 Ke3 data yielded $a = (5.18 \pm 0.06)\%$ and $b = (7.59 \pm 0.06)\% GeV^{1/2}$. While the second term (b) agrees well with previously obtained results [25][21], the constant term (a) is significantly larger than previously observed. As the constant term is sensitive to module-to-module variation in gain, this indicates that this variation was not taken (to its full extent) into account in the calorimeter calibration. The degradation of the calorimeter energy resolution leads to worse electron/positron identification efficiency for the same pion rejection. Nevertheless, the very limited use of calorimeter information in my analysis (coupled with correct simulation of the resolution) made the observed resolution acceptable.

2.3.3 Muon Range System

The muon range system was used to separate pions from muons by their depth of penetration into the system. It was located directly behind the calorimeter. The elevation view of the muon system is presented in Figure 2.14.

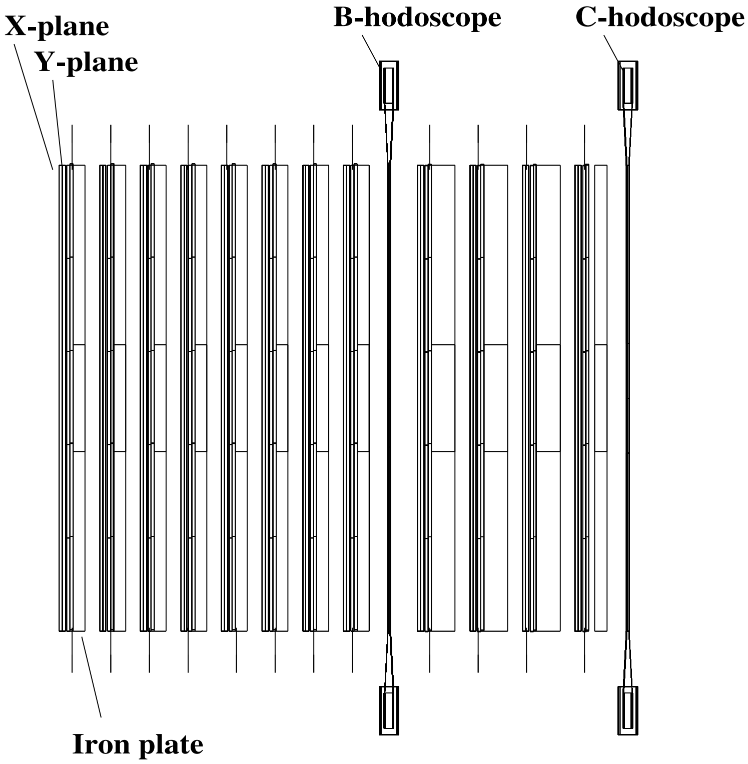

Figure 2.14: Elevation view of the muon system. Included in the drawing are the B-hodoscope, and C-hodoscope.

The minimum energy required for a muon to reach the B-hodoscope and C-hodoscope was 0.8GeV and 1.3GeV respectively. These numbers include muon energy loss in the 15 radiation lengths of the calorimeter (about 250MeV).

While the muon system was crucial for the $K^+ \to \pi^+\mu^+e^-$ analysis, I did not use it in my analysis of the Ke3 data.

2.4 Scintillator Hodoscopes

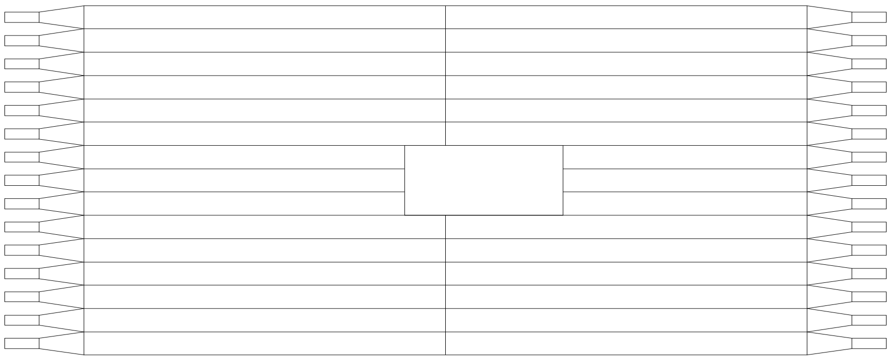

Figure 2.15: Schematic drawing of downstream view of the the A-hodoscope array

The four scintillator hodoscopes (A, B, C and D) all served different purposes:

- The A-hodoscope was positioned immediately up-stream from the calorimeter. It consisted of 30 scintillator slabs positioned horizontally (Figure 2.15, 2.13). Each slab was 11.4cm^2 wide and 1cm thick. Some of the slabs were cut short to provide for a beam-hole in the middle of the hodoscope. Coincidence (in time and space) between a hit in the A-hosocope and the calorimeter was usually caused by a charged particle and was used as the most basic building block of the lowest level on-line trigger for the $K^+ \to \pi^+\mu^+e^-$ data collection.

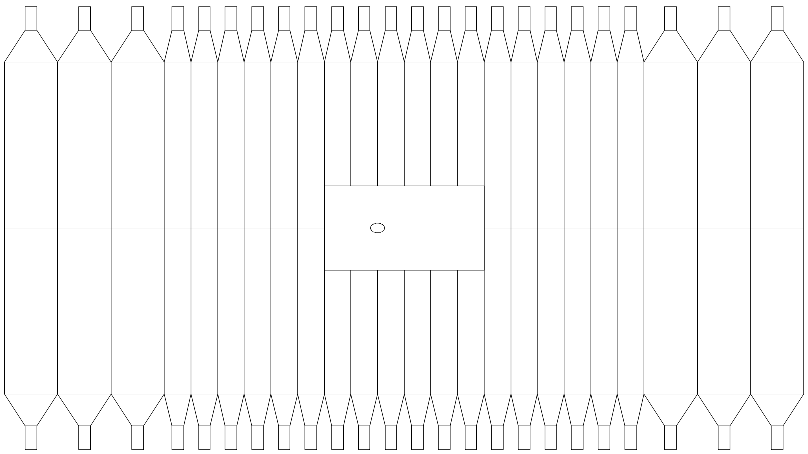

Figure 2.16: Schematic drawing of downstream view of the the B-hodoscope array

- The B and C hodoscopes (Figure 2.16, 2.13, 2.14) were part of the muon system and were used in the muon part of the $K^+ \rightarrow \pi^+\mu^+e^-$ trigger. Scintillator slabs in both B and C hodoscopes were positioned vertically and were 1cm thick. B and C hodoscopes were similar except for the slight difference in the beam hole size.

- The D-hodoscope (Figure 2.1) was installed between P1 and P2 after the 1995 data taking run and consisted of 20 (10 on each side) horizontally positioned slabs of $(80 \times 10)\text{cm}^2$ area each. Scintillator slabs were 3mm thick and the light was collected on one end of the slab (the one furtherest from the beam). The D-hodoscope was used as a part of the lowest level on-line trigger. Its purpose was to decrease the trigger rate by requiring rough spatial (vertical) correlation of hits in D-hodoscope slabs with the A-hodoscope and calorimeter hits (assuring that the hits in the A-hodoscope and calorimeter were caused by tracks originating from the decay volume). The time coincidence between at least one D-hodoscope slab from each side was used as the lowest level trigger for the Ke3 data collection.

2.5 Trigger System

The trigger system of the E865 experiment was designed for the purpose of the $K^+ \rightarrow \pi^+\mu^+e^-$ decay search. During the $K^+ \rightarrow \pi^+\mu^+e^-$ data taking, the average rate of charged tracks through the sensitive aperture of the detector was about 50MHz. The data was saved to the Exabyte 8mm tape drive with about 500kb/s writing speed. With one event size of about 2kb, only a few hundred events can be saved per second. These conditions required a fast trigger with very high background rejection coupled with high detection efficiency for kaon decays. In order to achieve these requirements, a multilevel trigger was constructed with most of the background rejected by the lowest level hardware levels of the trigger and more sophisticated (hence slower) selection performed at the higher (last) stages.

2.5.1 *Trigger used for the standard $K^+ \rightarrow \pi^+\mu^+e^-$ data collection*

As the standard E865 trigger has been extensively discussed before[21], I will limit its description here to the most important points:

- T0 trigger: the lowest level trigger that required at least three coincidences between A-hodoscope, shower calorimeter and D-hodoscope (D*A*SH). The combination of the three found D*A*SH hits was required to be roughly consistent with kinematics of three charged tracks (one negative and two positive or visa-versa) coming from the decay volume. The T0 level trigger had a response time of about 170ns and had an output rate of about 350kHz. All subsequent trigger levels required T0 and were timed by it.

- T1 trigger: this trigger utilized particle identification information from the Cerenkov counters and muon system combined with spatial information from the Cerenkov counters, calorimeter and muon system (B hodoscope). Using this information, triggers designed to select different kaon decay modes were formed. The main trigger: $\pi^+\mu^+e^-$, called MUE, required both Cerenkov counters on the left (e^-) and a muon system (B-hodoscope) hit spatially consistent with an A*SH hit. Several other triggers were formed in the same manner and were used to select all major kaon decay modes with at least three charged particles in the final state. All T1 triggers were prescaled except for the MUE trigger. T1 had about 1.5kHz output rate and was fanned out to all digitization modules. It had a response time of about 130ns.

- T2 trigger: this trigger was used for selection of events with high invariant mass e^+e^- pairs while suppressing events with an e^+e^- pair originating from $\pi^0 \rightarrow e^+e^-\gamma$ decays (low invariant mass). Information from Cerenkov counters, A-hodoscope and calorimeter was used to identify events with hit patterns consistent with an e^+e^- tracks having small vertical separation (low invariant mass). These events were prescaled, while the ones that had evidence of an e^+e^- pair but did not satisfy the low mass criteria were passed directly to the next level trigger. The T2 trigger had an output rate of about 0.7kHz and its decision was made about 200ns after T1.

- T3 trigger: this trigger compared the number of hits in each PWC plane with preloaded likelihood distributions obtained offline. This trigger level rejected events that contained too many or too few PWC hits. The average rate of T3 output was about 1,700 events per 2.8second AGS spill.

All of the trigger logic described above was realized in hardware. Custom made programmable MLU (matrix lookup units) were used for hit pattern selection and NIM modules were used for the simpler (AND/OR) logic of the trigger.

2.5.2 Trigger mix used for the Ke3 data collection

Three main requirements were considered in design of the Ke3 data collection trigger:

- The trigger should provide as little bias (in selection efficiency) between the signal (Ke3) and the normalizer (Kdal) as possible.
- The trigger mix should provide for the extraction of the efficiencies of all detector elements from the collected data.
- Relative trigger efficiencies for the Ke3 and Kdal events should be extracted from the collected data.

Both Ke3 and Kdal events have low invariant mass e^+e^- pair in the final state (from the $\pi^0 \to e^+e^-\gamma$ decay) that occupied similar phase space in the E865 detector. Therefore, a trigger that selects events with e^+e^- was the obvious choice for the main Ke3 trigger. Such a trigger was implemented in the standard E865 trigger mix. It was called ELER and required time coincidence of at least one PMT hit from each of the four Cerenkov counters. However, there were two reasons why the use of the standard E865 trigger was not advisable: firstly, it required D*A*SH at its lowest level, therefore efficiencies of the D-hodoscope, A-hodoscope and the calorimeter could not be determined in a model independent way from the data; secondly, three hits in the calorimeter were required. The latter could introduce systematic bias between Ke3 and Kdal decays due to the difference in the calorimeter response to e^+ and to $\pi^+\mu^+$.

In order to eliminate these shortcomings, we decided to modify the standard E865 trigger for the purpose of the Ke3 data collection. It is important to note that while the search for the $K^+ \to \pi^+\mu^+e^-$ decay required operation at the highest possible beam intensities, the Ke3 data could be collected at much lower rates. Taking into account kaon life time, branching ratio of the Ke3 followed by $\pi^0 \to e^+e^-\gamma$ decay chain, and the E865 acceptance, the beam intensity of about 10^7 kaons per 2.8sec AGS pulse (about 10 times lower than the standard E865 beam rate) resulted in $\approx$3.5 reconstructed Ke3 decays per pulse. With AGS duty cycle of 5.1sec, that translated into approximately 60,000 collected Ke3 events per 24 hours of continuous running. Such reduction in rate made it possible to remove the requirement of the three charged hits in the calorimeter that was necessary for the standard trigger.

A schematic of the finally designed and implemented trigger logic is presented in Figure 2.17.

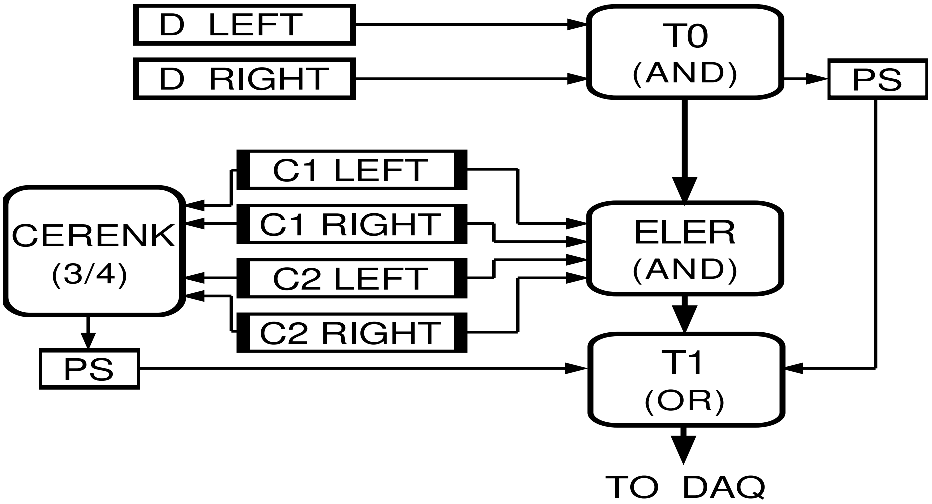

Figure 2.17: Schematic drawing of the trigger logic used for the 1998 Ke3 data collection. DLEFT and DRIGHT are the OR combinations from the D-hodoscope scintillator slabs on the left and on the right; C1LEFT, C1RIGHT, C2LEFT, and C2RIGHT are the OR combinations from the four Cerenkov counters.

Trigger elements

- **DLEFT, DRIGHT**: logical OR of the D-hodoscope scintillator slabs from the left and right sides of the hodoscope array.
- **C1LEFT, C1RIGHT, C2LEFT, C2RIGHT**: discriminated (threshold $\approx$0.25 photoelectrons) dynode signals of all PMTs from each of the four Cerenkov counters were fanned (logical OR) in the four logical signals that signified presence (or absence) of the signal in each of the four counters.

Trigger Logic

- The zero level trigger (T0) required logical AND of DLEFT and DRIGHT signals.
- The main Ke3 trigger (ELER) required logical AND of T0 with the four Cerenkov counters.
- The CERENK trigger required three out of four Cerenkov counters and was prescaled. CERENK trigger events were used for the determination of the Cerenkov counters and D-hodoscope efficiencies
- The prescaled T0 (called TAU) trigger was used for the $K^+ \to \pi^+\pi^+\pi^-$ decays collection. These decays were used for the calibration purposes. Prescaled T0

trigger was also used for determination of the efficiency of the Cerenkov part of the ELER trigger.

All trigger elements were latched (before and after prescales, where appropriate). This provided for the determination of the relative trigger efficiencies. The T1 output was fanned out to all digitization modules (start signal for the TDCs and gate signal for the ADCs). Delays between T1, T2 and T3 trigger levels were retained the same as for the standard E865 trigger but without any decisions made either at the T2 or T3 level.

The prescales on CERENK and TAU triggers were adjusted to produce about 850Hz T1 output rate (maximum allowed by the DAQ system throughput).

2.6 Data Acquisition System

The data acquisition (DAQ) system consisted of CAMAC, Fastbus, VME modules, and three computers: two DEC Alpha workstations, and one VAXstation. Schematic diagram of DAQ system is shown in Figure 2.18.

The DAQ system took advantage of the 5.1 second AGS duty cycle with 2.8 second of beam-on (spill) time. Data from CAMAC crates were transferred to the 4Mb Fastbus memory buffer (LeCroy 1892) for each T3 output. There was no event buffering in the CAMAC system. Therefore, the whole system was inhibited until all data were transferred from CAMAC to Fastbus memory buffer. Time needed for one event transfer averaged at about 200μs and depended on the PWC occupancy.

Data from Fastbus ADC and TDC modules was transferred to memory buffers during the spill. As Fastbus TDC and ADC modules could buffer 7 and 64 events respectively, the readout of ADC/TDC modules did not yield any dead time up to six buffered events. A special counter kept track of the number of buffered events and if seven events were buffered, the system was inhibited until one event was read out.

Memory buffers were read out between the spills into the internal memory (4Mb) of CERN host interface (CHI), which wrote the data directly into the memory of two DEC Alpha workstations through the VME interface. Data were transferred from CHI to the workstations at a maximum rate of 3.27Mb/s.

Since the transfer rate between the workstations and the VAXstation (limited by Ethernet) was about 450kb/s, and the maximum tape drive writing speed was about 400kb/s, the average $(1700 events \times 2kb/event) = 3.4Mb$ of data were still too much to write to the tape in 5.1s of the AGS duty cycle. Additional event rate reduction was performed in the DEC workstations by a series of software filters.

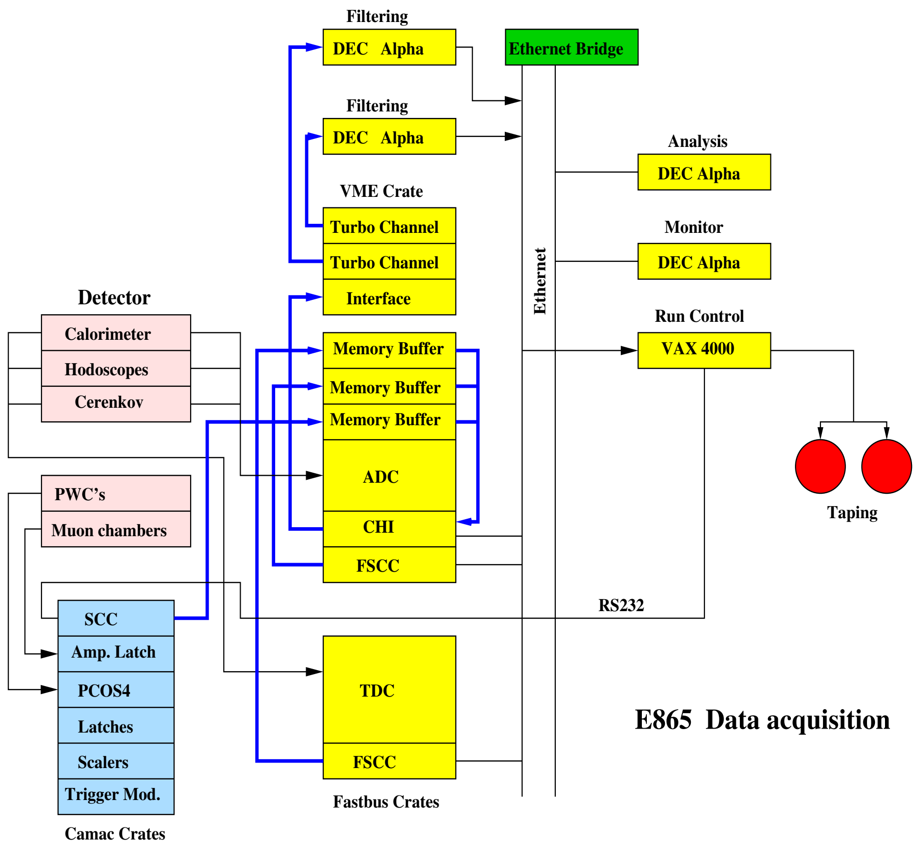

Figure 2.18: Schematic diagram of the E865 data acquisition system.

The filters were implemented in sequence starting with the simplest (fastest) and finishing with the more complicated (slowest) ones. The configuration of the filters used could be changed and was indeed varied through the course of the experiment. Crude calorimeter clump reconstruction was performed and even vertical coordinates of the tracks were reconstructed. Filters rejected about (40-50)% of the events. More detailed description of the filters can be found in [21]. The workstations also performed the task of event building, as the data transferred from CHI were still in the form of Fastbus memory blocks.

It is important to note that during the dedicated Ke3 data collection, all filters were turned off and the workstations were used solely for the event building. This was done for two reasons: firstly, the lower beam intensity greatly decreased the event size (to below 1kb), so that the tape drive write speed allowed for adequate (about 2,300 events per AGS pulse) throughput, and secondly, because crude event reconstruction at the filter stage could introduce systematic bias between different kaon decay modes.

The VAXstation performed all control functions and wrote events to the data tape.

A small fraction of events (about 1%) was sent to the two additional DEC stations for the purpose of on-line data quality monitoring.

The ADC modules were gated by the T1 signal, TDC modules operated in a common start mode with start signal coming also from T1. The failure of the subsequent trigger levels (T2 or T3) resulted in a fast clear with ADC and TDC modules ready for a new trigger in 1μs.

The DAQ system deadtime was incurred mostly due to CAMAC inability to buffer events and was kept below 20% for most of the running time. Event buffering in the Fastbus modules and parallel transfer of data from two Fastbus crate controllers to the memory buffers almost entirely eliminated other readout deadtimes.

CHAPTER 3
KE3 DATA COLLECTION

The Ke3 trigger was implemented and tested by the University of Pittsburgh group in the end of 1998. The Ke3 data taking run was performed during the last week of 1998. The beam intensity was lowered by about a factor of ten compared to the standard E865 running conditions. Careful monitoring of the detector elements' performance was carried out by the E865 members on shift duty and by the University of Pittsburgh group.

CHAPTER 4
OFFLINE DATA ANALYSIS

4.1 Overview

The standard E865 event reconstruction is described extensively in [19],[20],[21]. Its logic was based on the standard E865 trigger logic, i.e. the first requirement was to find at least three charged clumps in the calorimeter. The positions of the found clumps were used to determine approximate rectangular “windows” in each of the PWCs. Only PWC wire hits that were inside these windows were allowed to contribute to the track fitting in the spectrometer.

No requirement of the calorimeter in the Ke3 trigger, and the lower multiplicity of the PWC wire hits due to the lower beam intensity allowed me to modify the reconstruction procedure in such a way that all of the PWC hits were considered for the purpose of track finding. Clumps in the calorimeter were reconstructed after three tracks with a common vertex inside the decay volume were found. The Ke3 trigger requirement of at least one hit on the both sides of the D-hodoscope was satisfied at the final event selection stage. Except for these structural changes, I mostly used the standard E865 event reconstruction package described below, with appropriate changes pointed out.

4.2 Track reconstruction

The track reconstruction procedure began with combining the raw wire hits into the space points.

First, we found the wire clusters, defined as one or more wire hits in a certain PWC plane which were located next to each other. In the case of more than one wire in the cluster, the cluster position was defined as a simple average of the comprising wires' positions.

The point in space where the clusters from all four PWC planes overlap ('quadruplets') were found first. The position of the quadruplet space point was determined by minimization of the $\sigma^2\chi^2$ constructed from squared differences between the cluster positions and the position of the space point. The space point was accepted if the resulting $\sigma^2\chi^2$ was less than a threshold determined from a calibration set of real data. The algorithm looped through all quadruplet combinations in each chamber, then proceeded to find "triplets" in a similar fashion.

Any given cluster was allowed to contribute to different space points. At the same time, if the two space points had more than two common clusters, the space point with the worse $\sigma^2\chi^2$ was discarded.

The next step was to combine space points that could have come from one track (crude track finding). The track in the E865 spectrometer can be crudely approximated by two straight lines that have the same vertical slope, and meet at the mid-plane of the D6 magnet. The χ^2 that tested this hypothesis was constructed first for all possible combinations of the found space points that included one space point from each of the four chambers (four-chamber tracks). Four space point combinations that had χ^2 less than a threshold determined from the real data were saved. After that the algorithm proceeded to find the three-chamber tracks. For the three chamber tracks, the tested hypothesis was that the space point in the middle chamber should be vertically close to the straight line between the space points in the first and the last chambers. The vertical slope at the D6 middle plane was tested in the same way as for the four-chamber tracks.

In the standard E865 analysis, the additional requirement of the track's spatial consistency with the clump found in the calorimeter was implemented. I removed this requirement from the Ke3 data reconstruction.

After the space point combinations that were likely to form a track were found and stored, the algorithm proceeded to find the track's momentum. This was done by fitting the found track's trajectory in the detailed map of the E865 magnetic field. Instead of the space points, the coordinates of the separate wire clusters were used in the fit. The track's trajectory was determined by the set of the five parameters: $X; \theta_x; Y; \theta_Y$ at the mid plane of the PWC1, and the track's curvature (ratio of the charge to the track's momentum in the XZ plane).

First order Taylor expansion of the χ^2 around the track parameters obtained from the previous step of the reconstruction reduces the problem of fitting to the numerical calculation of the partial derivatives of the fitted track's position and the inversion of the resulting matrix.

The numerical calculation of the derivatives was the most CPU-intensive part of the event reconstruction. In case of the standard E865 analysis, the first processing of the raw data was done with a very crude (large) step size used to calculate the track's trajectory in the magnetic field. The smaller step size was used in the consequent analysis.

For the Ke3 data I used the finest step size (5cm), both for the raw data processing, and for the final analysis. This was possible due to the lower PWC occupancy (fewer track combinations) in the Ke3 data. The comparatively small size of the Ke3 raw data also allowed for the longer processing time.

The χ^2/Ndf cut was set at 100 allowing for virtually all of the fitted tracks to participate in the vertex finding procedure.

4.3 Common Vertex Reconstruction

After the track parameters were fitted in the spectrometer, the obtained position, angle and momentum of each track were used to propagate the track's trajectory through the D5 magnetic field back into the middle (in Z) of the vacuum decay volume. Next the three track common vertices were found for all possible combinations of the fitted tracks. The position of the vertex was obtained by minimization of the quantity S: the R.M.S. of the closest approach of the three tracks to the common vertex point. The three track combination that yielded the common vertex with the smallest value of S was considered an event and was saved for further analysis, unless it did not satisfy the loose requirement of $S < 10cm$. This procedure did not take into account the errors of the reconstructed tracks' positions; as a result, the average value of S increased for the vertices found far upstream. The average dependence of S on the Z position of the vertex was obtained empirically (from the data) and was used to remove such dependence. The corrected S called $Snorm$ was used to make a vertex quality cut at the later stages of the analysis.

The alternative method of the constrained vertex fit was developed by the Pittsburgh group and used the track error matrix obtained from the tracks' fit in the spectrometer and propagated back through the magnetic field of D5. Uncertainties of the field map used were included in the error matrix. The constrained fit allowed correct treatment of correlated uncertainties of the reconstructed tracks' positions and provided the true χ^2 of the constrained fit as the vertex quality indicator. The developed constrained vertex fit is used now for the analysis of the last (and the largest) sample of the $K^+ \to \pi^+\mu^+e^-$ data. The constrained vertex fit was not used for obtaining the final result of this analysis, but served as an important test of the robustness of the analysis.

4.4 Reconstruction of clumps in the calorimeter

After three tracks with a reasonable quality common vertex ($S < 10cm$) were found, the algorithm proceeded to find clumps in the calorimeter.

The standard E865 event reconstruction used time coincidence between the calorimeter module and the A-hodoscope slab in front of it as the seed of the charged clump (caused by the charged particle). After the seed was found, the eight calorimeter modules around it were considered a clump and the energy deposited in them was summed up to form the energy of the clump. The timing of the clump was calculated as a weighted (by the energy deposition) average of the times in the nine modules. As neutral particles scarcely induce signal in the A-hodoscope scintillator, the neutral clump was required to have no in-time A counter in front of it.

For the purpose of the Ke3 analysis I modified the described procedure in two ways:

- An alternative clump-finding algorithm was developed by the INR (Institute for Nuclear Research, Russia) part of the collaboration. This algorithm used time and energy information from the calorimeter modules to form clumps independent of the A-hodoscope. It also provided for the separation of the energy between overlapping clumps. While this algorithm was developed in the early stages of the experiment, it was not fine-tuned and tested to the extent of being included in the standard event reconstruction. I conducted consistent tests of this algorithm performance compared to the standard clump-finding. After several adjustments, it became the standard algorithm for the both 1998 $K^+ \to \pi^+\mu^+e^-$ and Ke3 analysis.

- Exclusively for the Ke3 analysis, I also modified the clump finding by allowing the A-hodoscope hits in front of a neutral clumps. I did it because the data analysis showed about 10% difference in the probability of the A-hodoscope hit in front of the clump caused by a photon due to the inaccurate simulation of the backscatter from the calorimeter. The low beam intensity during the Ke3 data taking resulted in a low number (average of less than four) of reconstructed clumps; therefore any clump that was further than 30cm from the positions of the charged tracks was considered as a neutral clump candidate.

It is important to note that the clump finding procedure could not result in the event rejection at the reconstruction stage. The information from the calorimeter was used later for event selection and for the π^0 reconstruction.

4.5 Matching of tracks to hits in the Cerenkov counters

As described in Section 2.3.1, the Cerenkov counter optics correlated particular regions in the (X;Y) plane to the particular PMT(s). This correlation was used in evaluating the Cerenkov counter response to the particular track. The track's position at the nominal primary mirror plane was used to determine which PMTs could have seen the signal from it (candidate PMTs). If the track was closer than 10cm to the border between two regions, the PMTs correspondent to both mirror assemblies were tested for the presence of the signal. This was done to account for the finite size of the Cerenkov cone at the mirror plane.

The ADC signals of the candidate PMTs were summed up to obtain the photoelectron count of the Cerenkov light associated with the track. The overall time was calculated as the weighted (by the ADC signals) average of all candidate PMTs associated with a particular track. Any single PMT was allowed to contribute to the average time only if its one TDC count was within 10ns of the event time determined by the D-hodoscope.

This procedure did not attempt to separate the Cerenkov signal between two tracks that "shared" some, or had exactly the same candidate PMTs. In the case of exactly the same candidate PMTs, the same signal was assigned to both tracks.

CHAPTER 5
DETECTOR CALIBRATION AND EFFICIENCIES

5.1 Overview

Knowledge of the exact positions of the PWCs and dependence of the magnetic field on the coordinate in both dipole magnets is essential for the correct track reconstruction. PWC positions, orientation, and magnetic field map were determined by direct measurements and refined using the collected data.

The response of each detector element was digitized using Analog-Digital converters (ADCs) and/or Time-Digital converters(TDCs). Calibration of each digitization channel is needed to reconstruct the original response of the detector. Such calibration was performed using the collected data and took into account response variations between individual detector elements (eg. individual photomultipliers in Cerenkov counters or individual modules in the calorimeter).

Detector inefficiencies have to be taken into account for the calculation of the detector acceptance. Inefficiencies of all detector elements were obtained from the collected data using special triggers or built-in redundancy of the collected information. Inefficiency of each detector subsystem was measured with appropriate granularity and as a function of the appropriate phase space. Results of these measurements were summarized in a form compatible with the E865 Monte Carlo simulation package (KAY [26]).

5.2 Magnetic field map

Three components of the magnetic field from both dipole magnets were measured on a three dimensional grid with 5cm step using the ZipTrak field mapping system borrowed from Fermilab. The measurements were done before any apparatus was placed inside the magnets and were done in sets with the Hall probe repositioned, and sometimes recalibrated, between sets. This procedure led to inconsistencies in the field map scale between different parts of space. The ZipTrak data were converted into the magnetic field map data file used by the reconstruction software to obtain the three components of the field in any given point. The conversion was done early in the experiment (1994) and unfortunately was poorly documented.

In order to study systematic uncertainties in the magnetic field map, the University of Pittsburgh group performed limited measurements of the magnetic field at the end of the 1998 run and conducted an involved consistency study of the magnetic field map using the results of these measurements, the remaining ZipTrak data, the magnetic field map used in the event reconstruction, and the magnetic field map created with TOSCA software. This study showed that while the agreement was satisfactory within approximately $\pm 40cm$ in Y (in the D6 magnet), the different compared field maps disagreed by as much as 10% at the edges of the magnet's aperture. The measurement performed in the end of 1998 also showed $(2 \pm 0.5)\%$ higher overall field scale plus about 2cm shift in Z position compared to the map used in the reconstruction. While both of these corrections were already artificially used in the event reconstruction, they were previously obtained by comparison of the distributions of the kaon mass from the reconstructed data and Monte Carlo $K^+ \to \pi^+\pi^+\pi^-$ events, and the 1998 measurements allowed us to confirm these corrections experimentally.

In order to fine-tune the overall scale of the magnetic field I compared Monte Carlo and data distributions of the reconstructed kaon mass and invariant e^+e^- mass from $K^+ \to \pi^+\pi^+\pi^-$ and $\pi^0 \to e^+e^-\gamma$ decays respectively. These distributions are the ones which are most sensitive to the magnetic field. I found that we need to scale down the D6 magnetic field by 0.25% for the Monte Carlo to agree with data. This analysis also showed that I can not determine the overall field scale from such a comparison with accuracy better than about 0.1%.

Magnet positions relative to the rest of the detector were determined from the measurements performed by the AGS survey team.

The systematic uncertainty of the Ke3 branching ratio arising from the imprecise knowledge of the magnetic field map (Section 10.2) was estimated to be small compared to the other systematic error sources.

5.3 Proportional Wire Chamber Position calibration

PWC wire positions in three dimensional space are crucial for the correct track reconstruction. Determination of these positions consisted of several stages.

First, positions of four corners of each of the four chambers were measured by the AGS survey team. While this measurement was done with precision of better than 0.1mm, it gave only positions of the chamber enclosures but not the wires. It also did not provide information on the exact orientation and spacing of wires in different planes. In order to correct these shortcomings, a special set of events (alignment data) was collected. The alignment data were recorded with both detector magnets shut off, beam collimators fully closed, and Q6 beam-line quadrupole operating at lower current. The trigger was set to require at least one cluster in the calorimeter. As a result, the collected data consisted of events with single straight (no bend in the magnetic field) track events most of which were muons resulting from pion and kaon decays in the beam. Such tracks can be reconstructed using only two out of four PWCs and were used to adjust positions, orientations and wire spacings of the individual planes of all four chambers through an iteration process [19]. While such calibration provides alignment which is self-consistent within the "package" of four PWCs, we still need the position of the "package" itself with the respect to the rest of the apparatus. This position for the 1998 data was taken from the survey measurements and was checked for consistency by matching coordinates of the reconstructed tracks with coordinates of the clumps in the calorimeter.

In the final alignment procedure (developed by the University of Pittsburgh group), each wire plane was allowed to have different orientation and wire spacing in the left and right sides of each chamber. While such difference can be justified for the Y-plane wires (which are physically separated left from right), for the other three planes it is more difficult to explain. The estimated differences (left from right) in wire orientation were below $1 mrad$ and in wire spacing below 0.1%.

Additional fine adjustments to the PWC alignment were done by analyzing the collected $K^+ \to \pi^+\pi^+\pi^-$ and $\pi^0 \to e^+e^-\gamma$ decays and performing an analysis similar to that done with the alignment data.

The final PWC spatial positions and orientations were used for all stages of data reconstruction. For simplicity, I used symmetric (left/right) PWC alignment for the Monte Carlo simulation and reconstruction.

5.4 Gain and Timing calibration

5.4.1 D Hodoscope

The signal from the D hodoscope array served as a TDC start for the Ke3 data. ADC information from the hodoscope was not used in the Ke3 analysis due to the pulse-height readout being adjusted through the course of the run: the D-counter discriminator threshold was set at about 30% of the minimum ionizing signal. Readout for each of the 80cm long scintillator slabs was performed by a PMT attached to one side of the slab.

For the purpose of the timing calibration, data events with three tracks coming from a common vertex were used. Each scintillator was divided into eight bins (10cm each) along its length. This resulted in 160 bins (20 scintillators × 8 bins). Track coordinates obtained from the spectrometer were used to define which bins were hit. Only events where all three tracks occupied different bins were used.

For each of the bins, the timing correction was defined as:

$$\delta T_i = -\sum_n (t_{in} - (t_{in} + t_{jn} + t_{kn})/3) \tag{5.1}$$

where t_{in}, t_{jn} and t_{kn} are raw times of the three D counter bins in the event and the sum is done over events where bin i is present. After that the procedure was repeated but with the raw times of each bin corrected by T_i. This iterative process was stopped when neither of the corrections was larger than 50psec.

These corrections were used in the event reconstruction to adjust the D counter timing after the tracks were found in the spectrometer. The resulting D counter timing resolution was found to be about $0.9ns/\sqrt{2} = 0.6ns$ (Figure 5.1).

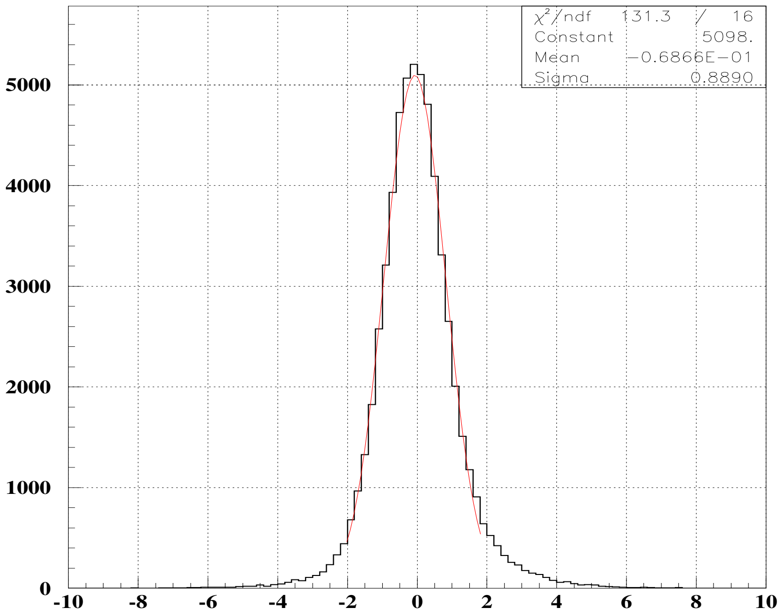

Figure 5.1: Difference of the time of the two D counter hits after timing correction.

5.4.2 Cerenkov counters

Both ADC and TDC information was collected for each of the 32 Cerenkov PMTs. The discriminator threshold was set at about 30% of the one photoelectron peak and a

$20ns$ gate was used for the ADC. Information from the auxiliary Cerenkov electronics was not used in this analysis.

ADC pedestals for each channel were obtained from out-of-time hits (the ones not associated with an event associated particle crossing the apparatus).

Since the E865 experiment uses common start TDCs the average timing of the D counter hits was used as a time reference for the other detectors. Each of the photomultipliers in the Cerenkov counters was calibrated to take into account the slewing (time dependence on the amplitude of the signal) correction. Data events with reconstructed e^+e^- pairs were used for this purpose. The time distribution of the Cerenkov hits in C1L after correction is shown in Figure 5.2. Taking into account the fact that the time reference used was typically the average three D counters we can estimate the time resolution of the Cerenkov counters to be about $\sqrt{0.74^2 - (0.6/\sqrt{3})^2} = 0.65ns$.

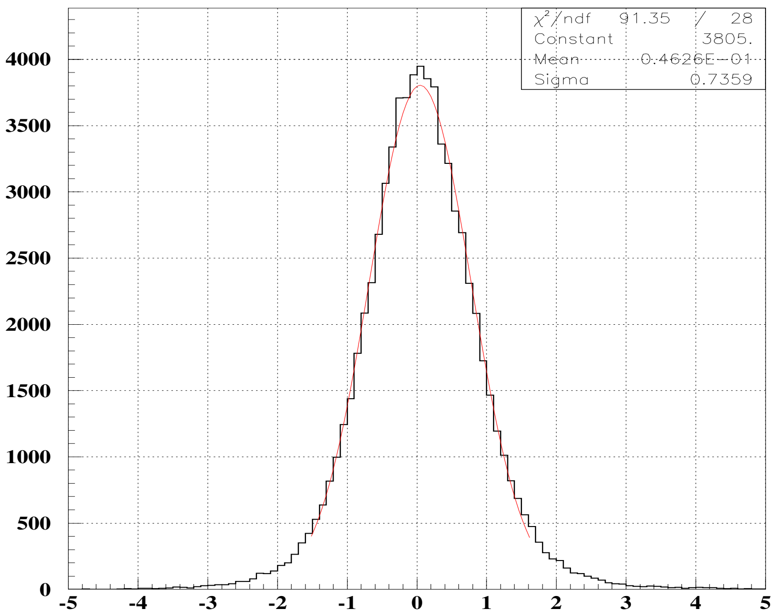

Figure 5.2: Time distribution of the C1L hits (difference of the Cerenkov signal with respect to the reference time, typically three D counters), after correction for the time dependence on the amplitude.

The Cerenkov ADC and TDC calibrations were used in the data reconstruction and in the Monte Carlo simulation and reconstruction.

5.4.3 Electromagnetic calorimeter

ADC pedestals of the calorimeter were obtained from special runs taken without the calorimeter sparcification. The gain calibration was done by matching the calorimeter response of electrons and positrons from the data to their momentum measured in the spectrometer. Both pedestals and gains were determined separately for each calorimeter module.

The timing calibration was performed in the same way as for the D counters and included a slewing correction.

5.5 Efficiencies

5.5.1 Proportional Wire Chambers

Track reconstruction (as described in Section 4.2) required at least three out of four PWCs to have space points and each space point required at least three out of four wire planes to be hit. Such a redundancy allowed use of the reconstructed data events to extract PWC efficiencies.

Efficiencies were measured for ten wire bins for each of the four planes of each chamber. Separate efficiency maps were obtained for electrons/positrons and pions/muons. Measured average efficiencies and individual wire bin efficiencies for pions and electrons are shown in Figures 5.3 and 5.4. Inefficiencies for pions/muons were found to be about 40% larger than for electrons/positrons. This difference is caused by about 50% more initial ionization produced in the PWC gas by electrons than by pions (for particles in the typical momentum range of 1 to 3 GeV/c).

Efficiencies of PWC3 and PWC4 were measured to be significantly lower than those of PWC1 and PWC2. Variation of efficiencies was found to be as large as $(10-20)\%$ between individual wires in PWC3 and PWC4. Efficiencies of some wires were as low as $(60-70)\%$ and average efficiencies of PWC3 and PWC4 wire planes were at the level of 90%; however it is important to note that for the collected Ke3 data sample, the resulting inefficiency of reconstructing three track events was at the level of only 1%. This is explained by the redundancy of the information collected by PWCs and is discussed in Section 9.4.

5.5.2 Scintillator Hodoscopes

The efficiencies and positions of the individual D counter slabs in 1998 were obtained using the Cerenkov efficiency trigger, which did not require the D counter. Near the photomultipliers, inefficiencies are less than 1-2% for all individual D counters. Due to smaller pulse-heights, and attenuation of pulses arising far from the photomultipliers, inefficiencies in the tips of a few counters were as high as 10-20%. Measured

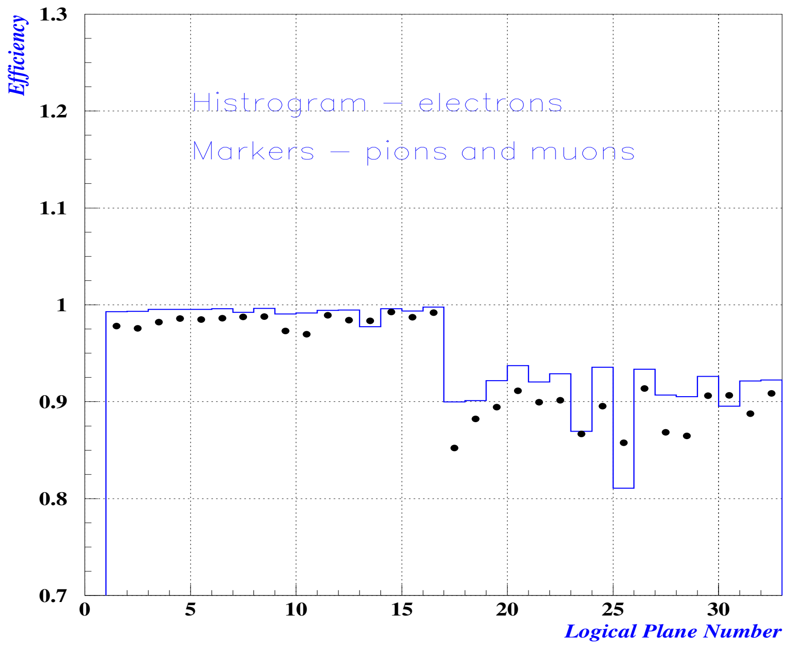

Figure 5.3: Measured efficiencies of the thirty two PWC logical planes. Logical planes are defined by dividing each of the sixteen sensitive planes into the left and right (relative to the beam) halves.(add PWC on the pic)

inefficiencies are presented in Figure 5.5.

5.5.3 Cerenkov Counters

The Cerenkov counters' performance was critical for the Ke3 measurement. Special $CERENK$ trigger events were collected for the purpose of obtaining these efficiencies from the data. The only trigger requirement was to have hits in at least three out of four Cerenkov counters. From the collected $CERENK$ trigger events we selected the ones that had a low mass e^+e^- pair and the second positive track was not a positron. In order to measure the efficiency of a given counter, we required the two tracks with low invariant mass to be identified as electron/positron in the other three Cerenkov counters and in the calorimeter. The second positive track was required to be identified as a pion or muon in the calorimeter. For events selected in this way (candidate events), we defined the Cerenkov counter in question to be inefficient if it had signal below 0.5 photoelectrons or time outside of $\pm$5ns window (cuts opposite to the ones used to identify electron/positron in the Cerenkov counters).

Cerenkov efficiency varied as a function of the four-dimensional phase space $(X; Y; \theta_X; \theta_Y)$ as a result of local variations in the mirror alignment and mirror reflectivity. Phase-space variation of the Cerenkov efficiency was measured and taken into

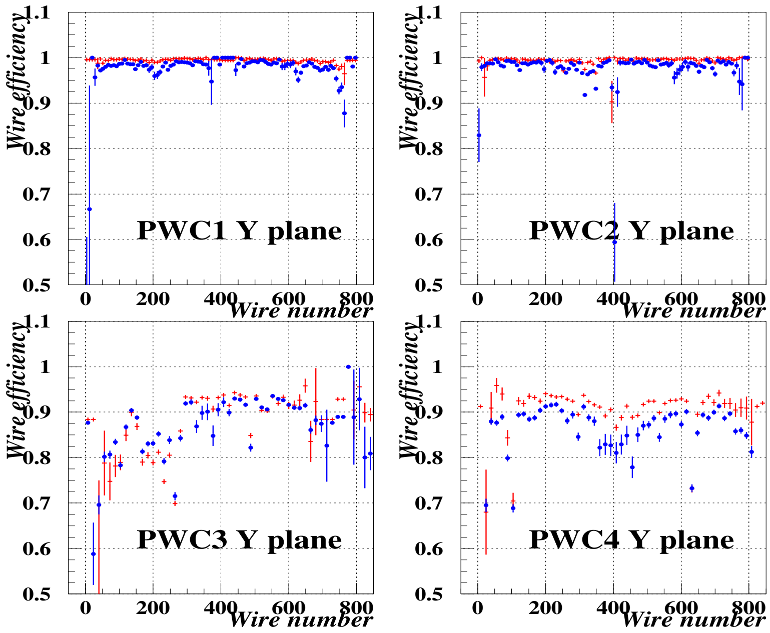

Figure 5.4: Measured wire efficiencies of the Y plane wires of the four PWCs. Circles show efficiencies for pions and muons. Crosses show efficiencies for electrons and positrons.

account by dividing candidate events into nonuniform bins in the four-dimensional space. Two considerations were taken into account when deciding on the number and sizes of the bins. First, efficiency inside each bin should be as close to constant as possible; second, the number of candidate events in each bin should be large enough to minimize the statistical uncertainty of the measured efficiency.

We used a segmentation with the total of 1920 bins (10 in X; 8 in Y; 6 in θ_X; 4 in θ_Y). The candidate event sample was about 50,000. It is important to note that electron and positron tracks coming from kaon decays occupy only part of the available four-dimensional phase-space, and thus most of the 1920 bins were empty. This, combined with the fact that the part of the phase-space filled by the candidate tracks is very close to the one occupied by the electrons and positrons that we identified in the Ke3 analysis, allowed us to have sufficient statistical accuracy inside the bins.

Bin borders were defined by looking at the measured Cerenkov efficiencies in 10cm$\times$10cm bins in X and Y and defining bins in X and Y in such a way that efficiency inside each bin would be as uniform as possible. Bins in θ_X and θ_Y were defined to describe in the best way the variation of optical acceptance with the angle of incident photons.

Tables 5.1 and 5.2 show average efficiencies in the chosen X;Y bins for C1 and C2

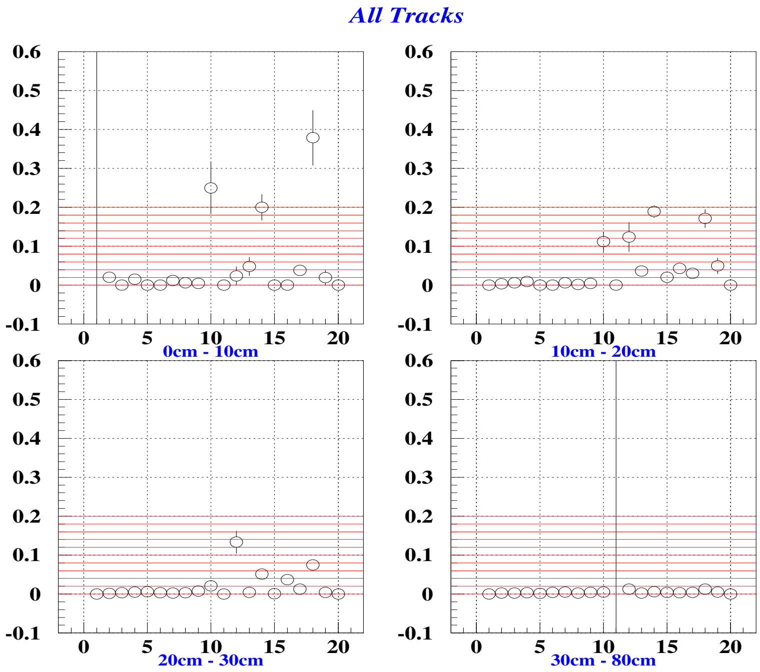

Figure 5.5: Measured inefficiencies of the D hodoscope scintillator slabs. Four plots show inefficiencies for the tracks crossing in the particular range in X (coordinate along the slab with zero at the edge furthest from the PMT) for all twenty slabs.

respectively. Zero efficiencies correspond to the blinded regions close to the beam; to the regions that were cut offline or to bins with no statistics. Low efficiencies in some bins are explained either by bins being on the border of adjacent mirror assemblies (alignment problems) or by the distorted (caused by accidental over-inflation) beam-tubes obscuring part of the optics.

A slight variation of the efficiency map binning was used to assess the systematic effects connected with the variation of efficiencies inside the bins (Section 10.4).

Efficiencies of the four Cerenkov counters averaged over all candidate events are

Table 5.1: Average efficiencies of C1 in percent as a function of track's position at the mirror plane. The upper row and the leftmost column show the bin borders in cm.

	-150;-110	-110;-90	-90;-35	-35;-20	-20;-10	0;10	10;30	30;90	90;110	110;150
60;20	98.0	96.5	99.3	98.3	92.3	00.0	95.1	99.9	99.3	99.7
20;15	95.6	95.9	99.4	97.6	92.7	00.0	96.9	99.9	99.3	99.7
15;7.5	87.7	93.5	98.9	98.5	96.4	00.0	95.8	99.9	98.6	100
7.5;0	90.1	95.8	99.3	00.0	00.0	00.0	100	99.3	99.4	100
0;-7.5	90.0	94.7	99.2	00.0	00.0	00.0	100	99.8	98.8	99.7
-7.5;-15	96.8	96.5	99.7	93.9	48.2	00.0	88.1	98.9	97.9	100
-15;-20	99.8	98.3	99.5	97.7	91.2	00.0	96.0	99.2	99.1	100
-20;-60	99.5	98.3	98.8	99.6	99.0	00.0	10.0	99.9	98.4	99.7

Table 5.2: Average efficiencies of C2 in percent as a function of track's position at the mirror plane. The upper row and the leftmost column show the bin borders in cm.

	-160;-140	-140;-85	-85;-70	-70;-40	-40;25	-25;-10	10;20	20;80	80;100	100;160
80;50	100	99.5	98.7	100	100	100	100	99.9	99.5	99.2
50;40	000	98.6	95.9	99.6	99.8	98.2	100	99.0	99.4	98.7
40;30	100	100	94.8	99.3	99.8	98.7	100	99.9	99.8	00.0
30;0	96.8	99.9	99.4	99.8	99.8	99.6	100	99.9	100	99.8
0;-30	94.4	99.4	98.7	99.3	94.0	87.1	9.72	99.8	99.8	99.9
-30;-40	90.0	99.3	94.2	98.8	91.8	87.8	9.57	99.7	100	99.9
-40;-50	100	98.7	81.4	99.4	88.8	91.2	9.09	99.7	98.2	99.5
-50;-80	000	97.6	82.1	99.8	98.5	97.6	000	99.7	100	99.6

presented in Table 5.3.

Table 5.3: Efficiencies of the four Cerenkov counters averaged over all candidate events

Counter	Electron detection efficiency
$C1Left$	0.9947 ± 0.0004
$C1Right$	0.9716 ± 0.0009
$C2Left$	0.9971 ± 0.0003
$C2Right$	0.9799 ± 0.0008

The statistical errors of the Cerenkov efficiencies were calculated as $\sqrt{e(1-e)/N}$, where e is the measured efficiency and N is the number of candidate events used for the measurement.

It is important to note that taking into account the importance of the Cerenkov efficiencies, I performed their measurement independently from the procedure used previously in the experiment and prepared by Professor Thompson. This procedure was then used for the Ke3 data and consistency of the obtained results was confirmed.

5.5.4 Electromagnetic calorimeter

Information from the calorimeter was used neither in the trigger nor in the event reconstruction. This allowed us to use reconstructed data for determination of the calorimeter efficiencies.

In each reconstructed event I looked at the time in the three calorimeter modules hit by the three reconstructed charged tracks. A module was declared inefficient if the ADC signal was above 100MeV and its time was more than 5ns away from zero or the time was inside ± 5ns and the ADC signal was less than 50MeV. Most of the calorimeter showed inefficiencies of less than 1% except for a few modules where inefficiency varied from 10% to 100% ("dead" modules). A map of the calorimeter efficiencies was constructed and used in the Monte Carlo simulation.

It is important to note that the calorimeter was used primarily only for the full reconstruction of the π^0, which in turn was done as a consistency check and was not required in the final analysis that produced the Ke3 branching ratio.

CHAPTER 6
MONTE CARLO SIMULATION

6.1 Overview

Accurate Monte Carlo simulation is a crucial part of this analysis, since we rely on it to provide us with sufficiently accurate acceptances for the different kaon decay modes detected by the E865 apparatus. Simulation was done in two stages. First, the specially written program KAY[26] based on the GEANT[27] simulation package available from CERN was used to simulate interactions of the kaon decay particles with the E865 apparatus and to write out simulated events in the format used for storing the real data. After that, an additional program called ZORA was employed to apply detector efficiencies obtained from the data. This two step procedure allowed us to use different versions of measuring and applying detector efficiencies without repeating the CPU-intensive task of event simulation. The final outcome of the simulation was a sample of stored events that were analyzed by exactly the same code as used for the real events analysis.

6.2 Simulation of initial kaons

In the early stage of the experiment, an attempt was made to simulate the beam-line and production of initial kaons using the program BETRAF [28] and alternatively GEANT itself. However, for either simulation method the reconstructed kaons from the $K^+ \to \pi^+\pi^+\pi^-$ decays failed to reproduce the data. Therefore, the observed kaon beam phase-space was used.

The kaons reconstructed from the collected $K^+ \to \pi^+\pi^+\pi^-$ events were used to construct a bank of initial kaons (called rayout) for the Monte Carlo. This approach resulted in much better agreement with the data. It is important to note that the use of real reconstructed kaons has two problems. Firstly, the distributions of reconstructed kaons are smeared by the finite reconstruction resolution and secondly, such distributions have non-uniform (with the respect to the beam phase-space) detector acceptance already convoluted into them.

The effect of smearing was most visible when comparing simulated and reconstructed distributions of kaon momentum from simulated $K^+ \to \pi^+\pi^+\pi^-$ events backtracked to the target. In order to account for this effect and to estimate its impact on the acceptance, for each of the five parameters (X;Y;θ_x;θ_y;P) I constructed the correction (6.1):

$$\delta R(R_{SIM}) = R_{SIM} - R_{REC} \tag{6.1}$$

where R_{SIM} is the simulated value of the parameter and R_{REC} is the reconstructed one. Corrections were obtained separately for all five parameters by binning the simulated data at the target and calculating average shift of each bin as a result of the reconstruction.

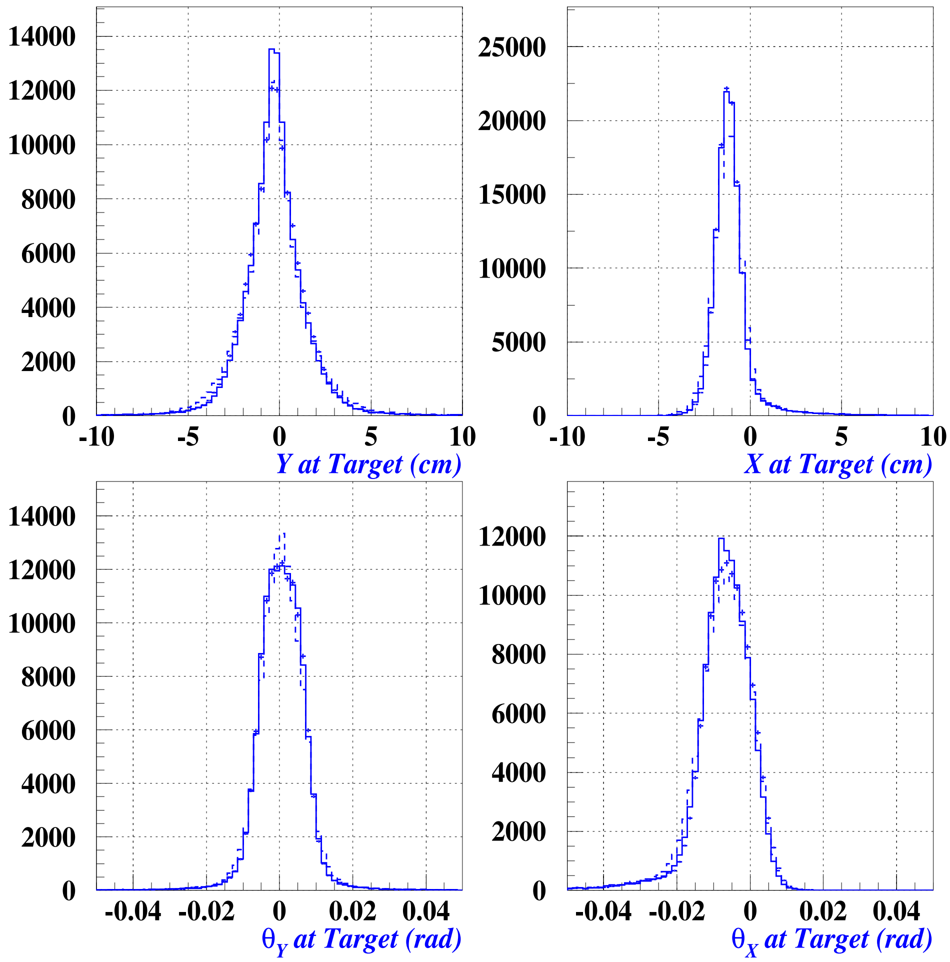

Figure 6.1: Position and angles at the target of kaons reconstructed from $K^+ \rightarrow \pi^+\pi^+\pi^-$ decays. Data is shown by points with errors; Monte Carlo by the dashed line; Monte Carlo corrected for the smearing effect by the solid line.

After all five correction maps were obtained, the next simulation of $K^+ \rightarrow \pi^+\pi^+\pi^-$ events was performed; original rayout kaons were backtracked to the target, corrected using the five maps independently, tracked to the beginning of the decay volume and only after that allowed to decay. While such a method produced better agreement between data and Monte Carlo for the kaons backtracked to the target (as expected from the nature of the correction), the agreement of the reconstructed kaons at the vertex became worse (Figures 6.1 and 6.2). This might be explained by not taking into account correlations between the five parameters of a kaon in the process of making correction at the target.

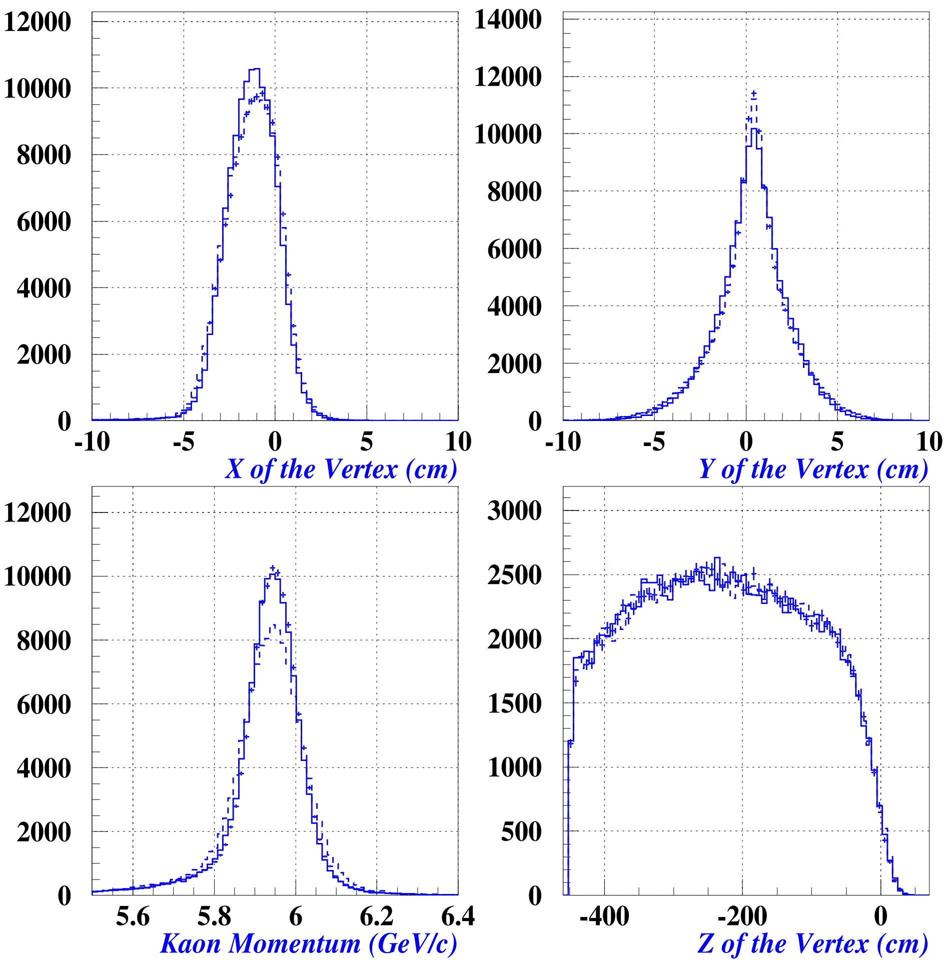

Figure 6.2: Position and momentum at the decay vertex of kaons reconstructed from $K^+ \to \pi^+\pi^+\pi^-$ decays. Data is shown by points with errors; Monte Carlo by the dashed line; Monte Carlo corrected for the smearing effect by the solid line. The correction for the smearing effect was not used in the final analysis.

It is important to note that the overall acceptance for the Monte Carlo events simulated with and without the correction differed by less than 0.3% and was within the statistical precision of the Monte Carlo sample used for this test. In the light of such a small change in the acceptance as well as worsening of data to Monte Carlo agreement at the vertex, and taking into account the fact that the Ke3 analysis did not require a good quality for the kaon's position at the target (necessary for some of the other decays analyzed in the experiment), I decided not to use these corrections.

Sensitivity of the simulated acceptance to the particular choice of the criteria used to select the $K^+ \to \pi^+\pi^+\pi^-$ rayout data sample was studied The acceptance was found to be stable within 0.1% under the variation of the selection criteria.

The weak dependence of the acceptance on the variation of the initially simulated beam profile is due to the fact that the acceptance is determined by the individual particles' kinematics which has much larger spread than the beam itself. Therefore, on the average, the final particle kinematics is only weakly coupled to the direction of initial kaon.

6.3 Simulation of the kaon decays

6.3.1 Simulation of the initial phase-space densities

Each of the pertinent kaon decay modes was simulated in a separate batch. In order to do so, in GEANT a "new" particle with the same properties as a standard K^+ was created, and forced to decay before reaching a certain point in Z (Zth=100cm; see Figure 9.2).

Each event of a certain mode was simulated according to the correct matrix element squared using the rejection-acceptance method (with some of the decay parameters simulated first according to the approximate dependence of the matrix element on them in order to increase simulation efficiency and accuracy). Appropriate experimentally measured form-factors (from [2])) were used for the matrix element calculation. Events were simulated initially in the rest-frame of the kaon and then transformed to the laboratory system according to the momentum of the kaon taken from the previously prepared rayout file.

Variation of the simulated Ke3 decay acceptance was observed to be $\pm 0.1\%$ when I varied the form-factor slope λ_+ used in the simulation within its current experimental uncertainty.

6.3.2 Simulation of the radiative correction

Radiative corrections for two decay modes were included in the Monte Carlo.

For the Dalitz decay $\pi^0 \to e^+e^-\gamma$, radiative corrections were taken into account according to [30] in the form of tabulated corrections to the phase-space density of the simulated events.

In the Ke3 analysis I did not attempt to separate $K^+ \to \pi^0 e^+ \nu\gamma$ events either by photon veto or by kinematic constraint. That meant that I had to simulate full radiative corrections. In order to do that, I divided all $K^+ \to \pi^0 e^+ \nu\gamma$ events into two parts. First was inside the two-dimensional $(E_e; E_\pi)$ region determined by three particle Ke3 kinematics and included soft real and virtual photons. Second was outside of this region and included "hard" real photons. For the first part I used standard Ke3 matrix element corrected according to [12]. For the second part I simulated $K^+ \to \pi^0 e^+ \nu\gamma$ events [29] . For the $K^+ \to \pi^0 e^+ \nu\gamma$ events I did not use a lower limit on the photon energy or angle; instead, I required Ke3γ events to be outside of the Ke3 Dalitz plot when projected to the $(E_e; E_\pi)$ plane. The relative weight of the two parts was determined from the generators themselves (by doing numerical integration). The Ke3γ part was found to constitute only about 0.5% of the total Ke3 decay rate.

In practice I used the standard Ke3 generator (without any radiative corrections). Weights reflecting virtual and soft "real" radiative corrections were calculated and stored for each event; they were applied at the stage when acceptance was calculated. Ke3γ events were simulated separately and added to the Monte Carlo mix with the correct relative weight.

6.4 Simulation of the apparatus and physical processes

All of the E865 detector apparatus was included in the simulation using tools provided by GEANT. Each detector element was included using its dimensions and materials. Positions of individual detector subsystems were taken from the same data file used in the Monte Carlo reconstruction. From the spatial distributions of the reconstructed real events it was discovered that the downstream edge of the decay volume is shifted up by a few centimeters resulting in asymmetric (top to bottom) geometric acceptance. Instead of an additional software cut, a new survey of the decay volume position was requested and performed by the AGS survey team. Using the results of this survey, I changed the positions of the decay volume in the Monte Carlo. This resulted in an improvement of the agreement between data and Monte Carlo distributions.

Using GEANT we simulated the following processes:

- Multiple Scattering according to Moliere formula

- Continuous energy loss due to ionization

- Photo-electric effect
- Compton scattering
- Bremsstrahlung
- Delta-ray production
- Positron annihilation
- Cerenkov radiation
- Pair production by photon
- Hadronic interactions using the GHEISHA package

All of the particles were tracked by GEANT until they reached $1MeV$ energy. While this threshold was arguably high for the simulation of hadronic interactions in the calorimeter, and the simulation of the hadronic interactions was not fine-tuned, the very limited use of the calorimeter information in the Ke3 analysis allowed me to use it and greatly reduce the CPU load (compared to using lower energy cutoff).

An event simulation was stopped if one of the charged particles failed to reach the A counter. This cut avoided use of CPU time for events that would not be reconstructed, as most of the events that do not pass through the A counter aperture also miss the sensitive regions of either PWCs or Cerenkov counters. As a result of this requirement the CPU time per simulated event decreased from about 1sec to 0.37sec. A corresponding geometric cut was applied to both reconstructed data and Monte Carlo and a sample of Monte Carlo events without this requirement was simulated and showed no significant bias in acceptance.

6.5 Simulation of the detector response

6.5.1 Proportional wire chambers

In order to simulate the PWC response, the entry and exit coordinates of the charged track as it crosses the sensitive region of each PWC wire plane were calculated. Coordinates were calculated in the direction perpendicular to the wires of this plane. The wire hit was registered if any of these two coordinates were closer than 1mm (half a wire separation space) to the wire. The initial simulation assumed sensitive region for each plane to have width of 1cm in Z direction. While this corresponds well to the gap between plates, this procedure produced significant discrepancy between data and Monte Carlo in the number of wires hit by a single track in a single wire plane (Figure 6.3). Monte Carlo predicted many more two-wire hits than was observed in the data. At the same time, there was a marked discrepancy in the track reconstruction χ^2. I reduced the depth of the sensitive region in such a way as to give consistent multiplicity of the number of wires in a PWC hit between simulation and data. This change led to only a negligible change in the acceptance but significantly improved agreement of track χ^2 between data and Monte Carlo (Figure 6.3). Such a change is physically justified by the measured PWC efficiencies being lower than the expected 99%, which in turn can be described by reduction of the sensitive volume.

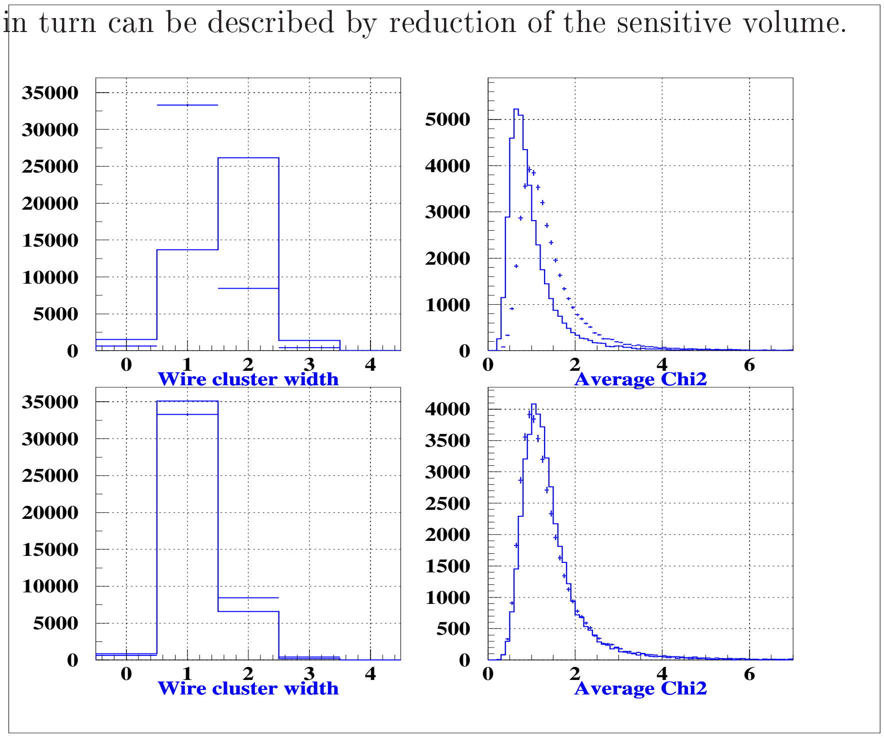

Figure 6.3: The figure shows number of wires in the wires cluster in the X view of PWC1 and the average of the three charged track χ^2/ndf. Upper plots are for the conventional Monte Carlo. Lower plots are for the Monte Carlo with the reduced width of PWC sensitive region. Histogram represents Monte Carlo, while points with errors represent data.

PWC wire efficiencies obtained from the data were applied for each wire hit depending on the wire number and on the type of the particle (separate efficiency maps for electrons and for pions/muons).

6.5.2 Cerenkov counters

The simulation of the Cerenkov counter's response to electrons/positrons had two components. First, the total number of photoelectrons detected by Cerenkov PMTs was simulated. This was done by first locating which bin of the four-dimensional efficiency map (Section 5.5.3) is occupied by the track. The corresponding efficiency was converted into an average number of photoelectrons using Poisson statistics. The second step was to determine by which PMTs these photoelectrons are detected. As described in Section 2.5.1, each Cerenkov PMT "sees" a certain area in the (X;Y) plane, except for C2, where some of the X;Y regions are actually seen by two PMTs, each sensitive to a restricted range of track angles. The light from a track can also be detected in more than one PMT if the track is close to the border between adjacent mirror assemblies. In such a case, the light is "shared" between different PMTs in the proportion defined by the Cerenkov cone position and distribution of photons inside it. As the Cerenkov photons were not traced in the Monte Carlo used for the Ke3 analysis, I extracted information about sharing from the data. To do so, I first selected Kpi2 events using only the calorimeter to identify pions. I required these events to have π^+ and e$^+$ in different but adjacent mirror assemblies. In such events, pions might be identified as positrons if the real positron is closer than approximately 5cm (typical radius of Cerenkov cone at the primary mirror plane) to the border between mirror assemblies, so that part of Cerenkov light is "shared" with the PMT looking at the pion. I obtained the dependence of the probability of such misidentification as a function of positron's distance from the border. This dependence was used in the Monte Carlo to divide the number of photoelectrons between different PMTs if an electron/positron track was within $\pm 5cm$ from the border (Figure 6.4). At this point in the simulation, we know how many photoelectrons are detected on average in each PMT. The exact number of photoelectrons was simulated for each PMT according to the Poisson distribution with this average. If the resulting integer number was above zero, it was smeared with a gaussian distribution providing a continuous spectrum.

It is important to note that if, after smearing, the number of photoelectrons was less than 0.5 (threshold used for efficiency determination and for the e$^+$/e$^-$ PID), the smearing was done again until the result was above 0.5 photoelectrons. This method insured that the PID efficiency of the Monte Carlo will be the same as for the data if 0.5pe is used as a threshold. Thus, the final procedure was aimed at the correct simulation of the Cerenkov counters' response to e^+/e^- originating from kaon decays (i.e. with the energy far above Cerenkov radiation threshold of about 60MeV in methane). The photoelectron yield for such particles depended primarily on the

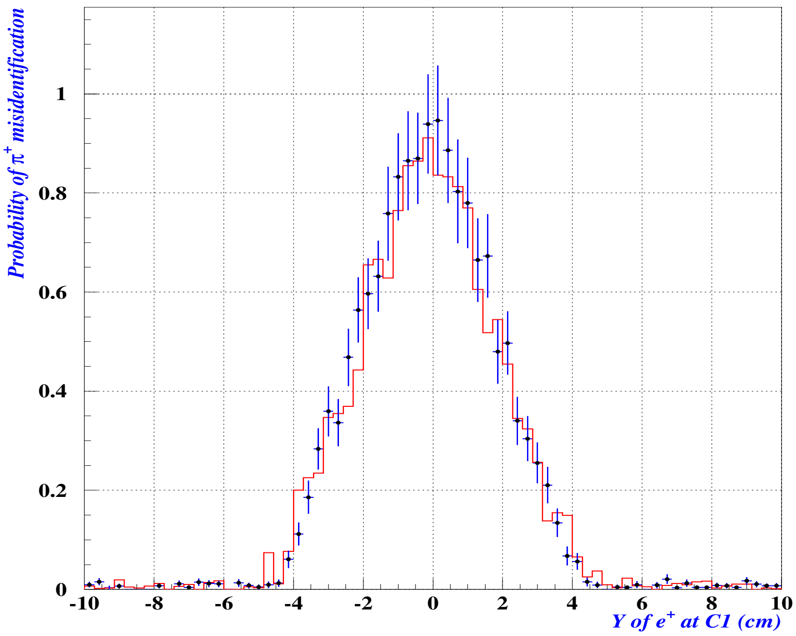

Figure 6.4: The probability of pion misidentification as positron in the Cerenkov counters (due to the light sharing between mirrors) as a function of the distance of the positron to the border between mirrors. In this case, the pion always hits the mirror adjacent to the one hit by the positron. Markers with errors represent data; histogram represents Monte Carlo.

Cerenkov photon absorption in the gas, mirror reflectivity, the counters' optics alignment, and on the photomultipliers' quantum efficiency; but was almost independent of the particle's energy.

Unfortunately, this approach was not very suitable for the simulation of the counters' response to pions and muons, which is due primarily to scintillation and δ-electrons. Delta electrons were produced in the Monte Carlo but the Cerenkov response for them was simulated in the same way as for electrons from kaon decays, i.e. without taking into account their much smaller energies and smaller path-length inside the counters. This inaccuracy in the simulation led to systematic uncertainties in the calculated (from Monte Carlo) efficiency of pions and muons particle identification and in the estimate of the selected Ke3 sample contamination due to pion/muon misidentification as positron. The uncertainty in π^+/μ^+ PID was greatly reduced by selecting a pion/muon as a particle that does not have response in *both* Cerenkov counters (Section 7.2.4). The uncertainty in the Ke3 sample contamination was estimated to be small compared to the other systematic errors (Section 8.2).

6.5.3 Scintillator hodoscopes

Scintillator hodoscopes were simulated to be 100% efficient. No ADC information was simulated for scintillators, and any charged track was assumed to have left a TDC hit. Efficiencies obtained from the data were applied at the reconstruction stage.

6.5.4 Electromagnetic calorimeter

The calorimeter response depends on the energy loss in the radiator and in the scintillator, attenuation of light in the fibers, and photomultiplier response.

The transformation of ionization losses into photons in scintillator was described by the well known semi-empirical model called Birks's law[31, 32] (Equation 6.2).

$$\frac{dL}{dx} = A\frac{dE}{dx}\left[1 + B\frac{dE}{dx} + C\left(\frac{dE}{dx}\right)^2\right]^{-1} \tag{6.2}$$

where $\frac{dL}{dx}$ is the light per unit path length, A is the scintillator efficiency, B and C are parameters for Pilot-B scintillator taken from [33] and used to simulate the scintillator of the E865 calorimeter.

The light yield was then corrected (reduced) taking into account the exact position of the hit with the respect to the center of the scintillator plate. Exponential attenuation in fibers was applied (taking into account both "long" and "short" components of attenuation). Fiber-to-PMT coupling was assumed to be linear. Additional smearing due to the photoelectron statistics on PMT dynodes was introduced in the form of

$$\frac{\sigma_E}{E} = \left[a^2 + \frac{b^2}{E}\right]^{1/2} \tag{6.3}$$

with parameters a and b taken initially from [25] and fine-tuned later by comparing data with Monte Carlo.

6.6 Digitization of the simulated detector response

The final stage of an event simulation was the conversion of the simulated detector response into the format of the E865 event record. To assure correct reconstruction, the simulated amplitudes and times were converted into ADC and TDC channels using the calibration data files and exactly reversed procedures that were used for data and Monte Carlo reconstruction. Time response was not simulated: time in the

Monte Carlo events was equal to zero for efficient hits and was absent (TDC overflow) for inefficient ones.

6.7 Addition of accidentals to the Monte Carlo simulation

Accidental tracks/hits are tracks/hits in the collected data that were accidentally close in time but were not in any way connected with the kaon decay we are trying to identify. Accidental hits can affect the data in different ways: an accidental hit in the Cerenkov counter can lead to π^+ misidentification as e^+, accidental hits/tracks in the spectrometer can disturb track and vertex reconstruction; a reconstructed accidental track might even be reconstructed to have a common vertex with, for instance, the e^+e^- pair from π^0 decay, thus faking the three track event.

In order to add accidental hits to the Monte Carlo, I selected good $K^+ \to \pi^+\pi^+\pi^-$ events from the data using only kinematic cuts. For each of these events, all PWC and calorimeter hits that formed the reconstructed $K^+ \to \pi^+\pi^+\pi^-$ decay were removed from the event record. Events "stripped" in this manner were written out into a separate file that was later merged with the simulated data at the event record level. ADC signals from the "stripped" file were added to the simulated ADC signals; "stripped" TDC signals replaced the simulated ones if they were smaller (earlier in time). PWC wire hits from the "stripped file" were superimposed on the simulated ones.

The merging procedure allowed addition of accidental hits in different systems of the detector in a selective way (for instance only hits in PWCs).

For the final analysis, accidental hits in PWCs were added to all simulated decay modes, while accidental hits in the Cerenkov counters were added only for the purpose of the π^+/μ^+ identification, i.e. they were not taken into account when the simulated electrons or positrons were identified. Note that any effect accidental hits had on the Cerenkov efficiencies was already taken into account by efficiency measurement; therefore, overlaying of the simulated electron/positron signal by accidentals would have been wrong.

CHAPTER 7
EVENT SELECTION

7.1 Overview

As described in Section 1.4, our main goal was to measure the ratio

$$\frac{BR(K^+ \to \pi^0 e^+ \nu)}{Kdal} = \frac{N_{Ke3}/Acc^{Ke3}}{N_{Kdal}/Acc^{K\pi2}} \tag{7.1}$$

$$\begin{aligned} Kdal = \quad & BR \quad (K^+ \to \pi^+ \pi^0) \\ +(Acc^{K\mu3}/Acc^{K\pi2})\times \quad & BR \quad (K^+ \to \pi^0 \mu^+ \nu) \\ +(Acc^{K\pi3}/Acc^{K\pi2})\times \quad & BR \quad (K^+ \to \pi^+ \pi^0 \pi^0) \end{aligned} \tag{7.2}$$

where N_{Ke3} and N_{Kdal} are the numbers of data events for the signal and normalizer respectively, and Acc^{PROC} is the total acceptance for the decay mode $PROC$. While Equations 7.1 and 7.2 are only approximate (not including cross-contamination, accidental background and rare decays), they are adequate to give a general description of the goal of the experiment for the purpose of this Chapter overview.

As one can see, the selection criteria should be designed to select two samples from the data (Ke3 and Kdal). In choosing the exact selection mechanism, I was guided by three concerns. Firstly, I wanted to separate signal and normalizer as cleanly as possible to minimize both cross-contamination and contamination by background. Secondly, to have such a selection that would in general provide as little systematic uncertainty as possible, i.e. make sure that all the reconstructed parameters used in cuts are well simulated in the Monte Carlo. Thirdly, to have as little difference in selection criteria for signal and normalizer as possible; this will allow minimization (through cancellation) of the systematic uncertainties common for Ke3 and Kdal.

The first and second concerns will be mostly discussed in Chapters 8, 9 and 10 while in this Chapter I will state the final cuts that I arrived at (as being optimal) through the course of this analysis.

The third concern was initially addressed by the choice of the normalizer. As pointed out in Section 1.4, the π^0 is always detected through the decay $\pi^0 \rightarrow e^+e^-\gamma$; therefore, both signal and normalizer events always have three charged tracks from the common vertex, low mass e$^+$e$^-$ pair in the final state, plus an additional positive track which is either e$^+$ for the signal or π^+/μ^+ for the normalizer. As will be shown later (Chapter 8), an adequate signal/normalizer separation can be achieved without any kinematic cuts specific to a particular decay mode. This fact allowed me to have identical selection criteria for the Ke3 and Kdal samples, except for the particle identification of the second positive track (not e$^+$ from the low mass e$^+$e$^-$ pair).

It is important to note that Ke3 and Kdal events were selected from the collected $ELER$ trigger data sample.

7.2 Event Selection

7.2.1 Vertex cuts

My first concern was to select events with a good quality three track vertex located inside the decay tank. Such selection is important for decreasing the level of accidental three track events, where (for the case of Ke3 and Kdal) the e$^+$e$^-$ pair comes from one decay, while the second positive track comes from another or from the beam. It also eliminates three track events where one or more of the tracks were poorly reconstructed due to multiple scattering or pattern recognition problems in the spectrometer.

Two explicit cuts were applied to the $ELER$ data that passed $PASS1$ (three tracks with loosely defined common vertex are found).

The first cut required the vertex to be downstream from -350cm ($Zvtx > -350cm$). While the decays tank starts at -480cm, the large decrease of acceptance for the Ke3 and Kdal decays occurring far upstream resulted in about 80% efficiency of this cut (compared to cutting at -480cm and according to Monte Carlo); at the same time, this cut eliminated decays that occurred upstream from the decay volume but were wrongly reconstructed to be inside it. This elimination is important since the Monte Carlo “starts” kaons only from -490cm.

The second cut required a good quality vertex by cutting on the normalized missing distance $Snorm$ (Section 4.3). $Snorm$ was required to be less than 3cm, which corresponds to about 95% efficiency compared to the $S < 10cm$ cut used in $PASS1$ (according to Monte Carlo).

Both *Zvtx* and *Snorm* cuts were identical for the Ke3 and Kdal samples. Systematic effects connected with both cuts will be discussed in Section 10.3.

7.2.2 Fiducial Volume cuts

Fiducial volume cuts were designed primarily to assure that all the three tracks are crossing the sensitive regions of the detectors used for this analysis. This included the D counters, Cerenkov counters and the calorimeter. The largest (in terms of removed events) was the cut that required all three tracks to be outside of the beam holes in both Cerenkov counters. Events with tracks crossing beam holes in the D counters and in the calorimeter were also excluded.

An event was also rejected if any of the tracks was too close to X=0cm in either of the Cerenkov counters. This cut was required by the absence of primary mirrors in this region and low Cerenkov counter efficiency at the aperture edge.

I decided to include here a description of the Cerenkov Ambiguity Cut(CAC). This cut, while not connected to the overall fiducial volume, is based solely on the coordinates of the tracks.

Cerenkov counters in E865 were used to separate electrons (positrons) from pions and muons. The finite granularity of the Cerenkov counters (four and twelve photomultipliers per one side of the first and second Cerenkov counter respectively), made the particle identification ambiguous when more than one track traversed the area of the Cerenkov counter viewed by a given photomultiplier.

Inclusion of such ambiguous events in the analysis would have resulted in a substantial (order of 10%) contamination of the selected Ke3 sample by the Kdal decays. More importantly this contamination was strongly dependent on both sharing of Cerenkov light between adjacent mirrors (Section 6.5) and calorimeter response to pions. The latter is inherently difficult to simulate, as it includes simulation of hadronic interactions. Taking these considerations into account, I decided to reject events where any one Cerenkov PMT might detect photons from more than one track. The Cerenkov Ambiguity Cut and was based solely on the X;Y coordinates of the tracks at the primary mirror planes of two Cerenkov counters. The CAC reduces the combined sample of all Dalitz events (Ke3+Kdal) by almost 30%. At the same time, the remaining sample was still adequate to obtain statistical accuracy of less than a percent. Study of implications of CAC on the systematic uncertainty (Section 10.3) showed that application of this cut does not produce significant systematic bias and in fact reduces the systematic error.

7.2.3 Low mass e^+e^- pair cuts

After selection of good quality three track events with all tracks crossing the sensitive regions of the detector and no ambiguity in the Cerenkov response, the next step was to identify events with a low mass e$^+$e$^-$ pair. The cut used to do this consisted of three stages. First, out of the two possible combinations of negative/positive track pairs, I selected the one that had the lowest Mee (invariant e$^+$e$^-$ mass) and required its Mee to be below $0.05GeV$. Second, both tracks in the selected pair were required to have electron PID in both Cerenkov counters. Particularly:

$$\begin{array}{rrcccl} & PE_{e^-}^{C1L} & > & 0.5pe & .AND. & |T_{e^-}^{C1L}| < 5ns \\ .AND. & PE_{e^-}^{C2L} & > & 0.5pe & .AND. & |T_{e^-}^{C2L}| < 5ns \\ .AND. & PE_{e^+}^{C1R} & > & 0.5pe & .AND. & |T_{e^+}^{C1R}| < 5ns \\ .AND. & PE_{e^+}^{C2R} & > & 0.5pe & .AND. & |T_{e^+}^{C2R}| < 5ns \end{array} \tag{7.3}$$

where $PE_{e\mp}^{CK(L/R)}$ is the number of photoelectrons associated with the electron/positron in the Left/Right side of Cerenkov counter K (K = 1 or 2) respectively, and $T_{e\mp}^{CK(L/R)}$ is the corresponding Cerenkov time. Note that the cuts used are exactly the same as the ones used to determine Cerenkov efficiency in Subsection 5.4.1. It is also important to point out that since positive and negative tracks are required to be on the Right and Left sides of the apparatus, the PID cut on the low mass e$^+$e$^-$ pair simultaneously requires each of the four Cerenkov counters to have at least one in-time hit. This requirement repeats the $ELER$ trigger requirement, thus making sure that the trigger was caused by the selected event and emulating the trigger for the simulated Monte Carlo events.

7.2.4 Particle identification of the second positive track

Particle identification of the second positive track is the point in the selection process where selection criteria for Ke3 and Kdal begins to be different. For Ke3, the second positive track is e^+, while for Kdal it is π^+ or μ^+.

π^+/μ^+ identification

The obvious particle identification for π^+/μ^+ was to require no in-time hits in both Cerenkov counters: (0/2) PID:

$$\begin{aligned} & (PE^{C1R}_{(\pi/\mu)^+} &<& \; 0.5pe \quad .OR. \quad |T^{C1R}_{(\pi/\mu)^+}| > 5ns) \\ .AND. \quad & (PE^{C2R}_{(\pi/\mu)^+} &<& \; 0.5pe \quad .OR. \quad |T^{C2R}_{(\pi/\mu)^+}| > 5ns) \end{aligned} \tag{7.4}$$

Unfortunately simulation of this requirement in the Monte Carlo introduced a systematic uncertainty connected with inaccurate simulation of Cerenkov response to pions/muons (Section 6.5.2); addition of the accidental Cerenkov hits to the Monte Carlo (as described in Section 6.7) will also introduce an error, as the added accidental hits actually include Cerenkov hits produced by pions from the data $K^+ \to \pi^+\pi^+\pi^-$ decays used to obtain the accidentals.

In order to estimate the uncertainty connected with the above sources I compared the efficiency of the requirement from Equation 7.4 when applied to π^+ from the real and simulated $K^+ \to \pi^+\pi^+\pi^-$ events. The results are presented in Table 7.1.

Table 7.1: Efficiency of different pion/muon PID requirements when applied to π^+ from the real and simulated $K^+ \to \pi^+\pi^+\pi^-$ events. Errors are determined by statistics only.

	(0/2) PID	.not.(2/2) PID
Data	$(99.03 \pm 0.04)\%$	$(99.87 \pm 0.01)\%$
Monte Carlo without Cerenkov accidentals	$(99.46 \pm 0.01)\%$	$(99.999 \pm 0.005)\%$
Monte Carlo with Cerenkov accidentals	$(98.64 \pm 0.01)\%$	$(99.910 \pm 0.005)\%$

As one can see from Table 7.1, Monte Carlo with added Cerenkov background will underestimate the efficiency of the described π^+/μ^+ PID by $(0.59 \pm 0.04)\%$. Unfortunately, this number can not be used directly as a correction to the efficiency of this cut when applied to other kaon decays, as this number is clearly affected by real accidental hits which are not evenly distributed, and thus will not affect decay modes with different kinematics in the same way.

An alternative way to identify the pion/muon is to define it as the track that does not satisfy the requirement of having in-time hits in both Cerenkov counters (.not.(2/2) PID). Such identification will have higher efficiency and will fail primarily if there was an accidental track that produced Cerenkov signal in both counters close to the original pion/muon. Comparison of .not.(2/2) PID for different samples is presented in Table 7.1 and shows that while there is still a difference between data

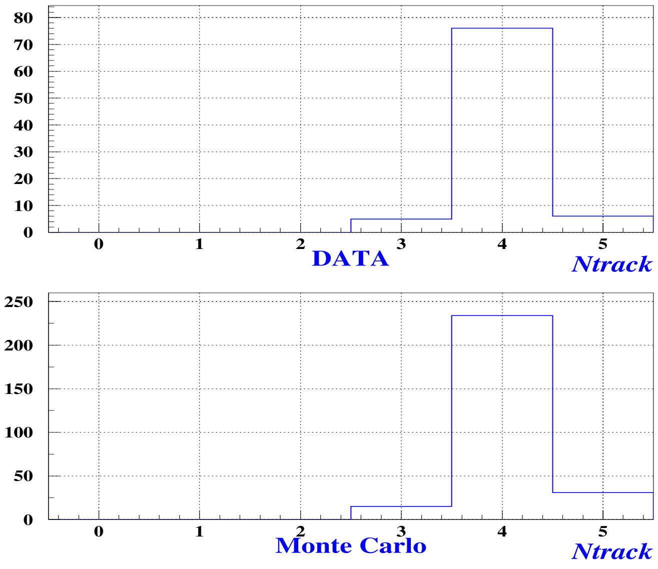

Figure 7.1: Number of reconstructed tracks for $K^+ \to \pi^+\pi^+\pi^-$ events where π^+ has in-time hits in both Cerenkov counters.

and Monte Carlo, its magnitude is only $(0.04 \pm 0.01)\%$ (for Monte Carlo with added Cerenkov background). One can also see from Figure 7.1 that most of $K^+ \to \pi^+\pi^+\pi^-$ events that fail this requirement do have an additional (fourth) track; their fraction depends very weakly on the Cerenkov response to pions/muons and therefore can be predicted with better accuracy. Fraction of events with more than three reconstructed tracks in the finally selected Ke3 and Kdal samples was about 10%, that corresponded well with the fraction of four track events in the selected *ktau* sample.

e^+ identification

Particle identification for the second e^+ from the Ke3 was done in the following two alternative ways. The first one (Equation 7.5) was identical to the PID requirements used to identify the low mass e^+e^- pair and was called $(2/2)PID$ (two out of two Cerenkov counters were required). It had the advantage of using information from the Cerenkov counters only, thus eliminating any systematic effects connected with the use of the calorimeter as an additional PID system. At the same time, the accuracy with which I could model the efficiency of such identification relied solely on my ability to model Cerenkov counters' efficiencies; as any inaccuracy of the model would translate directly into systematic inaccuracy of the final result.

$$\begin{aligned} PE^{C1R}_{e^+} &> 0.5pe \quad .AND. \quad |T^{C1R}_{e^+}| < 5ns \\ .AND. \quad PE^{C2R}_{e^+} &> 0.5pe \quad .AND. \quad |T^{C2R}_{e^+}| < 5ns \end{aligned} \tag{7.5}$$

Taking this into account, the alternative e^+ PID method was developed. It required at least two out of the three conditions from Equation 7.6 to be satisfied and was called $(2/3)PID$.

$$\begin{aligned} PE^{C1R}_{e^+} &> 0.5pe \quad .AND. \quad |T^{C1R}_{e^+}| < 5ns \\ PE^{C2R}_{e^+} &> 0.5pe \quad .AND. \quad |T^{C2R}_{e^+}| < 5ns \\ |E_{e^+}/|P_{e^+}| &> 0.8 \end{aligned} \tag{7.6}$$

where E_{e^+} is the energy deposited by the e^+ in the calorimeter and $|P_{e^+}|$ is its momentum magnitude measured in the spectrometer. While the $(2/3)PID$ did add calorimeter to the particle identification, it reduced the systematic uncertainty caused by inaccuracies in the modeling of the Cerenkov counter efficiencies. At the same time, the $(2/3)PID$ leads to the larger contamination of the selected Ke3 sample due to π^+/μ^+ misidentification as e^+. Detailed discussion of implications of these two cuts can be found in Section 10.4.

7.3 Summary

Table 7.2 contains a summary of the selection criteria used for the selection of the signal (Ke3) and the normalizer (Kdal) samples. Application of these cuts to the collected $ELER$ triggers resulted in about 70,000 Ke3 and 500,000 Kdal events.

Table 7.2: Cuts used to select the samples of Kdal and Ke3 events from the reconstructed $ELER$ triggers. The application of these cuts resulted in about 70,000 Ke3 events and 500,000 Kdal events. Note that $(2/2)PID$ and $(2/3)PID$ cuts were used alternatively and $(2/3)PID$ was used for the final selection.

Cut	Description	Selected samples	
		Kdal	Ke3
$Snorm < 3cm$	Vertex quality cut.	YES	YES
$Zvtx > -350cm$	Rejects upstream events	YES	YES
Aperture cut	Requires all three tracks to go through detector's sensitive regions	YES	YES
Cerenkov Ambiguity Cut (CAC)	Rejects events where any one Cerenkov photomultiplier could have detected Cerenkov photons from more than one track	YES	YES
e^+e^- PID	Requires in-time signals in both Cerenkov counters for the pair of negative and positive tracks that produces the smaller M_{ee} invariant mass	YES	YES
$M_{ee} < 0.05GeV$	Requires the invariant mass of the found e^+e^- pair to be small	YES	YES
e^+ $(2/2)PID$	The second positive track is required to have in-time signals in both Cerenkov counters (C1 and C2)	NO	YES
e^+ $(2/3)PID$	The second positive track is required to satisfy at least two out of the following three conditions: in-time signal in C1; in-time signal in C2; energy deposition in the Calorimeter consistent with the track's momentum: $(E/P) > 0.8$	NO	YES
π^+/μ^+ .not.(2/2) PID	Requirement opposite to the (2/2) e^+ PID	YES	NO

Table 7.3 shows how the number of events was reduced by the applied selection criteria.

At an early stage of the analysis I checked that the number of reconstructed three track events per AGS pulse agreed between the data and the Monte Carlo within statistical accuracy of the sample used for this check (about 10%). The large reduction

Table 7.3: Flow-chart of the data reduction by applied selection criteria

Selection criteria	Number of events
Collected $ELER$ triggers	37,676,459
Three tracks with the common vertex	2,851,581
Vertex, aperture, and Cerenkov Ambiguity cuts	710,486
$M_{ee} < 0.05GeV$	643,720
Low mass e^+e^- pair identification	625,727
$(2/3)e^+$ PID of the second positive track (Ke3 selection)	71,204

of the data by the geometric cuts was explained by removal of events which contained tracks traversing the beam-holes in the Cerenkov counters and by the Cerenkov Ambiguity cut. Implications of the aperture and the Cerenkov Ambiguity cuts, as well as the M_{ee} and particle identification cuts are discussed in Chapter 9.

CHAPTER 8
CONTAMINATION OF THE SELECTED SAMPLES

8.1 Overview

The goal of this experiment was to measure the $BR(K^+ \to \pi^0 e^+ \nu)/Kdal$ ratio defined in Equations 7.1 and 7.2; however, it is important to note that these equations are correct only for the case when we can select two samples of *only* Ke3 events and of *only* Kdal events. Unfortunately, such an ideal situation is not possible in practice, i.e. the selected Ke3 sample will always contain a number of non-Ke3 events. The same is true for the Kdal sample.

Contamination can be caused by different mechanisms. First, is the contamination due to incorrect identification of the kaon decay mode caused by particle misidentification (for instance π^+ is misidentified as e^+ and consequently $K^+ \to \pi^+\pi^0$ is misidentifies as $K^+ \to \pi^0 e^+ \nu$ decay). Second is the contamination due to the accidental tracks that might be reconstructed to have a common vertex with, for instance, an e^+e^- pair from π^0 decay, thus faking the three track event. Finally, some kaon decay modes that have more than three charged tracks in the final state can be reconstructed to have only three tracks and therefore misidentified as Ke3 or Kdal depending on their daughter particle species. Third, is the contamination due to the decays occurring upstream of the decay vaolume. Finally, the low mass e^+e^- pair can come not from the π^0 decay but from a photon conversion on the material of the detector.

8.2 Cross-contamination by kaon decays

The amount of contamination of the selected Ke3 sample by the other kaon decay modes depended strongly on the choice of e^+ PID method. Two methods were used: $(2/2)PID$ and $(2/3)PID$.

As was discussed in Section 7.2.4, only about 0.1% pions(muons) had in-time signals in both Cerenkov counters and therefore could be misidentified as e^+ if $(2/2)PID$ was used. Most of such occurrences were due to the presence of the fourth (accidental) track that produced a signal in both Cerenkov counters close to the trajectory of the pion(muon) and were simulated fairly well (with less than 0.1% discrepancy between predicted and observed misidentification of pions from $K^+ \to \pi^+\pi^+\pi^-$ decays). In fact, the misidentification probability is even smaller for Kdal events, since the majority of pions from Kdal decays are further away from the beam region than pions from $K^+ \to \pi^+\pi^+\pi^-$ decays. The use of $(2/2)PID$ resulted in about 0.5% contamination of the selected Ke3 sample due to pion/muon misidentification.

The probability of pion/muon misidentification as e^+ increased if $(2/3)PID$ was used for e^+ identification: with Cerenkov accidental hits added to the Monte Carlo, the resulting predicted Ke3 sample contamination reached above the 1% level. Taking into account problems with pion/muon Cerenkov response simulation (Sections 6.5.2 and 7.2.4), I performed the consistency check of pion misidentification probability using pions from reconstructed data and Monte Carlo $K^+ \to \pi^+\pi^+\pi^-$ events. The results are presented in Table 8.1.

Table 8.1: Misidentification probability of different e^+ PID requirements when applied to π^+ from the real and simulated $K^+ \to \pi^+\pi^+\pi^-$ events. Errors are determined by statistics only.

	$(2/2)PID$	$(2/3)PID$
Data	$(.124 \pm 0.013)\%$	$(0.3733 \pm 0.02)\%$
Monte Carlo without Cerenkov accidentals	$(< 10^{-3})\%$	$(0.204 \pm 0.012)\%$
Monte Carlo with Cerenkov accidentals	$(0.089 \pm 0.005)\%$	$(0.557 \pm 0.014)\%$

One can see that the misidentification probability of pion as positron was below 0.6%. The difference between the simulated and observed misidentification probability was used as a systematic uncertainty of the predicted contamination of the selected Ke3 sample due to the particle misidentification.

Contamination of the Kdal sample by the Ke3 decays was caused by e^+ from the Ke3 decay being inefficient in one (or very rarely both) of the Cerenkov counters. The frequency of such events was predicted well by the Monte Carlo simulation.

Note that since ideally the Ke3 sample was supposed to consist of Ke3 decays followed by $\pi^0 \to e^+e^-\gamma$, and the Kdal sample was supposed to consist of the mix of ($K^+ \to \pi^+\pi^0$,$K^+ \to \pi^+\pi^0\pi^0$, $K^+ \to \pi^0\mu^+\nu$) followed by $\pi^0 \to e^+e^-\gamma$, any other decay modes or decay chains were considered as contamination.

Table 8.2 contains Monte Carlo prediction for the contamination of the selected Ke3 sample by non-Ke3 kaon decay modes. Systematic errors connected with pion/muon misidentification as e^+ were not assigned to the individual contributions from the decay modes that were misidentified as Ke3 primarily due to the three reconstructed charged tracks being $e^+e^+e^-$. For the total contamination, the systematic errors were added linearly because of their correlation; if the misidentification probability is overestimated for pions from $K^+ \to \pi^+\pi^0$, it is also overestimated for pions from $K^+ \to \pi^+\pi^0\pi^0$ and for muons from $K^+ \to \pi^0\mu^+\nu$.

Table 8.2: Fraction of non-Ke3 kaon decay modes in the selected Ke3 sample as predicted by the Monte Carlo with added Cerenkov accidental hits. PDG [2] branching ratios were assumed. First error is statistical, second is systematic. Systematic errors are connected with uncertainty in the simulation of the Cerenkov response to pion/muon. Statistical errors were added in quadrature; systematic errors were added linearly.

Decay Chain	Mechanism for the decay misidentification as Ke3	Contamination with (2/2) e^+ PID	Contamination with (2/3) e^+ PID
$K^+ \to \pi^+\pi^0$; $\pi^0 \to e^+e^-\gamma$	π^+ identified as e^+	$(0.25 \pm 0.03 \pm 0.1)\%$	$(0.76 \pm 0.05 \pm 0.2)\%$
$K^+ \to \pi^0\mu^+\nu$; $\pi^0 \to e^+e^-\gamma$	μ^+ identified as e^+	$(0.10 \pm 0.01 \pm 0.04)\%$	$(0.11 \pm 0.01 \pm 0.03)\%$
$K^+ \to \pi^+\pi^0\pi^0$ with one $\pi^0 \to e^+e^-\gamma$	π^+ identified as e^+	$(0.13 \pm 0.02 \pm 0.05)\%$	$(0.32 \pm 0.03 \pm 0.09)\%$
$K^+ \to \pi^+\pi^0\pi^0$ with two $\pi^0 \to e^+e^-\gamma$	π^+ identified as e^+ or the three tracks are $e^+e^+e^-$	$(0.13 \pm 0.01)\%$	$(0.13 \pm 0.01)\%$
$K^+ \to \pi^+\pi^0$; $\pi^0 \to e^+e^-e^+e^-$	π^+ identified as e^+ or the three tracks are $e^+e^+e^-$	$(0.51 \pm 0.03)\%$	$(0.51 \pm 0.03)\%$
$K^+ \to \pi^0\mu^+\nu$; $\pi^0 \to e^+e^-e^+e^-$	μ^+ identified as e^+ or the three tracks are $e^+e^+e^-$	$(0.065 \pm 0.005)\%$	$(0.066 \pm 0.005)\%$
$K^+ \to \pi^+\pi^0\pi^0$; $\pi^0 \to e^+e^-e^+e^-$	π^+ identified as e^+ or the three tracks are $e^+e^+e^-$	$(0.036 \pm 0.004)\%$	$(0.043 \pm 0.004)\%$
$K^+ \to \pi^0e^+\nu$; $\pi^0 \to e^+e^-e^+e^-$	the three tracks are $e^+e^+e^-$	$(0.55 \pm 0.02)\%$	$(0.55 \pm 0.02)\%$
Total:		$(1.77 \pm 0.05 \pm 0.19)\%$	$(2.49 \pm 0.05 \pm 0.32)\%$

Table 8.3 shows the selected Kdal sample contamination predicted by the Monte Carlo. One can see that the largest contamination came from the Ke3 decay. As will be shown in Section 9.4.3, the systematic uncertainty in the e^+ from the Ke3 identificatation was 0.5% ((2/2) PID). Taking into account that the efficiency of this identification was 96%, the relative systematic uncertainty of the e^+ misidentification was $(0.5/4) = 12.5\%$. Table 8.3 reflects this uncertainty for the modes that were misidentified as Kdal due to misidentification of e^+ as π^+/μ^+.

Table 8.3: Fraction of non-Kdal kaon decay modes in the selected Kdal sample as predicted by the Monte Carlo with added Cerenkov accidental hits. PDG [2] branching ratios were assumed. First error is statistical, second is systematic. Systematic errors are connected with uncertainty in the simulation of the e^+ misidentification. For the total, statistical errors were added in quadrature.

Decay Chain	Mechanism for the decay misidentification as Kdal	Contaminatiion fraction
$K^+ \to \pi^0 e^+ \nu$; $\pi^0 \to e^+e^-\gamma$	e^+ identified as π^+/μ^+	$(0.49{\pm}0.01{\pm}0.06)\%$
$K^+ \to \pi^+\pi^0\pi^0$ with two $\pi^0 \to e^+e^-\gamma$	the three tracks are $\pi^+e^+e^-$	$(0.088 \pm 0.004)\%$
$K^+ \to \pi^+\pi^0$; $\pi^0 \to e^+e^-e^+e^-$	the three tracks are $\pi^+e^+e^-$	$(0.34 \pm 0.01)\%$
$K^+ \to \pi^0\mu^+\nu$; $\pi^0 \to e^+e^-e^+e^-$	the three tracks are $\mu^+e^+e^-$	$(0.052 \pm 0.002)\%$
$K^+ \to \pi^+\pi^0\pi^0$; $\pi^0 \to e^+e^-e^+e^-$	the three tracks are $\pi^+e^+e^-$	$(0.032 \pm 0.001)\%$
$K^+ \to \pi^0 e^+ \nu$; $\pi^0 \to e^+e^-e^+e^-$	e^+ identified as π^+/μ^+	$(< 0.01)\%$
Total:		$(1.00{\pm}0.02{\pm}0.06)\%$

8.3 Contamination by accidentals

Geometric acceptance of the detector for the three charged tracks from the kaon decays in question was of the order of 10%; therefore, for the most of the decays occurring in the decay vacuum tank, one or more tracks were not reconstructed in the spectrometer. For events where one of the three tracks was lost, there was a possibility that some track that was not related to the decay could be reconstructed to have a common vertex with the two remaining tracks. Such events were called 2+1 accidentals (two tracks from the real vertex of the kaon decay and one from somewhere else). The other possible combination: 1+1+1 events, where all three tracks came from different sources was much less probable. Since the correct timing was required in the Cerenkov counters for the low mass e^+e^- pair (both in the trigger and in the selection criteria), the most probable configuration for 2+1 accidental events was the low mass e^+e^- pair from some kaon decay containing π^0 in the final state and a positive track coming from somewhere else (another kaon decay or beam interaction) that was reconstructed to have a common vertex with the e^+e^- pair.

In order to estimate the contribution of 2+1 accidentals to the selected Ke3 and Kdal samples, I simulated all the pertinent kaon decays without the requirement for all three daughter tracks to cross the aperture of the A counter: condition used to increase the speed of the Monte Carlo production (Section 6.4). The accidental hits obtained from the reconstructed real data $K^+ \to \pi^+\pi^+\pi^-$ decays (Section 6.7) were added to these simulated decays. The result is that 2+1 accidentals contributed at the level of $(0.25 \pm 0.07)\%$ and $(0.12 \pm 0.05)\%$ to the selected Kdal and Ke3 samples respectively.

8.4 Contamination by upstream decays

The decays occurring usptream of the decay volume might contaminate the selected samples if the decay vertex was misreconstructed to be inside of the decay volume. Such events, as they were not simulated by the Monte Carlo, would result in an excess of data events (compared to Monte Carlo) with bad vertex quality and with the small (upstream) Z coordinate of the found vertex. Vertex quality and Z vertex coordinate distributions are discussed in detail in Sections 9.2.1 and 9.3.1. Vertex quality distributions were shown to agree well between data and Monte Carlo and the quantified disagreement (0.6%) was included in the systematic uncertainty of the final result. The Z coordinate distribution did show an excess of data with vertices close to the upstream end of the decay volume; however, this discrepancy disappeared already at about -400cm, while the selection criteria required $Zvtx > -350cm$. This requirement "removed" the accepted vertices by 140cm from the upstream end of the decay volume.

The other possible way in which the decays occurring usptream could have contaminated the selected sample was for the π^0 to decay into $\gamma\gamma$ with one of the photons converting into an e^+e^- pair on the material of the usptream decay volume vacuum window and for the charged track from the initial decay to be transported by the beam optics into the decay volume in such a way that it would traverse the trajectory of the e^+e^- pair and have the reconstructed three track vertex inside the decay volume. Such events would be characterized by bad vertex quality, and as discussed in Section 9.2.1, the tail of the vertex quality distribution agreed well between data and Monte Carlo.

Both of the mechanisms of contamination described above would be greatly reduced by the requirement of the fully reconstructed π^0 and as shown in Section 9.6, the final result does not differ significantly for the Ke3 and Kdal samples where the π^0 was and was not reconstructed.

Based on the above arguments, I did not take into account the contamination by upstream decays and considered the systematic error connected with the data-Monte Carlo discrepancy in the vertex quality distribution to account for such omission.

8.5 Photon conversion in the material of the detector

The first place where the photon conversion into an e^+e^- pair could happen was the downstream decay volume vacuum window (conversion on the usptream one is discussed in the previous section). The downstream vacuum window is located downstream from the D5 dipole magnet; therefore, if such an e^+e^- pair was reconstructed in the spectrometer, the backtracking through the D5 magnetic field would give completely wrong coordinates and momenta of both e^+ and e^- in the decay volume. Therefore the vertex would not be found.

8.6 Summary

My study of the contamination of the selected signal (Ke3) and normalizer (Kdal) samples showed that contamination of the Ke3 sample by other (non-Ke3) decay modes was at the level of 1-2% (depending on the cuts) and could be predicted with not worse than 0.3% (of the selected sample) accuracy (Table 8.2). Figure 8.1 shows comparison of data and Monte Carlo distributions of the energy deposited in the calorimeter by the second e^+ (not the one from the π^0 decay) from the selected Ke3 sample (2/2 e^+ PID). Minimum ionization energy loss in the calorimeter was about 250MeV; therefore such energy deposition was the signature of muons and pions. The little spike at 250MeV that one can see in Figure 8.1 was caused by pions and muons misidentified as e^+; the Monte Carlo describes this spike with about 30% accuracy that does not contradict the uncertainty estimates from Table 8.2.

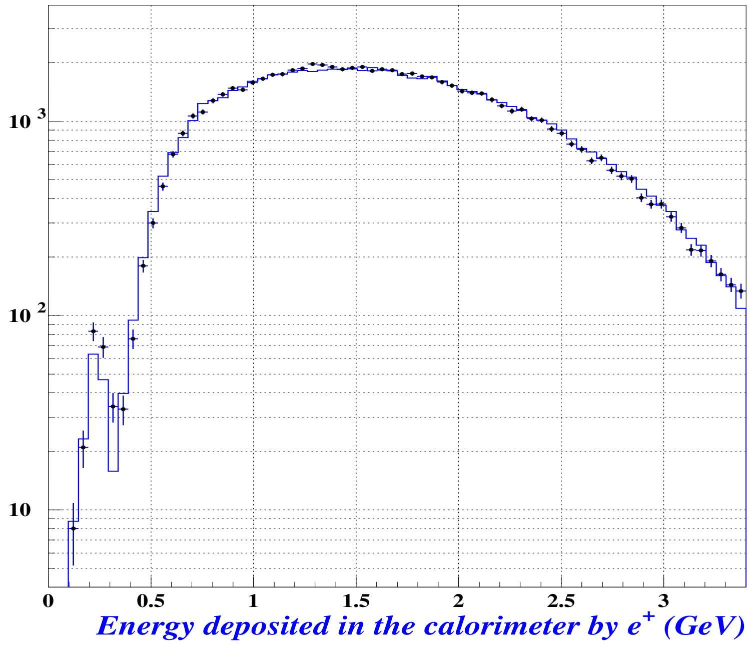

Figure 8.1: Energy deposited in the calorimeter by the second positive track from the selected Ke3 sample (e^+ which is not from the low mass e^+e^- pair). Markers with errors represent data; histogram represents Monte Carlo.

Contamination of the selected Kdal sample was found to be $(1.00 \pm 0.02_{stat} \pm 0.06_{sys})\%$ (Table 8.3).

Contamination by 2+1 accidentals was found to be at the level of $(0.12 \pm 0.05)\%$ for the Ke3 and $(0.25 \pm 0.07)\%$ for the Kdal samples.

Contamination by the decays occurring uspstream of the decay volume was assumed negligible and the systematic error connected with this assumption was incorporated in the error connected with the data-Monte Carlo level of agreement of the vertex quality distribution. The validity of this assamption will be checked by observing the change in the result when the full reconstruction of the π^0 was required (Section 9.6).

CHAPTER 9
ANALYSIS OF THE SYSTEMATIC UNCERTAINTY

9.1 Overview

The statistical accuracy of the measured Ke3 relative branching ratio was defined by the size of the selected Ke3 sample (around 70k without π^0 reconstruction) and is equal to 0.4%.

The systematic error was determined by the study of the stability of the result under variation of event reconstruction procedure, selection criteria, detector efficiencies applied to the Monte Carlo and subdivision of the selected samples (both signal and normalizer).

In practice, the simulated events were weighted to create a "correct" mix according to the branching ratios from the PDG [2]. After that, two ratios (called single-ratios) of the numbers of events selected from the data and Monte Carlo were calculated (Equation 9.1).

$$R_{Ke3} = \frac{N^{MC}_{Ke3}}{N^{Data}_{Ke3}}; \qquad R_{Kdal} = \frac{N^{MC}_{Kdal}}{N^{Data}_{Kdal}} \tag{9.1}$$

If there were no cross-contamination of the selected Kdal and Ke3 samples, the double-ratio R_{Kdal}/R_{Ke3} would have given us exactly the number we were trying to measure $(\frac{BR(K^+ \to \pi^0 e^+ \nu)}{Kdal})$ relative to the prediction for this number based on the branching ratios claimed by the PDG. Existing cross-contamination was found to be small and in addition, affected the result as a second order correction (providing that the deviation of the E865 Ke3 result from the current PDG estimate was small). Taking this into account, in order to study systematic effects the two ratios from Equation 9.1 were arbitrarily normalized to be equal to unity when the standard reconstruction procedure and selection criteria were applied to both data and Monte Carlo and when the standard efficiencies were applied to the Monte Carlo. If there were no systematic uncertainties I would have expected the both single-ratios and the double ratio to remain equal to unity within the statistical uncertainties under any reasonable change in the way events were selected, reconstructed or simulated; thus, any significant variation of the double-ratio gave me an estimate of the systematic uncertainty connected with the aspect of the selection criteria, reconstruction or simulation that caused this variation.

In some cases, the variation in the single-ratios was larger than in the double-ratio; this reflected the cancellation of the systematic uncertainties - the effect we were aiming at when choosing the normalizer for this measurement to be as similar as possible to the signal.

Note that since in most cases the event samples (both data and Monte Carlo) used to obtain single and double ratios had a very large overlap. As a matter of fact, in most cases, only a small (order of 1-10%) fraction of events was removed/added by the variation in the selection criteria, efficiencies or reconstruction. Therefore, the compared single and double ratio were not statistically independent; the error of a single ratio for the purpose of comparison was calculated according to Equation 9.2.

$$\begin{aligned}
\epsilon^{MC} &= N_1^{MC}/N_2^{MC} \\
\epsilon^{Data} &= N_1^{Data}/N_2^{Data} \\
R &= (N_1^{MC}N_2^{Data})/(N_1^{Data}(N_2^{MC}) \\
\frac{\sigma_R}{R} &= \sqrt{\epsilon^{MC}(1-\epsilon^{MC})/N_2^{MC} + \epsilon^{Data}(1-\epsilon^{Data})/N_2^{Data}}
\end{aligned} \tag{9.2}$$

where N_1^{MC}, N_2^{MC}, N_1^{Data}, and N_2^{Data} are the number of Monte Carlo and data events obtained with for instance two different sets of Cerenkov efficiencies. The indexes were always chosen in such a way as to have both ϵ^{MC} and ϵ^{Data} below one. In each of the tables that follow, the single ratios obtained under standard conditions (the ones normalized to unity) are shown with the simple statistical error, while the errors of all the other single ratios have errors calculated according to Equation 9.2. In most cases the errors were less than 0.1%. I listed them for the first table in this Chapter (Table 9.1), but omitted in the following tables, unless the errors exceeded 0.1% value.

In some cases (like exclusive partitioning of the data), two completely independent samples were compared. In such cases, the errors were calculated based solely on the data and Monte Carlo statistics of these samples.

9.2 Event reconstruction

Monte Carlo simulation of the E865 experiment was not ideal: accidental hits in the apparatus, kaon beam phase space and the interactions of daughter particles were simulated with a finite precision limited by the accuracy of our knowledge of things like beam transport, magnetic field map, amount and location of detector material, etc., and by the extent to which Monte Carlo can simulate the real physical processes of electromagnetic and hadronic interactions.

One of the ways in which I studied the effect of these inaccuracies on the systematic uncertainty of the final answer was by varying the event reconstruction procedure. First, I used two alternative methods of the common vertex reconstruction and second, I reconstructed real data events with a varied magnetic field of the detector spectrometer.

9.2.1 Vertex finding procedure

The standard vertex finding procedure consisted of finding a point inside the vacuum decay volume that was simultaneously closest to the three tracks reconstructed in the spectrometer and backtracked to the decay volume through the first detector's dipole (D5) magnetic field. This procedure minimized the sum of the squares of the the distances of the three tracks to the vertex point. The quality of the found vertex was represented by the square root of this sum (called S). This procedure did not take into account the errors of the reconstructed tracks' positions; as a result, the average value of S increased for the vertices found far upstream. The average dependence of S on the Z position of the vertex was obtained empirically (from the data) and was used to remove such dependence. The corrected S called Snorm was used to make a vertex quality cut.

The alternative method of the constrained vertex fit was developed by the Pittsburgh group and used the track error matrix obtained from the tracks' fit in the spectrometer and propagated back through the magnetic field of D5. Uncertainties of the field map used were included in the error matrix. The constrained fit allowed correct treatment of correlated uncertainties of the reconstructed tracks' positions and provided the true χ^2 of the constrained fit as the vertex quality indicator.

The importance of the vertex finding procedure was that any inaccuracy of the magnetic field map of the detector's two dipoles as well as any inaccuracy in the modeling of the daughter track's interactions in the detector would cause a systematic bias between data and Monte Carlo both in the probability of finding and in the quality of the found vertex. As the selection criteria always required a good quality three track vertex to be found, such a bias would translate into a systematic uncertainty of the final result. Since this bias would be different for the two described methods of vertex reconstruction, the difference in the double-ratios obtained with these two alternative methods was used as an estimate of the systematic effect on the vertex finding due to the inaccuracy of the magnetic field map and of the particle interactions modeling; the two alternative methods also served as a way to assess the robustness of the event reconstruction procedure.

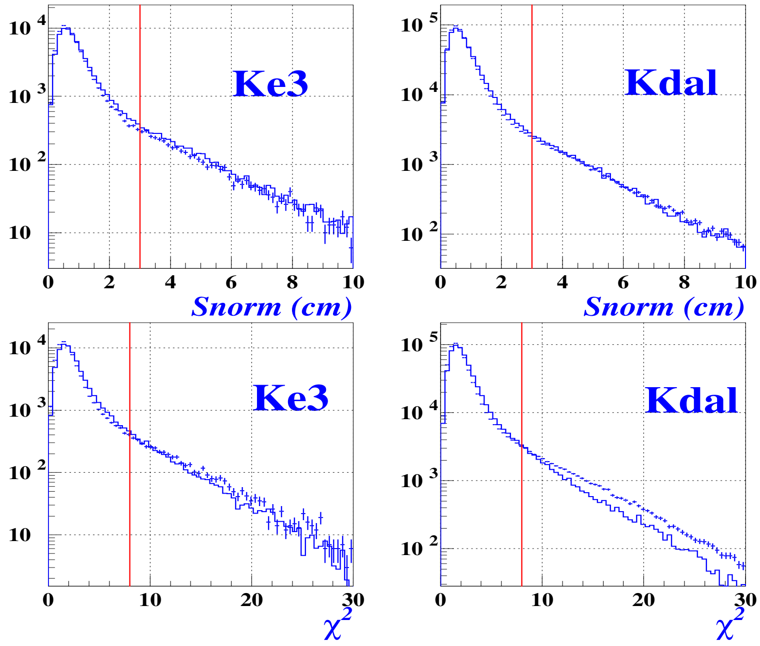

Figure 9.1: Comparison of data and Monte Carlo distributions of the found three track vertex quality for events reconstructed with the standard vertex finding procedure (upper plots) and with the constrained vertex fit (lower plots). Lines on all four plots show the values of the chosen cuts ($Snorm < 3$ and $\chi^2 < 8$). Markers with errors represent data; histogram represents Monte Carlo.

I reconstructed both data and Monte Carlo with the two alternative vertex finding methods. Comparison of the resulting data and Monte Carlo Snorm and χ^2 distributions is shown in Figure 9.1. One can see that while all of the distributions show similar small disagreements for the "good" (small Snorm or χ^2) vertices, the agreement of the high end of the distributions is much better for the events reconstructed with the standard vertex finding procedure. The disagreement at the lower end of the distributions is connected with the inaccuracy of the detector material modeling and the vertex quality cuts were chosen to be at the point where this distortion is minimal. Agreement at the high end of the distributions is critical, as events with a bad vertex are the ones that can be discarded and an event can be lost. 2+1 accidentals also would show up at the higher end of the vertex quality distribution. The larger disagreement for the events reconstructed with the vertex constrained fit procedure might be connected with several assumptions about the value of multiple scattering and inaccuracy of the magnetic field map that were used in this procedure.

In order to estimate the systematic effect connected with the inaccuracies in the magnetic field and in the particle interactions modeling, as well as in the simulation of the accidentals, I compared the single and double ratios obtained with the different vertex finding procedures and with the different vertex quality cuts. The results of this comparison are presented in the Table 9.1. For the events reconstructed with the standard method, I used $Snorm < 3$ cut and for the events reconstructed with the constrained vertex fit, I used $\chi^2 < 8$ cut. For both methods cuts were chosen to remove about 5% of events.

Table 9.1: Dependence of the single and double ratios on the vertex fitting procedure used for event reconstruction and on the applied vertex quality cut. Ke3 and Kdal single ratios were normalized to be equal to unity when the standard vertex finding procedure with $Snorm < 3$ requirement were used.

	$(MC/Dat)_{Ke3}$	$(MC/Dat)_{Kdal}$	Kdal/Ke3
Standard vertex $Snorm < 3$	1.000(0.005)	1.000(0.002)	1.000(0.005)
Constrained fit vertex $\chi^2 < 8$	0.9959(0.0002)	0.9972(0.0001)	1.0013(0.0002)
Standard vertex $Snorm < 10$	1.0090(0.0009)	1.0027(0.0005)	0.994(0.001)
Constrained fit vertex $\chi^2 < 30$	0.9899(0.0009)	0.9820(0.0005)	0.992(0.001)

From Table 9.1 one can see that the two vertex reconstruction procedures provided the results (double ratios) that differed from each other only by (0.1-0.2)% and behaved similarly when the vertex quality requirements were changed. Taking this and the fact that the constrained vertex fit procedure resulted in the larger disagreement between data and Monte Carlo in the vertex quality distribution, I decided to use the standard vertex finding procedure for this analysis.

I assigned the variation of 0.6% in the double ratio, observed when the $Snorm$ cut value was changed from 3 to 10 to be a systematic uncertainty of the final result caused by the inaccuracies in the magnetic field and interactions modeling. It is important to note that this uncertainty incorporates the error caused by the assumption that the contamination of the selected samples by the upstream decays was negligble, as these decays would have bad vertex quality and add to the discrepancy between data and Monte Carlo.

This 0.6% uncertainty is explicitly connected with the vertex quality cut; therefore, I will not consider the $Snorm$ cut in the next section (dedicated to the systematic errors connected with the other selection criteria).

9.2.2 Magnetic field variation

In order to check the stability of the result under the reasonable variation of the spectrometer magnetic field map, I performed two checks. First, I reconstructed the data using the best estimate of the overall D6 spectrometer dipole magnetic field available from the field strength measurement and compared the result with the one obtained with the D6 scale adjusted by -0.25% (correction obtained from comparison of the data and Monte Carlo distributions). The resulting variations of the single and double ratios are shown in Table 9.2.

Table 9.2: Dependence of the single and double ratios on the D6 magnetic field scale factor. The scale factor is relative to the best known field scale obtained from the field strength measurement; the -0.25% correction was obtained from maximizing agreement between the low mass e^+e^- pair distribution from the data with that from the Monte Carlo. Ke3 and Kdal single ratios were normalized to be equal to unity when the correction was used. Statistical errors (numbers in parenthesis) of less than 0.1% are not listed.

	$(MC/Dat)_{Ke3}$	$(MC/Dat)_{Kdal}$	Kdal/Ke3
D6 B-field scale corrected by -0.25%	1.000(0.005)	1.000(0.002)	1.000(0.005)
Uncorrected D6 B-field scale	0.996	0.997	1.001

The magnetic field consistency study performed by the Pittsburgh group showed that the largest field inconsistencies were limited to the D6 regions with $|Y| > 40cm$, where the field became nonlinear. Table 9.3 shows the variation of the single and double ratios when all three tracks were required to be within $\pm 40cm$ in Y at the mid-plane of the D6 dipole.

Table 9.3: Variation of the single and double ratios when all three tracks were required to be within $\pm 40cm$ in Y at the mid-plane of the D6 dipole. Ke3 and Kdal single ratios were normalized to be equal to unity when no Y cut at D6 was applied. Statistical errors of less than 0.1% are not listed.

	$(MC/Dat)_{Ke3}$	$(MC/Dat)_{Kdal}$	Kdal/Ke3
No Y cut at D6	1.000(0.005)	1.000(0.002)	1.000(0.005)
$\lvert Y_{D6}\rvert < 40cm$	0.995(0.001)	0.998(0.001)	1.003(0.001)

It is important to note that the $|Y_{D6}| < 40cm$ cut removed about 36% of the Kdal and 30% of the Ke3 events. Therefore the resulting 0.3% variation in the double-ratio was caused not only by the inaccuracies in the non-linear regions of the magnetic field but by the any other systematic effects that could affect the spatial distributions of the tracks as well (for instance inaccuracies in the PWC and Cerenkov efficiencies). Nevertheless, I conservatively ascribed all of this 0.3% to the inaccuracies in the magnetic field.

9.3 Selection criteria

9.3.1 Zvtx cut

The Z position of the vertex was required to be further downstream (larger) than -350cm. Data and Monte Carlo vertex Z positions distributions agreed well for both Ke3 and Kdal samples (Figure 9.2). The excess of the data at the lower end of the distributions was caused by the misreconstructed decays occurring upstream from -490cm where Monte Carlo kaons “started”. It is important to note the good agreement of the Zvtx distributions in the region above 0cm, as events from this region had vertices inside the magnetic field of the D5 dipole; therefore they were sensitive not only to the total field integral but also to the details of the magnetic field map inside the magnet and any inaccuracy in the field was critical since the acceptance dropped dramatically in this region of Z of the vertex.

In order to estimate the systematic effect of this requirement, I varied the cut point by ± 50cm. The results are presented in Table 9.4

Table 9.4: Dependence of the single and double ratios on the value of the Z position of the vertex cut. Ke3 and Kdal single ratios were normalized to be equal to unity when the standard ($Zvtx > -350cm$) requirement was applied. Statistical errors of less than 0.1% are not listed.

	$(MC/Dat)_{Ke3}$	$(MC/Dat)_{Kdal}$	Kdal/Ke3
$Zvtx > -350cm$	1.000(0.005)	1.000(0.002)	1.000(0.005)
$Zvtx > -400cm$	1.002	1.001	0.999
$Zvtx > -300cm$	0.998	0.999	1.001

I estimated the systematic uncertainty connected with the Zvtx cut to be 0.1%.

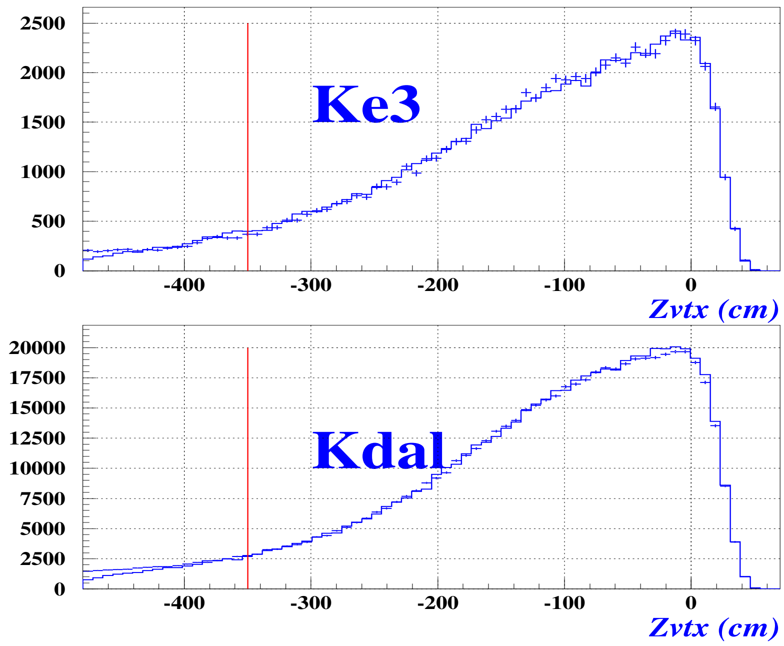

Figure 9.2: Z (along the beam-line) position of the vertex distributions. Vertical lines show standard cut-off points: $Zvtx > -350cm$. Histogram represents Monte Carlo, while points with errors represent data.

9.3.2 Cerenkov Ambiguity cut

Overview

Cerenkov counters were used to separate electrons (positrons) from pions and muons. The finite granularity of the Cerenkov counters (four and twelve photomultipliers per one side of the first and second Cerenkov counter respectively), made the particle identification ambiguous when more than one track traversed the area of the Cerenkov counter viewed by a given photomultiplier.

As described in Section 7.2.2, I decided to reject events that had two or more tracks which geometrically could produce a response in the same photomultiplier (Cerenkov Ambiguity Cut or CAC). CAC reduced the combined sample of all Dalitz events (Ke3+Kπ2+Kμ3+Kπ3) by almost 30%; therefore, even a small relative difference between the efficiency of this cut for data versus Monte Carlo could have led to a substantial error in the measured Ke3 branching ratio.

To assess the systematic effects of CAC the following three items were studied: sharing of the Cerenkov light between adjacent mirror assemblies, Monte Carlo simulation accuracy of the pion response in the shower calorimeter, and the accuracy of the final particles' kinematics simulation. All three items, as well as their relevance to the investigation of CAC systematic effects are described below.

Sharing of the Cerenkov light between adjacent mirror assemblies

When the electron (positron) traversed one of the E865 Cerenkov counters, the first Cerenkov photons were created about 2m away from the primary mirrors. Thus, at the mirror plane, the Cerenkov light cone created an image of about 5cm in radius. The consequence was that if the track traversed the mirror plane within roughly $\pm$5cm from the border between two adjacent mirror assemblies, the light produced by this track was divided between two mirrors and reflected into two different photomultipliers.

Let us consider why this mechanism was important for understanding CAC. The obvious configuration for the two tracks to be ambiguous in the Cerenkov counter was if geometrically they traverse exactly the same mirror assembly. This configuration was determined solely by the particle kinematics. The second configuration was described by one of the particles intersecting with the mirror plane close to the border between two mirrors (within roughly 5cm) and the second going through the adjacent mirror assembly. In this case, the first particle could produce a signal in photomultipliers associated with both mirror assemblies and thus create an ambiguous situation. In order to check how the single and double ratios varied with the application of CAC it was necessary to simulate the light sharing correctly. The fraction of the Cerenkov light reflected from the adjacent mirror assembly depended on the distance of the track to the assembly's border. This dependence was not previously simulated by Monte Carlo.

I modified the simulation procedure as described in Section 6.5.2. In the result, a pion/muon misidentification probability due to the sharing was described well by the Monte Carlo (Figure 6.4). The remaining discrepancies in Figure 6.4 were adequate to test CAC systematic effects with the the accuracy of better than 0.5%.

Monte Carlo simulation accuracy of the pion response in the shower calorimeter

In addition to the light in the Cerenkov counters, the energy deposited by the charged track in the shower calorimeter could be used for the separation of electrons (positrons) from pions and muons. While an electron (positron) deposited all of its energy in the calorimeter, pions and muons mostly suffered only minimum ionization losses (about 250MeV for the E865 calorimeter). Thus, the ratio of the deposited energy to the track's momentum (E/P) could be used for the particle identification.

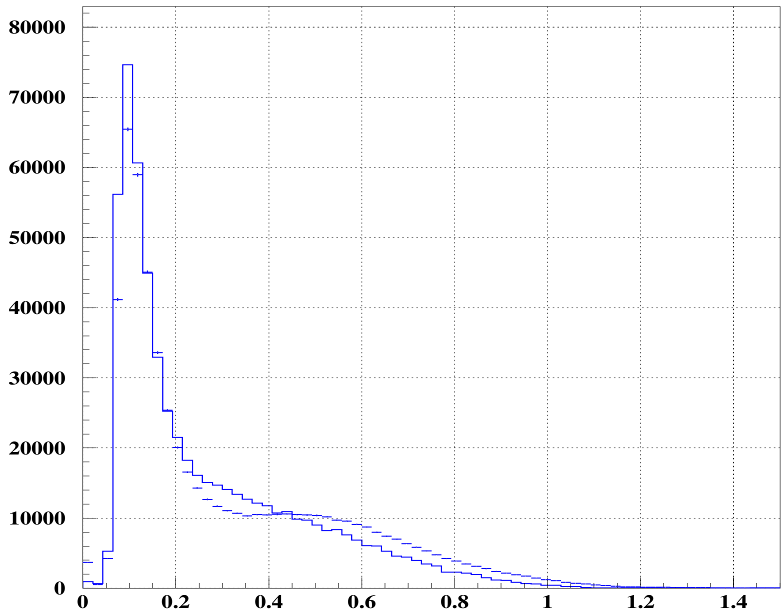

Figure 9.3: The figure shows the Ratio of the energy deposited in the calorimeter to the momentum (E/P) of $\pi+/\mu+$ tracks from the selected Kdal (non-Ke3) events. Pointers represent data, while the histogram represents Monte Carlo.

For the Ke3 analysis the Cerenkov counters alone provided an adequate electron (positron) separation, and the calorimeter information was not used for particle identification. The situation changed dramatically if CAC was removed. For the events which were ambiguous in the Cerenkov counters, the contamination of the selected Ke3 sample by the other Dalitz modes rose to about 50%. Thus, the use of the calorimeter became necessary if tracks were allowed to be in the ambiguous regions of the Cerenkov counters.

Unfortunately, the E865 simulation of the pion nuclear interactions in the calorimeter did not produce a response consistent with the data (Figure 9.3). One can see from Figure 9.3 that in the range of E/P larger than 0.8 (the standard requirement for the electron) the Monte Carlo underestimated the amount of data by about a factor of two. This factor was found to be momentum dependent.

One way to take into account this discrepancy was to create the momentum dependent correction factor $C = Fdat/Fmc$, where Fdat=fraction of the data pions with E/P>0.8 and Fmc=fraction of the Monte Carlo pions with E/P>0.8 The π^+ tracks from $K^+ \rightarrow \pi^+\pi^+\pi^-$ decays were used to obtain this correction factor (Figure

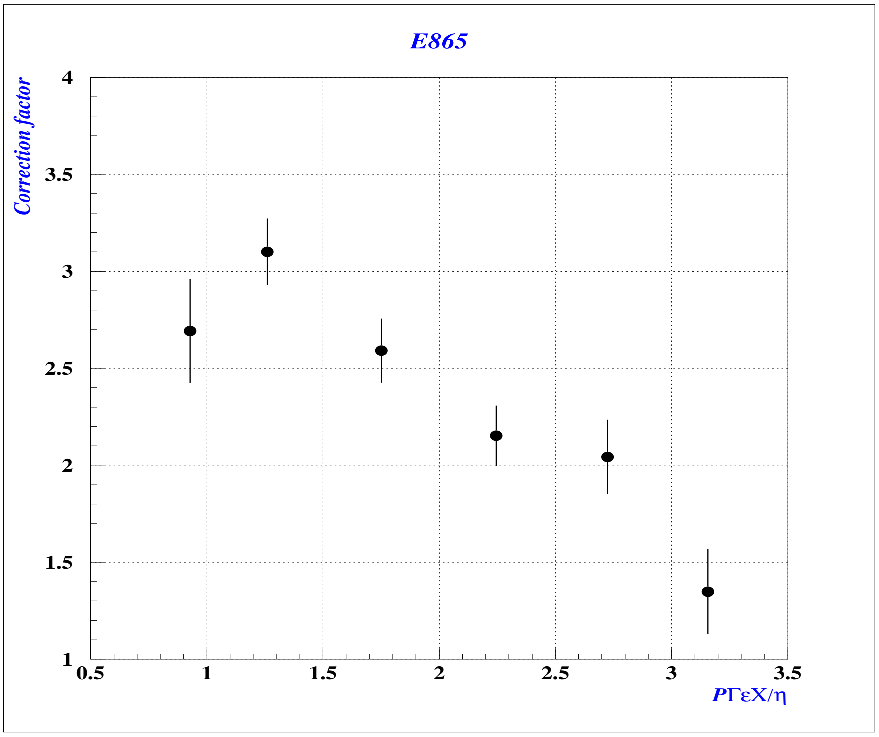

Figure 9.4: The figure shows the Correction factor (C=Fdat/Fmc; Fdat=fraction of the data $K^+ \to \pi^+\pi^+\pi^-$ decays with π^+ E/P>0.8; Fmc=fraction of the Monte Carlo $K^+ \to \pi^+\pi^+\pi^-$ decays with π^+ E/P>0.8) as a function of pions momentum in GeV/c.

9.4).

In order to check how well the correction factor described the discrepancy, I applied the E/P>0.8 cut to the Kdal (non-Ke3) sample preselected with the Cerenkov counters. The momentum dependent correction factor was applied to the selected Monte Carlo events. In the result, the single ratio for the selected events was 16% different from the single ratio without E/P cut. Taking into account that the selected Ke3 events which were ambiguous in the Cerenkov counters had about 10% contamination by the other Dalitz modes even after requirement of E/P>0.8, I estimated the systematic error in the single ratio for these events due to the error in the E/P distribution to be 1.6%.

Accuracy of the final particle simulation

The term "final particle simulation" here is used to describe not just the simulation of the kinematics of the particular kaon decay, but also the simulation of the detector response with all inefficiencies taken into account, as well as all possible background sources. In other words, everything that affected the spatial distributions of the finally selected events.

CAC used the X and Y positions of the charged tracks at the Cerenkov mirror planes to decide if they could be ambiguous in the Cerenkov counters. Thus, if the kinematics of the final particles were not simulated correctly in the Monte Carlo, application of this cut could lead to a systematic error. In order to check this effect, I selected the sample of events that included all of the kaon decay modes with π^0 in the final state (i.e. no separation was done between Ke3 and Kdal events). The selection used particle identification only for the low mass e^+e^- pair. No PID was required from the second positive track. The variation of the ratio between selected Monte Carlo and data events with the application of CAC is shown in the Table 9.5.

Table 9.5: Dependence of the single ratio on the Cerenkov ambiguity cut. Selected events are all decays, where low mass e+e- pair was found and no PID was made for the second positive track. The single ratio for events with no Cerenkov ambiguity cut was normalized to be one.

	without CAC	with CAC
MC/Data ratio (Kdal+Ke3)	1.000(0.002)	1.003(0.002)

Summary

Table 9.6 shows the variation of the single and double ratios when CAC is removed.

Table 9.6: Variation of the single and double ratios when CAC is removed. (3/3) e^+ identification (two Cerenkov and calorimeter identifications required) was used for the positron from the Ke3 decay. The Ke3 single ratio was corrected to remove the error caused by inaccuracy in the pion responce in the calorimeter simulation. The error of this single ratio includes the error caused by the correction. All single ratios were normalized to be one when CAC was applied

	$(MC/Dat)_{Ke3}$	$(MC/Dat)_{Kdal}$	Kdal/Ke3
CAC is in place	1.000(0.005)	1.000(0.002)	1.000(0.005)
No CAC applied	1.011(0.011)	0.997(0.002)	0.986(0.012)

One can see that the result changed by $(1.4 \pm 1.2)\%$ when CAC was removed. While this variation was substantial, it depended heavily on the empirical correction caused by the necessary calorimeter inclusion in the particle identification. The CAC was introduced exactly to eliminate the need for such a correction. Therefore I decided to use CAC and assumed that the only error caused by CAC is the one connected with the inaccuracy of the final particle simulation and is equal to 0.3% (from Table 9.5).

9.3.3 M_{ee} cut

Invariant mass of the e^+e^- pair (M_{ee}) that originated from the $\pi^0 \to e^+e^-\gamma$ decay, due to its sharpness, was a good indicator of how well the detector was modeled. The invariant mass was peaked at low values due to the e^+e^- pair coming from the internal photon conversion. The comparison of data and Monte Carlo distributions of M_{ee} is shown in Figure 9.5.

Table 9.7: Variation of the single and double ratios when the $M_{ee} < 0.05GeV$ cut is removed. Ke3 and Kdal single ratios were normalized to be equal to unity when the standard ($M_{ee} < 0.05GeV$) requirement was applied. Statistical errors of less than 0.1% are not listed.

	$(MC/Dat)_{Ke3}$	$(MC/Dat)_{Kdal}$	Kdal/Ke3
$M_{ee} < 0.05GeV$	1.000(0.005)	1.000(0.002)	1.000(0.005)
No M_{ee} cut	0.997(0.001)	0.999	1.002(0.001)

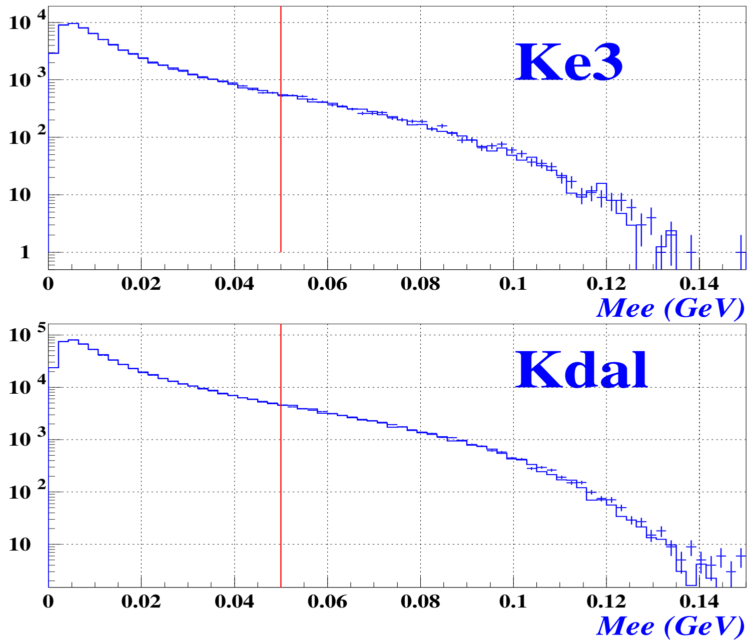

Figure 9.5: Invariant mass of the e^+e^- pair from the $\pi^0 \to e^+e^-\gamma$ decay. Vertical lines show standard cut-off points: $M_{ee} < 0.05GeV$. Histogram represents Monte Carlo, while points with errors represent data.

One can see that the distributions agree well for both Ke3 and Kdal samples. This agreement strengthened my conclusion that the inaccuracies in the magnetic field map and in the particles' interactions inside the detector modeling did not translate into a large systematic error. It also showed that the influence of the accidental hits in the PWCs on the track momentum and vertex reconstruction was modeled well (good agreement of the high M_{ee} tail).

Conservatively, I applied the $M_{ee} < 0.05 GeV$ cut in order to eliminate the π^0 decay into four electrons and to make sure that the contribution of any other possible backgrounds or badly misreconstructed events was minimized.

Table 9.7 shows the variation of the single and double ratios when the $M_{ee} < 0.05 GeV$ cut was removed.

I assigned 0.2% systematic error to the M_{ee} cut.

9.3.4 Aperture cuts

Systematic uncertainties connected with the detector aperture cuts will be discussed in Section 9.5.

9.3.5 Particle Identification cuts

Pion/Muon identification

Accuracy of pion/muon identification with the .not.(2/2) PID based solely on the Cerenkov counters was discussed in Section 7.2.4. It was shown there that the use of .not.(2/2) PID resulted in only $(0.04 \pm 0.01)\%$ (Table 7.1) discrepancy between data and Monte Carlo. I used this number as an estimate of the systematic error connected with pion/muon particle identification.

Electron/Positron identification

Accuracy of the e^+/e^- identification was directly connected to the accuracy of the Cerenkov counters' efficiency measurement and modeling; it will be discussed in Section 10.4.3.

9.4 Detector efficiencies

9.4.1 Proportional Wire Chambers

The PWC efficiency obtained from the data was organized into two alternate efficiency maps.

The first map included efficiencies for clusters of 10 wires for all sixteen sensitive planes (four per each wire chamber).

The construction of the P3 and P4 wire chambers included garlands kept at a constant potential to support the wires. This potential resulted in narrow inefficiency regions located perpendicular to the direction of the wires. Such inefficiencies were averaged out when the efficiency was measured by wire number. To check the magnitude of the error induced by such averaging, I constructed a second PWC efficiency map that depended not on the wire number but on the X and Y coordinates of the hit.

Both efficiency maps were constructed separately for pions/muons and electrons. The dependence of the single and double ratios on the choice of the PWC efficiency map applied to the Monte Carlo simulation is shown in the Table 9.8.

Table 9.8: Dependence of the single and double ratios on the choice of the PWC efficiency map applied to the Monte Carlo simulation. All single ratios are normalized to be one when the wire dependent efficiency map is applied. Statistical errors of less than 0.1% are not listed.

	$(MC/Dat)_{Ke3}$	$(MC/Dat)_{Kdal}$	Kdal/Ke3
Wire dependent map	1.000(0.005)	1.000(0.002)	1.000(0.005)
$(X;Y)$ dependent map	0.997	0.995	0.998
100% efficient PWCs	1.011	1.016	1.005

I estimated that the systematic error caused by the PWC inefficiencies to be 0.2%. Note that even in case of 100% efficient chambers in the Monte Carlo simulation, the double ratio changed by only 0.5%.

9.4.2 D counters

As described in Section 5.5.2, the D counter efficiencies were determined from CERENK trigger events, as this trigger did not require hits in the D counters. The efficiencies were measured as a function of the X coordinate separately for each D counter slab.

Table 9.9 shows the single and double ratios for two different choices of the D counter efficiency map.

Table 9.9: Dependence of the single and double ratios on the choice of the D counter efficiency map applied to the Monte Carlo sample. All single ratios are normalized to be one when the measured efficiency map is applied. Statistical errors of less than 0.1% are not listed.

	$(MC/Dat)_{Ke3}$	$(MC/Dat)_{Kdal}$	Kdal/Ke3
Measured efficiency map	1.000(0.005)	1.000(0.002)	1.000(0.005)
100% efficient D counters	1.031	1.026	0.995

The observed 0.5% variation of the double ratio should be multiplied by the relative uncertainty of the measured D counter inefficiencies. As one can see from Figure 5.5, the inefficiencies of the D counters with low efficiencies were measured with at least about 40% relative accuracy (D counter slab #12; 10cm-30cm bin). Conservativelly, I assumed that the systematic error of the final result connected with the uncertainties in the D counter efficiencies was $0.5\% \times 0.4 = 0.2\%$.

9.4.3 Cerenkov counters

Details of the Cerenkov efficiency measurement are presented in Section 5.3.3. In order to understand how the uncertainty of the measured efficiencies affected the accuracy of the final result, it is important to note that Cerenkov counters were used for two puproses: to identify the low mass e^+e^- pair and to identify the e^+ from the Ke3 decay.

The low mass pair identification was common for the signal and the normalizer (Ke3 and Kdal respectively). As the spatial distributions of the pair from Ke3 and Kdal decays were very similar, any systematic bias in the efficiency of the e^+e^- identification would be the same for the Ke3 and Kdal samples and would cancel in the double ratio.

The e^+ from the Ke3 identification, on the other hand, was required only for the Ke3 sample and any systematic error in it would translate directly into the error of the final result.

The two alternative e^+ identification methods: (2/2) and (2/3) PID are described in Section 7.2.4. The (2/2) e^+ PID required in-time signals in both Cerenkov counters, while for the (2/3) e^+ PID the $E_{e^+}/P_{e^+} > 0.8$ cut was allowed to verify the positron PID in case of the hit in only one of the two Cerenkov counters.

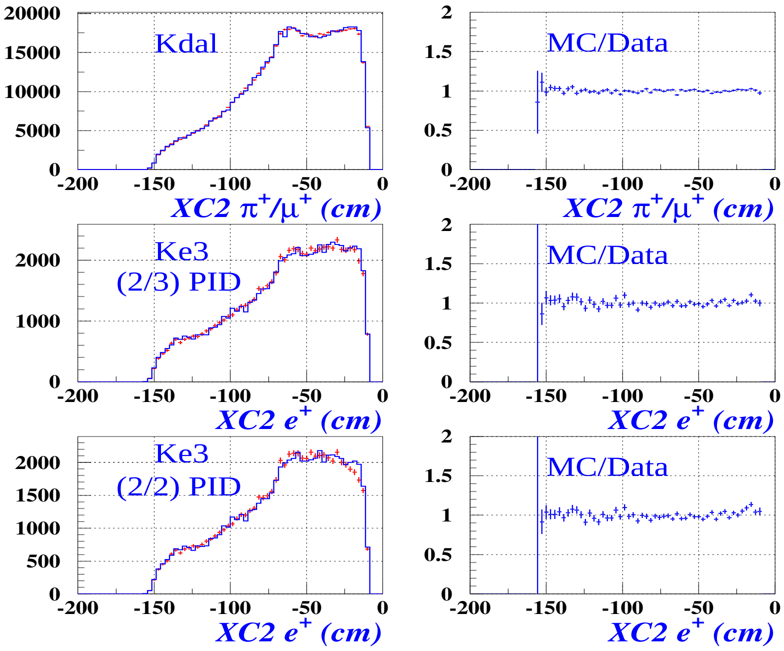

Figure 9.6: X (horisontal) position of the third (second positive: not e^+ from the low mass pair) track at the mirror plane of the C2. Histogram represents Monte Carlo, while points with errors represent data.

When the (2/2) PID was applied, I observed that the X coordinate distribution of the third track showed a discrepancy between data and Monte Carlo in the selected Ke3 events which was absent in the selected normalizer events (Figure 9.6). The size of the discrepancy was about 0.5% of the Ke3 sample. An obvious explanation was that some local Cerenkov inefficiencies were not measured accurately enough due to the lack of statistics. The fact that the problem area was close to X=0, where Cerenkov counters had large inefficiencies caused by deformed beam tubes, further strengthens this proposition. The attempt to remove the discrepancy by adjusting the binning of the Cerenkov efficiency map was unsuccessful. As none of the binning methods showed any significant improvement in the X distribution discrepancy and the double ratio varied by 0.5% depending on which binning was applied, I ascribed 0.5% systematic error due to the uncertainty in Cerenkov efficiencies in case of the (2/2) e^+ PID.

The application of (2/3) PID significantly decreases the discrepancy in the X distribution of the third track in the Ke3 sample (Figure 9.6). This improvement was expected since the (2/3) PID reduced the effect of the uncertainty in the measured efficiency of a counter on the efficiency of the e^+ identification.

Table 9.10 shows Ke3 positron PID efficiency as well as the resulting contamination of the selected Ke3 sample by other modes.

Table 9.10: PID efficiency for the Ke3 e^+, and selected Ke3 sample contamination (from Table 8.2) for the two alternative e^+ identification methods. All numbers were obtained from Monte Carlo simulation.

	Efficiency	Contamination (%)
(2/2) e^+ PID	0.9603(0.0005)	0.018(0.002)
(2/3) e^+ PID	0.9985(0.0001)	0.025(0.003)

The double ratio obtained with the (2/3) e^+ PID differed by 0.5% from the one obtained with the (2/2) identification. This difference was compatible with both the estimated uncertainty of the (2/2) PID and with the size of the discrepancy observed when the (2/2) PID was used.

Application of the Cerenkov efficiency maps with different binning resulted in 0.3% variation of the double ratio when (2/3) e^+ PID was used. Taking into account that the (2/3) PID led to the better agreement between data and Monte Carlo and that its use introduced a smaller systematic error, I used (2/3) PID to obtain the final result and ascribed 0.3% systematic uncertainty due to the inacuracies in the Cerenkov counter efficiencies.

9.5 Geometric acceptance of the Detector

The geometric acceptance of the detector for the kaon decays in question was less than 10% and depended on the decay mode. To test how well this acceptance was simulated I applied additional aperture cuts to both data and Monte Carlo. The single and double ratios for these cuts are presented in the Table 9.11

I used 0.2% as the systematic error due to the geometric acceptance.

9.6 Selected sample contamination

Contamination of the selected Ke3 and Kdal samples and the systematic errors connected with it are discussed in detail in Section 8. The uncertainty of the contamination by other decay modes was found to be 0.3% and 0.06% for the Ke3 and Kdal samples respectively. The uncertainty of the contamination by 2+1 accidentals was 0.05% and 0.07% for the Ke3 and Kdal samples. Finally, the contamination by upstream (from the decay volume) decays was assumed to be negligble and the error

Table 9.11: Dependence of the single and double ratios on the aperture cuts. Inner aperture cut increased the size of the beam hole in C1 and C2 by 10cm cm in both X and Y. Outer aperture cut decreased the C1 and C2 outer aperture by 10cm in X and Y. Outer cut at PWC1 decreased the outer aperture at the Z position of the first PWC by 10cm and and 5cm in X and Y directions respectively. All single ratios were normalized to be one when no additional aperture cuts were applied. Statistical errors of less than 0.1% are not listed.

	$(MC/Dat)_{Ke3}$	$(MC/Dat)_{Kdal}$	Kdal/Ke3
No additional aperture cut	1.000(0.005)	1.000(0.002)	1.000(0.005)
Outer aperture cut	0.999(0.001)	0.998(0.001)	0.999(0.002)
Inner aperture cut	0.995(0.002)	0.996(0.001)	1.001(0.002)
Outer aperture cut at PWC1	0.996(0.001)	0.998	0.998(0.001)

associated with such assumption was incorporated in the systematic uncertainty of the final result due to the vertex quality cut (Section 9.2.1). The important check of this assumption was the full reconstruction of the π^0 (both for the Ke3 and Kdal samples), as upstream decays would have the reconstructed vertex in the wrong place and therefore the probability of the π^0 reconstruction would be much smaller than for the decays that occurred and were correctly reconstructed inside the decay volume.

For the full π^0 reconstruction I assumed that all reconstructed clumps in the calorimeter that were not associated with the three charged tracks were caused by photons. The reconstructed vertex and the clump in the calorimeter provided the photon "track". In each event, photons that produced low ($< 20MeV$) invariant mass with any of the three charged tracks were not considered as a candidate for the photon from the $\pi^0 \to e^+e^-\gamma$ decay. This was done in order to eliminate the Internal Bremsstrahlung photons that were present in the data but were not simulated explicitly in the Monte Carlo. For each of the remaining photons in a event, the invariant $e^+e^-\gamma$ mass was calculated. If the best (closest to the π^0 mass) mass was inside $(0.1365 \pm 0.03)GeV$ (about ± 3 sigmas), the π^0 was claimed to be reconstructed. The efficiency of this reconstruction was about 30% and was determined mostly by the geometric acceptance of the calorimeter to the photons from the $\pi^0 \to e^+e^-\gamma$ decay.

Figure 9.7 shows the reconstructed π^0 mass for the Ke3 and Kdal samples.

I divided each of the selected Ke3 and Kdal samples into two idepenedent samples: the one where π^0 reconstruction was successful and the one where it failed. As the usptream decays would be unlikely to have π^0 reconstructed, a significant difference

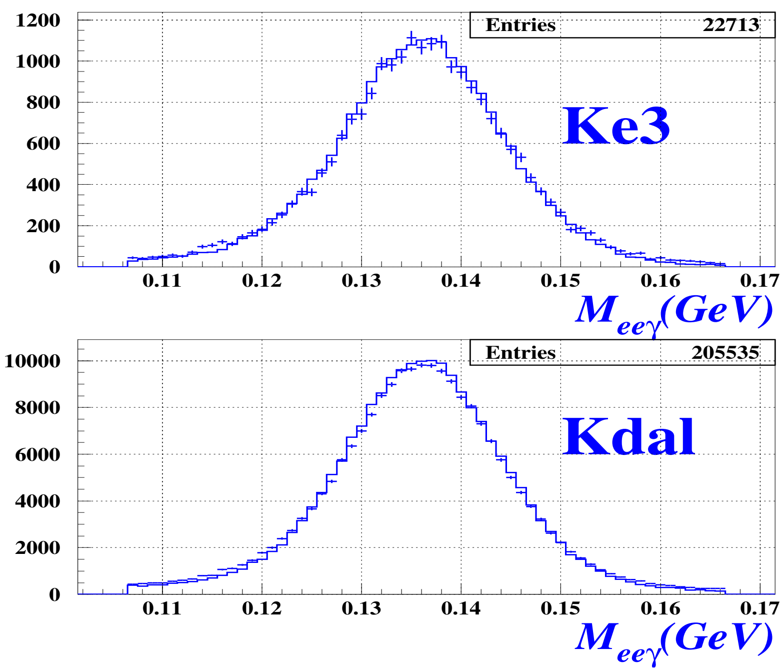

Figure 9.7: Reconstructed π^0 mass. Histogram represents Monte Carlo, while points with errors represent data.

between the double-ratios of these two samples would point at the usptream decays present in the data but not in the Monte Carlo. Table 9.12 shows the single and double ratios for events where π^0 was and was not found.

Table 9.12: Single and double ratios for events where π^0 was and was not found. Single ratios were normalized to be one when no attempt to reconstruct the π^0 was made.

	$(MC/Dat)_{Ke3}$	$(MC/Dat)_{Kdal}$	Kdal/Ke3
π^0	1.008(0.008)	1.011(0.004)	1.003(0.009)
NO π^0	0.996(0.006)	0.993(0.003)	0.997(0.007)

One can see that the difference in the double ratios was $(0.6 \pm 1.1)\%$ and was not statistically significant. The variations in the single ratios were explained by the overall overestimation by the Monte Carlo of the π^0 reconstruction efficiency.

The π^0 reconstruction test did not contradict the assumption that the upstream decays can be neglected.

The overall systematic error connected with the selected samples's contamination was calculated as a quadratic sum of the errors connected with contaminations by other kaon decays and by 2+1 accidentals for both Ke3 and Kdal samples:

$(\sqrt{0.3^2 + 0.06^2 + 0.05^2 + 0.07^2})\% = 0.3\%$ and $(\sqrt{0.2^2 + 0.06^2 + 0.05^2 + 0.07^2})\% = 0.2\%$ for the case of (2/3) and (2/2) e^+ identification respectively.

9.7 Discrepancies between data and Monte Carlo distributions

In the previous sections, I described and estimated uncertainties directly connected with conceivable sources of the systematic bias in the obtained result: event reconstruction, selection criteria, detector efficiencies, detector's geometric acceptance, and sample contamination. Uncertainty estimate in each case was done by applying additional selection criteria, or varying some reconstruction/simulation parameters relevant to the systematic error source in consideration. However, there is another very powerful, albeit not very certain tool that was used: comparison of event characteristics distributions between data and Monte Carlo. This tool is powerful because any significant disagreement between data and Monte Carlo indicates potential systematic uncertainty, and careful comparison might illuminate an error which would have been overlooked otherwise. This tool is not very certain because it gives no direct recipe for how to convert a discrepancy observed in any given distribution (or a set of distributions) into a quantitative systematic uncertainty.

Agreement between data and Monte Carlo has been scrutinized through the course of this analysis and improved as the analysis progressed. Some examples of how comparison of data and Monte Carlo distributions affected improvements in the analysis and/or led to additional systematic uncertainties are listed below.

- Investigation of the initially observed discrepancy in track χ^2 led to observation of the discrepancy in the frequency of multiwire clusters and consequently to the change in PWC response simulation that significantly reduced the χ^2 distribution discrepancy (Figure 6.3). While the resulting change in the Monte Carlo events acceptance was less than 0.2% (within statistical error of the compared Monte Carlo samples), the elimination of the χ^2 distribution discrepancy increased the final result reliability.

- Comparison of data and Monte Carlo distributions of the invariant mass of the e^+e^- pair from the $\pi^0 \to e^+e^-\gamma$ decays (called Mee1) allowed fine-tuning of the overall E865 spectrometer magnetic field scale. Resulting distributions agree very well between data and Monte Carlo (Figure 9.5).

- The initially observed excess of Monte Carlo events with positron tracks close to the beam in the horizontal direction was traced to systematic uncertainties in the Cerenkov counter efficiencies. As a result, an alternative e^+ identification method was developed, which reduced this discrepancy and the corresponding systematic error (Figure 9.6).

- At the early stages of the analysis I noticed that the vertical (Y) distributions of the reconstructed tracks were not symmetric and that the asymmetry was different in data and in Monte Carlo. Extensive study of this effect led to improvements in Monte Carlo simulation and in the PWC spatial alignment. This particular discrepancy and the simulation/reconstruction changes are discussed in more detail in the following section.

- The observed excess of data events (compared to the Monte Carlo prediction) with low value of invariant mass between e^- and the second positive track (e^+ for the Ke3 and $(\pi/\mu)^+$ for the Kdal events) resulted in extensive investigation that led to addition of the decay chains with π^0 decaying through the $\pi^0 \to e^+e^-e^+e^-$ process. Addition of these decay chains significantly reduced the discrepancy and increased the predicted contamination of the selected Ke3 sample (hence decreased the observed Ke3/Kdal ratio) by about 1.5% (Table 8.2). Application of the radiative corrections to the phase space distribution of the Monte Carlo events at the final stages of the analysis completely removed the discrepancy (Figure A.1).

- Reconstructed momentum spectra of the electron and positron from the $\pi^0 \to e^+e^-\gamma$ decay both show significant excess of data events with low (below 0.8GeV/c) momentum. This discrepancy was not resolved and is discussed further in this chapter.

All other relevant distributions show satisfactory agreement between data and Monte Carlo. The main distributions characterizing reconstructed event kinematics are presented in the Appendix.

9.7.1 Vertical coordinate and angle distributions

Discrepancy in the distribution of the vertical track position was observed in the early stages of the Ke3 analysis. This discrepancy was most pronounced in the Y coordinate and angle of both electron and positron from the $\pi^0 \to e^+e^-\gamma$ decay and had a similar form for the selected Ke3 and Kdal events. I chose the vertical angle of the e^- distribution at the Z coordinate of the calorimeter (DY_{e^-}) as an indicator of this problem.

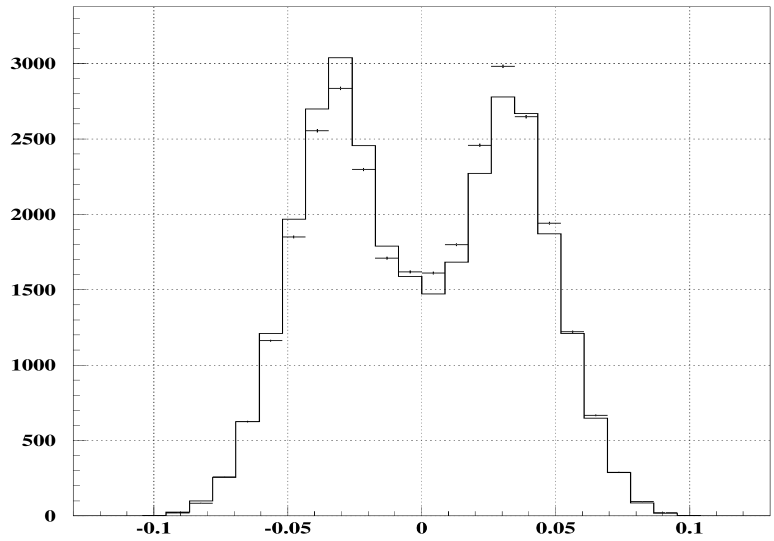

Figure 9.8: Shown is the distribution of the Y (vertical) angle of the e^- from the (Ke3+Kdal) sample at the calorimeter position as observed at the early stages of the analysis. Histogram represents Monte Carlo, while points with errors represent data.

Figure 9.8 shows the comparison between data and Monte Carlo for the DY_{e^-} parameter as first observed in the course of this analysis. One can see that significant "top/bottom" inconsistency between data and Monte Carlo was present. I quantified this discrepancy by dividing both Ke3 and Kdal into two independent samples: with DY_{e^-} less and larger than 0. The variation of the double ratio between these two samples and the one that included all events was used as the estimate of the systematic uncertainty connected with the "up/down" discrepancy (Table 9.13). While the double ratio varied only by $\pm 1\%$, the single ratios for the Ke3 and Kdal samples varied by as much as $\approx 5\%$.

In general, "up/down" asymmetry of the data (or Monte Carlo) coordinate/angle distribution was caused by the vertically asymmetric aperture of the downstream decay tank vacuum window flange and by asymmetric efficiencies of the detector. The vacuum window flange was carefully surveyed and I incorporated the results of this survey into the Monte Carlo simulation software. This step resulted only in marginal reduction of the discrepancy. I did not find any significant correlation of this discrepancy with uncertainties in the detector efficiencies. In the end, the discrepancy was greatly reduced after I implemented the updated PWC spatial alignment (prepared by the University of Pittsburgh group). The final DY_{e^-} distributions for the selected Ke3 and Kdal samples is shown in Figure 9.9.

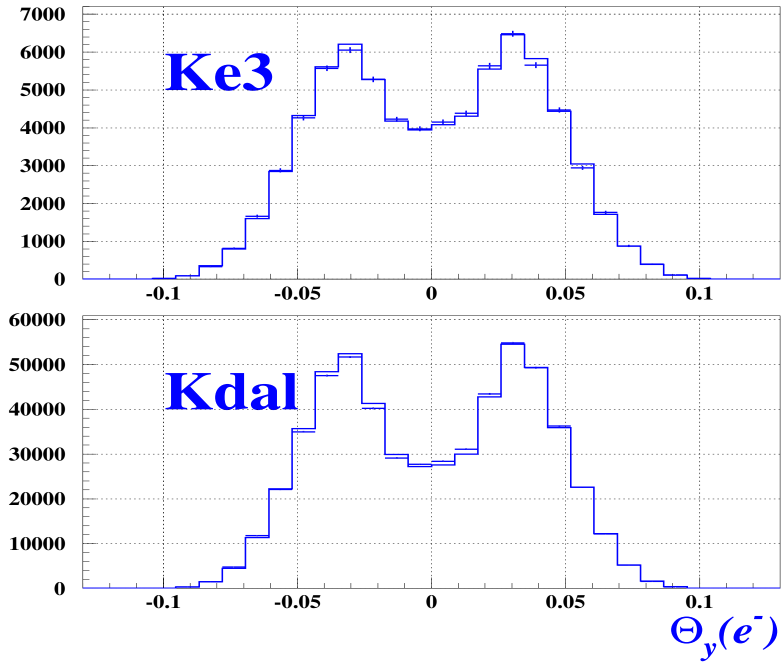

Figure 9.9: Distribution of the vertical angle of the e^- track from the selected Ke3 and Kdal events. Histogram represents Monte Carlo, while points with errors represent data.

While the variation of the double-ratio caused by DY_{e^-} cut (Table 9.13) remained at the level of $\pm 1\%$, the variation of the single ratios was significantly reduced.

It is important to note that the implementation of the new PWC alignment did not significantly (within statistical errors) change the double ratio. This fact coupled with the marked improvement in data to Monte Carlo agreement allowed me to conclude that while the "up/down" discrepancy was connected with the accuracy of the PWCs' position and orientation, the final result (double-ratio) was not very sensitive to this accuracy. I conservatively assigned 0.8% systematic error to the discrepancy in the vertical distribution of reconstructed tracks.

9.7.2 *Momentum spectra of e^+ and e^- from the $\pi^0 \to e^+e^-\gamma$ decay.*

The momentum distribution of both e^+ and e^- from the $\pi^0 \to e^+e^-\gamma$ decay differs significantly between data and Monte Carlo (Figures 9.10 and 9.11).

Excess data events with lower momentum were observed in both Ke3 and Kdal samples.

Table 9.13: Dependence of the single and double ratios on the DY_{e^-} cut. Three upper rows show the variation observed in the early stage of the analysis (before implementation of the updated PWC spatial alignment). Lower rows show variation for the final sample of data and Monte Carlo. Single ratios for no cut were normalized to be one both for the samples obtained with the old and the updated PWC alignment.

	$(MC/Dat)_{Ke3}$	$(MC/Dat)_{Kdal}$	Kdal/Ke3
no DY_{e^-} cut	1.000(0.007)	1.000(0.006)	1.000(0.008)
$DY_{e^-} < 0$	1.032(0.01)	1.046(0.008)	1.013(0.013)
$DY_{e^-} > 0$	0.967(0.01)	0.957(0.008)	0.989(0.013)
no DY_{e^-} cut	1.000(0.005)	1.000(0.002)	1.000(0.005)
$DY_{e^-} < 0$	1.003(0.007)	1.011(0.003)	1.008(0.008)
$DY_{e^-} > 0$	0.997(0.007)	0.990(0.003)	0.993(0.008)

The momentum discrepancy was described by the variation of the double ratio when both P_{e^+} and P_{e^-} were required to be above 0.8GeV/c. Several potential discrepancy sources were considered.

- Effect of the detector aperture (fiducial volume). The low momentum cut-off ($\approx$ 0.5GeV/c) was determined by the spectrometer acceptance. Some discrepancy at the very low end of the momentum spectra would not have been surprising, as sharp acceptance cut-off is generally hard to simulate. As the observed discrepancy extends to the much higher momentum range, it was unlikely that any uncertainty in the fiducial volume simulation was the cause of the discrepancy. This was checked by rejecting events close to the outer aperture of the detector ($|Y_{PWC1}| < 25$cm and $|X_{C2}| < 125$cm were required for each of the three reconstructed tracks). Application of these cuts did not change the discrepancy.

- Reconstruction of the tracks' momentum. Systematic bias in the value of the reconstructed momentum could be caused by the inaccuracy of the magnetic field map, by uncertainty in the PWC spatial alignment, or by systematic bias in the momentum fit procedure. These possible systematic bias sources were checked in several ways. Firstly, the aperture cuts described above rejected events that traversed regions with non-linear magnetic field; therefore the lack of change in the discrepancy suggests that it was not connected to the uncertainties of the non-linear magnetic field regions. Secondly, I artificially increased the magnitude of e^+/e^- momentum in data events by 1%. This increase resulted in the better (visually) agreement between data and Monte Carlo, but the

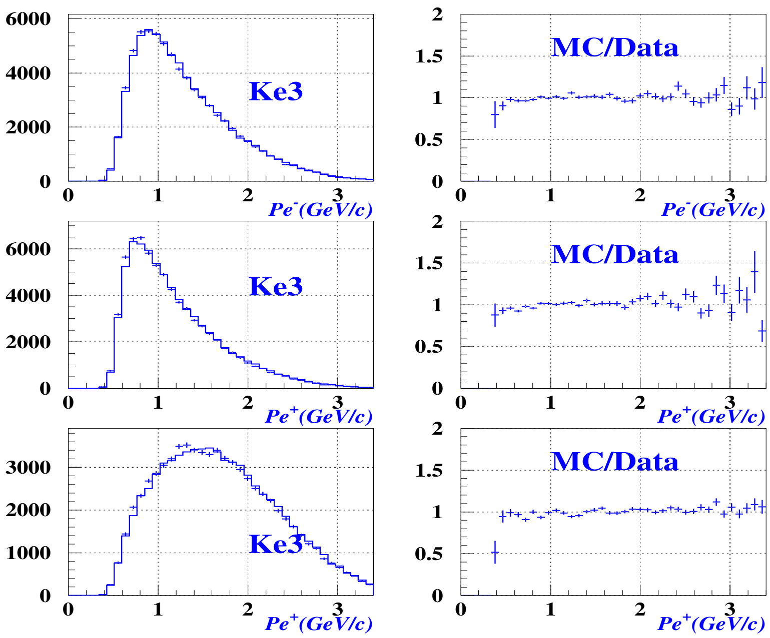

Figure 9.10: Distributions of the reconstructed momentum of the three charged tracks in the selected Ke3 sample. The lowest plots correspond to the e^+ from the Ke3 decay itself, while the ones in the middle correspond to the e^+ from the $\pi^0 \to e^+e^-\gamma$ decay. Histogram represents Monte Carlo, while points with errors represent data. Plots on the left show bin by bin Monte Carlo to data ratio.

variation of the double ratio after application of the momentum cut did not change significantly. Finally, the discrepancy remained the same both when the constrained vertex fit was used, and when the old (not fine-tuned) PWC alignment was applied. Therefore, I could not connect the discrepancy with these sources of the systematic bias in the track momentum reconstruction.

- Sample contamination. Decays occurring upstream of the decay volume were not simulated in the Monte Carlo. As discussed in Chapter 8 and Section 9.6, such decays would be greatly suppressed by the full reconstruction of the π^0. Since the momentum discrepancy did not change significantly for the sample with the reconstructed π^0, the upstream decays were unlikely to be the cause of the discrepancy.

- Detector efficiencies. I checked that the variation of the detector efficiencies used in the Monte Carlo did not affect the discrepancy.

The momentum discrepancy in the third track appeared to be smaller and was less significant, perhaps due to the much lower fraction of events with low momentum.

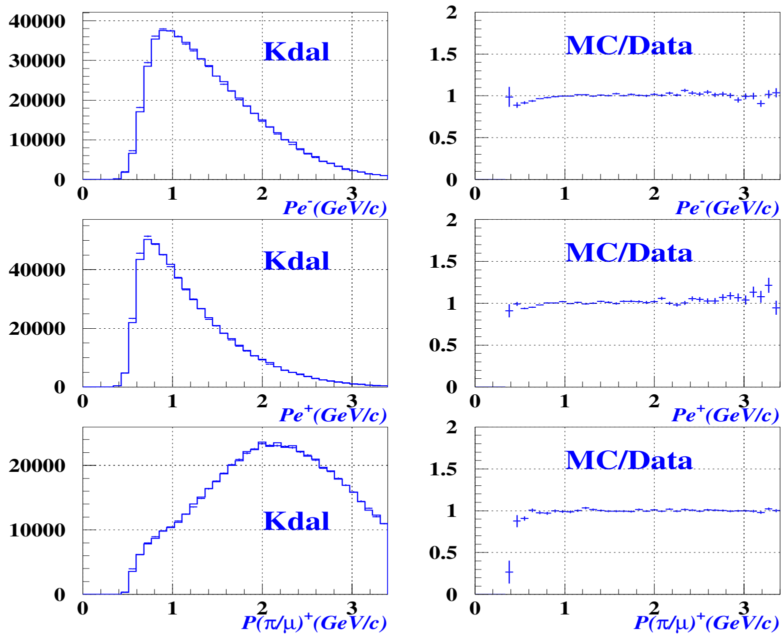

Figure 9.11: Distributions of the reconstructed momentum of the three charged tracks in the selected Kdal sample. Histogram represents Monte Carlo, while points with errors represent data. Plots on the left show bin by bin Monte Carlo to data ratio.

In order to study a posiible correlation between the momentum discrepancy and the vertical track's position/angle discrepancy (previous Section), I compared the variation of the double ratio caused by momentum cut for events with DY_{e^-} larger and smaller than 0. The variation was compatible between the two samples. Therefore, I concluded that the momentum discrepancy and the vertical spatial discrepancy were not correlated.

The final estimate of the systematic error connected with the momentum discrepancy is presented in Table 9.14.

One can see that the double ratio (final result) varied by $\pm 1.3\%$ depending on the applied momentum cut. The cut value (0.8GeV/c) was chosen because it separated the low momentum region where the bin-by-bin Monte Carlo to data ratio (Figures 9.10, 9.11) began to change, and because it divided the data into two independent samples of about the same size.

As I could not determine the definite source of the problem, the variation of 1.3% in the double ratio was used as the estimate of the systematic error connected with the momentum distribution discrepancy between data and Monte Carlo. The apparent connection of the momentum discrepancy to the spectrometer might be an indication of some residual magnetic field and/or PWC alignment problem.

Table 9.14: Dependence of the single and double ratios on the momentum cut. All single ratios were normalized to be one when no additional aperture cuts were applied

	$(MC/Dat)_{Ke3}$	$(MC/Dat)_{Kdal}$	Kdal/Ke3
Standard selection	1.000(0.005)	1.000(0.002)	1.000(0.005)
$P_{e^+} > 0.8GeV/c$ .AND. $P_{e^-} > 0.8GeV/c$	1.032(0.006)	1.019(0.003)	0.987(0.007)
$P_{e^+} < 0.8GeV/c$ .OR. $P_{e^-} < 0.8GeV/c$	0.954(0.006)	0.967(0.003)	1.013(0.007)

9.8 Trigger efficiencies

The ELER trigger used to collect both Ke3 and Kdal events required at least one hit in each of the four Cerenkov counters. While this requirement was aimed at the selection of events with e^+e^- pairs (common feature of the Ke3 and Kdal events), the presence of an additional positron in the Ke3 decay could result in a sytematic difference in trigger efficiency for the Ke3 and Kdal events.

The ELER trigger efficiency was measured using Ke3 and Kdal events that were found in the sample of events that had prescaled T0 trigger latch set. These events did not require the ELER trigger to fire in order to be collected. Both Ke3 and Kdal samples were selected from the pool of these events using the standard selection criteria. The fraction of the selected events that had the ELER trigger latch reflected the efficiency of the Cerenkov part of the ELER trigger (ELER relative to T0). The same procedure was performed using CLAND (T0 and the two left Cerenkov counters) trigger as a reference. Results are shown in Table 9.15.

Table 9.15: ELER trigger efficiencies relative to T0 and CLAND triggers. Numbers in parenthesis are the numbers of events with reference (denominator) and reference+ELER (nominator) trigger latches. Errors are statistical.

Reference trigger	ELER efficiency for the Ke3 events	ELER efficiency for the Kdal events
Prescaled T0	(92/94)=0.979±0.015	(621/632)=0.983±0.005
CLAND	(3642/3684)=0.989±0.002	(28713/28993)=0.990±0.001

One can see that the ELER efficiencies were statistically compatible when measured against T0 and CLAND triggers. Since the CLAND trigger provided much better statistical accuracy, the difference between 0.989 and 0.990 (Ke3 and Kdal efficiencies) was used as a systematic uncertainty connected to the ELER trigger efficiency.

9.9 Ke3 vector form-factor slope

Table 9.16: The double ratio variation with the change of the Ke3 vector form factor slope (λ_+) used in the Ke3 decay simulation. Double ratio was normalized to be one with the nominal λ_+ (upper row). Uncertainties are below 0.1% and are not shown.

λ_+ value	Kdal/Ke3
$\lambda_+ = 0.0282$	1.000
$\lambda_+ = 0.0282(1 + 0.1)$	1.001
$\lambda_+ = 0.0282(1 - 0.1)$	0.999
$\lambda_+ = 0$	0.986

The accuracy of the simulated decay phase space density affected the predicted acceptance. This was a second order effect in the normalizer sample, as the Kdal mix was dominated by the two-body $K^+ \to \pi^+\pi^0$ decay.

The vector form-factor slope λ^+ of the Ke3 decay is known with accuracy of about 10% ($\lambda^+ = 0.0282 \pm 0.0027$ [2]). In order to study the effect of the λ^+ value uncertainty on the final result, I varied the value of the slope parameter used in the Ke3 simulation. The resulting variation of the double ratio is shown in Table 9.16.

Variation of the double ratio caused by $\pm 10\%$ change in the λ^+ value was taken as a systematic error due to the uncertainty of λ^+.

9.10 Correlations between different systematic sources

The two largest systematic uncertainty sources were the discrepancies between data and Monte Carlo in the track momentum distributions and in the vertical position/angle distributions. In the course of their study, they were checked for correlations with the other known systematic sources. As described in Section 9.7, no correlation was found. The two discrepancies also did not show correlation between themselves. I concluded that all of the investigated systematic uncertainty sources were uncorrelated and should be considered independent for the purpose of obtaining total systematic error.

9.11 Summary

Systematic uncertainties from different sources are summarized in Table 9.17.

Table 9.17: Systematic uncertainty sources and estimates of their respective contributions to the error of the final result. The total error is equal to $\sqrt{\sum \sigma_i^2}$. The errors for two different e^+ identification methods are listed.

Source of systematic error	Estimated error (2/2) e^+ PID	Estimated error (2/3) e^+ PID
Magnetic field uncertainty	0.3%	0.3%
Vertex finding and quality cut	0.6%	0.6%
Vertex position cut	0.1%	0.2%
Cerenkov Ambiguity Cut	0.3%	0.3%
M_{ee} cut	0.2%	0.2%
Detector Aperture	0.2%	0.2%
$(\pi/\mu)^+$ identification	0.04%	0.04%
PWC efficiencies	0.2%	0.2%
D counter efficiencies	0.15%	0.15%
Cerenkov efficiencies	0.5%	0.3%
Contamination of the selected samples	0.2%	0.3%
Vertical spatial/angle distributions agreement	0.8%	0.8%
e^+/e^- momentum distributions agreement	1.3%	1.3%
ELER trigger efficiency	0.1%	0.1%
Uncertainty in the Ke3 form factor slope	0.1%	0.1%
Total error	1.8%	1.8%

Total systematic error was calculated assuming independence of the different systematic uncertainty sources, as no significant correlations between them were observed.

The two largest contributions to the error come from the discrepancies in the spatial and momentum distributions between data and Monte Carlo. In both cases the error was determined by dividing Ke3 and Kdal events in two roughly equal samples and observing the double ratio variation. While I could not determine the exact source of either of these two discrepancies, the change of the vertical distribution discrepancy with the PWC alignment and apparent connection of the momentum discrepancy to the spectrometer, indicate that the error might be connected to the magnetic field and PWC alignment. While PWC alignment was greatly improved, the magnetic field map study was more complicated. The new precise field mapping would have involved a considerable effort (if at all possible) and at the moment, we decided against it. Such measurement now can not be done since the magnets are no longer in place. But even in hindsight, the existing indications might not have justified such an undertaking.

Table 9.17 shows errors for the two alternative e^+ identification methods. While the total error was the same for the (2/2) and for the (2/3) e^+ PID, the (2/3) method was preferable, as it significantly decreased the error connected with the Cerenkov counters efficiencies. I used the (2/3) e^+ PID for the final result.

CHAPTER 10
CONSISTENCY CHECKS

While the systematic error of the Ke3/Kdal ratio has been exhaustively studied, an independent check of our estimate of its value was desirable. The consistency checks performed are described in the following sections.

10.1 BR($K^+ \to \pi^+\pi^+\pi^-$)/Kdal

An estimate of the $K^+ \to \pi^+\pi^+\pi^-$ decay branching ratio relative to Kdal was a very stringent test of the quality of our data, Monte Carlo simulation, and understanding of the systematic errors. Unlike the Ke3, the $K^+ \to \pi^+\pi^+\pi^-$ decay differs greatly from the Kdal both in the final particle composition and in the kinematics. While we aimed at, and in fact observed in this analysis, the cancellation of systematic uncertainties between the Ke3 and the Kdal events, such cancellation was almost completely absent between the $K^+ \to \pi^+\pi^+\pi^-$ and the Kdal. Therefore, the level of agreement between our BR($K^+ \to \pi^+\pi^+\pi^-$)/Kdal estimate and the prediction based on the results of the previous experiments was a very sensitive indicator of our understanding of the data. Both Kdal and $K^+ \to \pi^+\pi^+\pi^-$ branching ratios are known with uncertainty below a percent; therefore the prediction could be made with accuracy adequate to test our 1.8% estimate of the systematic error.

Several ingredients were needed to make an estimate of the BR($K^+ \to \pi^+\pi^+\pi^-$)/Kdal.

- The π^0 from the Kdal decay mix was always detected through the $\pi^0 \to e^+e^-\gamma$ decay. The experimental measurement accuracy of this decay branching ratio is about 2.7% ($BR(\pi^0 \to e^+e^-\gamma) = (1.198 \pm 0.032)\%$ [2]). This branching ratio uncertainty did not affect the Ke3/Kdal measurement, since both signal and normalizer included the $\pi^0 \to e^+e^-\gamma$ decay. However, it would translate directly into the 2.7% uncertainty of the $K^+ \to \pi^+\pi^+\pi^-$/Kdal prediction. I chose to use the theoretical prediction for the $\pi^0 \to e^+e^-\gamma$ branching ratio [34]. While the quoted paper presents the result of the precise QED calculation of the $\Gamma(\pi^0 \to e^+e^-\gamma)/\Gamma(\pi^0 \to \gamma\gamma)$ ratio, one can calculate BR($\pi^0 \to e^+e^-\gamma$) from it using the fact that the two decays account for all but 0.004% of the total π^0 decay rate. The result is $BR_{QED}(\pi^0 \to e^+e^-\gamma) = (1.184 \pm 0.002)\%$.

- The $K^+ \to \pi^+\pi^+\pi^-$ decay events were collected with the prescaled T0 trigger. The analog prescale modules allowed only for an approximate setting; therefore the exact prescale value had to be determined from the collected data. As all ELER triggers required the T0 to be satisfied, the exact prescale value was determined as

$$PS = \frac{N(T0ps.and.ELER)}{N(ELER)} = 0.001108 \pm 0.00002 \qquad (10.1)$$

  where $N(T0ps.and.ELER)$ and $N(ELER)$ are the number of events that had prescaled T0 and ELER trigger latches. The uncertainty in the calculated prescale factor was determined by the sample size.

- The efficiency of the ELER trigger relative to T0 should be taken into account. For the Kdal decays this efficiency was $(98.3 \pm 0.5)\%$ (Section 9.8).

Taking all of the above into account, my estimate was:

$$\frac{BR(K^+ \to \pi^+\pi^+\pi^-)}{Kdal} = (1.01 \pm 0.02) \times R_{PDG} \qquad (10.2)$$

where R_{PDG} is the prediction based on branching ratios listed by the Particle Data Group. The 2% error was determined by combining all relevant uncertainties, and was dominated by the 1.8% uncertainty of the prescale factor. No systematic uncertainty of the measurement was included. The observed 1% difference with the prediction did not contradict the 1.8% estimate of the systematic uncertainty from the previous Section, and strengthened our confidence in the quality of this analysis.

10.2 1997 Ke3 Data

Two sets of Ke3 data were collected by the E865 experiment. The first data set was collected in 1997 and the second in 1998. The result in this thesis is based on the 1998 data with 1997 data used for consistency check. The reasons for this are described below.

The first data set was collected during the 1997 running period. The beam intensity was at about 0.6×10^6 kaons per 1.6 second AGS pulse. The 1997 Ke3 trigger differed from the standard E865 trigger in that T0 required only two clumps in the calorimeter instead of three. This was done in order to minimize possible trigger bias between Ke3 and Kdal events due to the difference in energy deposited in the calorimeter by positron (Ke3) and pion/muon (Kdal). At the same time, as the calorimeter, A-hodoscopes, and D-hodoscopes were always required in the trigger, there was no model independent way to obtain their efficiencies. The ELER trigger efficiency also could not be obtained from the data.

The calorimeter efficiencies were obtained by the iteration procedure of comparing the hit frequency in each module between data and Monte Carlo using $K^+ \to \pi^+\pi^+\pi^-$ decays. The same procedure was performed for the A and D hodoscopes. This method of efficiency determination had two flaws:

- Since the $K^+ \to \pi^+\pi^+\pi^-$ decay has much smaller final particle phase space than either Kdal or Ke3, not all of the calorimeter was adequately covered.

- The efficiency measured in this way convoluted into itself inefficiencies of other detector elements and of the reconstruction procedure if they were not taken into account correctly in the Monte Carlo.

While we realized these difficulties, I pursued the 1997 Ke3 data analysis and obtained a preliminary estimate for the BR(Ke3)/Kdal ratio. This estimate was significantly different from the prediction based on the results of previous experiments. This difference combined with the flaws in the experimental setup used for the 1997 data collection resulted in the design of the 1998 Ke3 trigger. As it was clear that a Ke3 sample of appropriate size could be collected in a week or less, it was decided to test and implement the new trigger during the last week of the 1998 $K^+ \to \pi^+\mu^+e^-$ data collecting run (the last week of the experiment itself).

I concentrated on the 1998 Ke3 data analysis, because this data sample, by the virtue of the experimental conditions in which it was obtained, provided a potential for the better understanding and elimination of the systematic uncertainties.

After the 1998 data analysis was completed, I returned to the 1997 data and reanalyzed it using all the improvements in the Monte Carlo and event reconstruction/selection criteria that were developed in the course of the 1998 data analysis.

The difference in the trigger between 1997 and 1998 data did not allow me to exactly duplicate the 1998 analysis. The three major differences were:

- Each of the charged tracks reconstructed in the spectrometer was required to have a reconstructed charged clump in the calorimeter, i.e. at least one module in the calorimeter with the A-hodoscope hit in front of it.

- Calorimeter, A-hodoscope, and D-hodoscope efficiencies were determined by comparing hit distribution in these detectors between data and Monte Carlo.

- The presence (or absence) of the systematic bias between Ke3 and Kdal efficiencies of the ELER trigger could not be tested.

Table 10.1 shows comparison between single and double ratios obtained from the 1998 and 1997 Ke3 data.

Table 10.1: Single and double ratios obtained from the 1998 and 1997 data analysis. Both single ratios for the 1998 and the Kdal single ratio for the 1997 were normalized to be one. All errors are statistical.

Data sample collected in	$(MC/Dat)_{Ke3}$	$(MC/Dat)_{Kdal}$	Kdal/Ke3
1998	1.000(0.005)	1.000(0.002)	1.000(0.005)
1997	1.006(0.004)	1.000(0.003)	0.994(0.005)

One can see that the double ratios did not differ significantly between the two data sets. As the two data sets were obtained and analyzed in different ways, the agreement of the two results greatly increased our confidence in the validity of the result obtained from the 1998 data.

We chose to obtain our final result from the 1998 data because:

- The 1997 trigger was likely to result in larger systematic uncertainties of the 1997 result;

- The estimated systematic error of the 1998 result was much larger than the statistical one. The small benefit of the increased statistical precision from the addition of the 1997 data did not warrant the substantial effort of a thorough systematic uncertainty analysis of the 1997 data.

As the two largest contributions to the estimated systematic error of the 1998 result came from the vertical spatial/angle and from the momentum distribution, it was interesting to see if similar discrepancies were present in the 1997 data. Figures 10.1, 10.2, 10.3 show the DY_{e^-} parameter and the momentum of the three tracks for the Ke3 and Kdal samples from the 1997 data.

One can see (Figure 10.1) that the "top/bottom" discrepancy is present in the 1997 data approximately at the same level as first observed in the 1998 data analysis. This is not surprising considering that the PWC spatial alignment for the 1997 data was not calibrated to the same accuracy as for the 1998. The 1997 double ratio variation with the DY_{e^-} cut was the same as for the 1998.

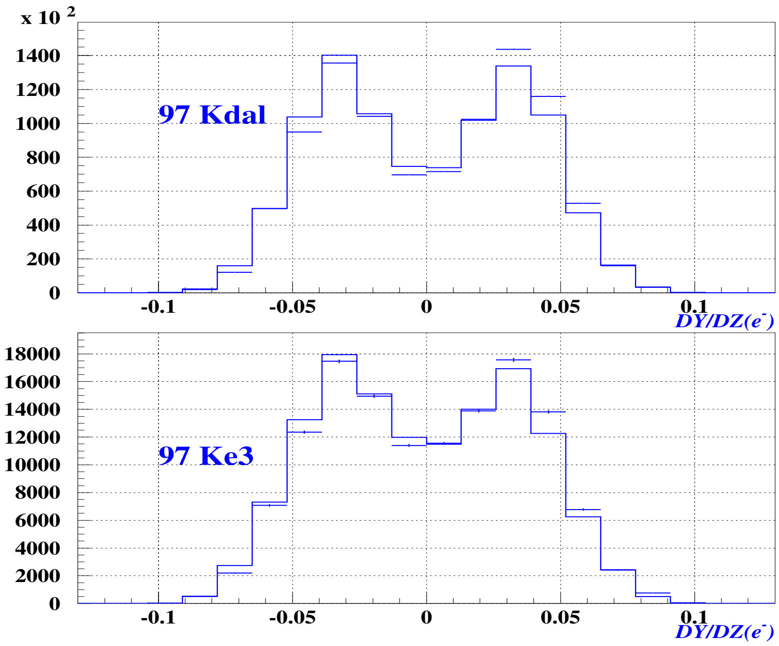

Figure 10.1: Distribution of the vertical angle of the e^- track from the selected Ke3 and Kdal events (1997 Ke3 data). Histogram represents Monte Carlo, while points with errors represent data.

The 1997 discrepancy in the momentum distributions is very different from the one observed in the 1998 data. The 1997 double ratio varied only by 0.3% when the $P_{e^+} > 0.8GeV/c.AND.P_{e^-} > 0.8GeV/c$ was applied. This is much smaller than the 1.3% variation observed in the 1998 data. The difference in the momentum discrepancy between the two samples supports our intuitive idea that the discrepancy itself might be connected with the magnetic field and/or PWC alignment calibration.

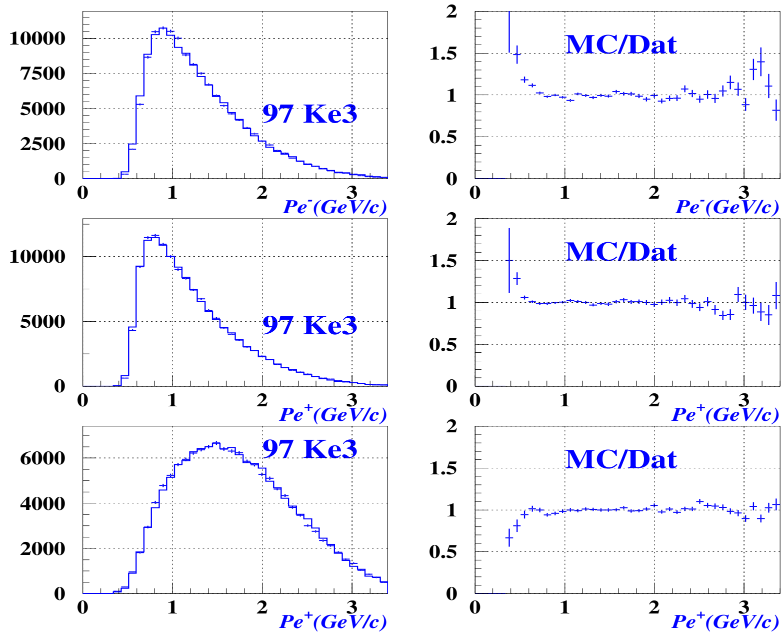

Figure 10.2: Distributions of the reconstructed momentum of the three charged tracks in the selected Ke3 sample (1997 Ke3 data). The lowest plots correspond to the e^+ from the Ke3 decay itself, while the ones in the middle correspond to the e^+ from the $\pi^0 \to e^+e^-\gamma$ decay. The histograms represent Monte Carlo, while points with errors represent data. Plots on the left show bin by bin Monte Carlo to data ratio.

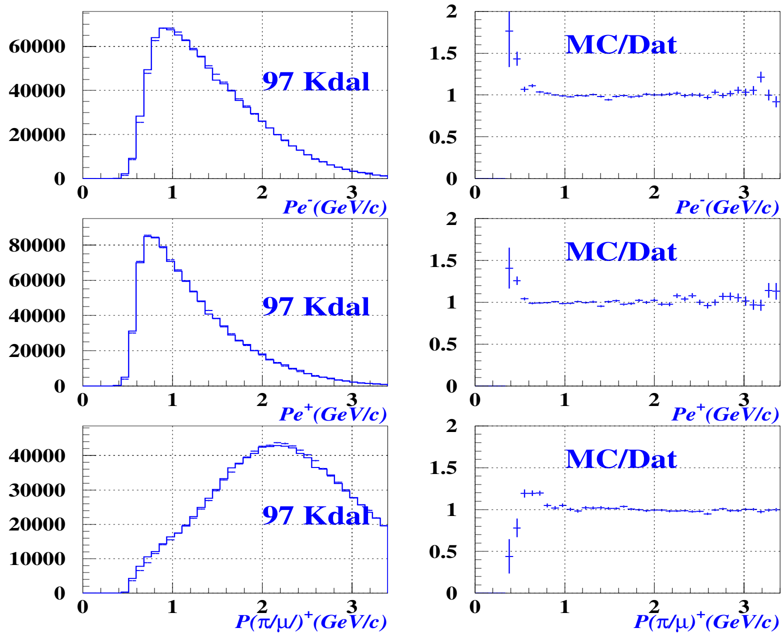

Figure 10.3: Distributions of the reconstructed momentum of the three charged tracks in the selected Kdal sample (1997 Ke3 data). The histograms represent Monte Carlo, while points with errors represent data. Plots on the left show bin by bin Monte Carlo to data ratio.

10.3 Ke3 form factor slope fit

Extraction of the slope parameter of the f_+ vector form-factor was used as an additional check of the analysis quality. We used the standard linear expansion of the form-factor dependence on the momentum transfer:

$$f_+(q^2) = f_+(0)(1 + \lambda_+(q^2/m_\pi^2)). \tag{10.3}$$

where $q = (P_K - P_{\pi^0})$. The q^2 value is connected directly to the π^0 energy in the kaon rest-frame:

$$q^2 = (M_K^2 + M_{\pi^0}^2 - 2M_K E_{\pi^0}) \tag{10.4}$$

Only events with the fully reconstructed π^0 were used in the analysis. The Lorentz transformation from the laboratory to the kaon rest-frame reference system required the knowledge of the kaon momentum vector which was not known for the reconstructed Ke3 decays. Since the kaon beam energy spread was small (about 2%), I used the average kaon momentum from the reconstructed $K^+ \to \pi^+\pi^+\pi^-$ decays (5.969GeV/c) as the kaon momentum magnitude for the purpose of the Lorentz transformation. The kaon direction was obtained from the $K^+ \to \pi^+\pi^+\pi^-$ decay beam profile, including dependence on the Z coordinate of the vertex. About 25% of the decays occur in the downstream part of the decay tank inside the magnetic field of the D5 dipole magnet, and the average beam kaon direction will be different, changing from +5mrad in X for decays at Z = -100cm, to -5mrad in X for Z = +20cm.

The distribution of the square of the missing mass (M_ν^2) for the selected Ke3 sample is shown in Figure 10.4. One can see the excess data events with M_ν^2 around 0.04GeV^2. As described in Section 6.3.2, the $K^+ \to \pi^0 e^+ \nu\gamma$ decays were simulated explicitly only if they were outside of the two-dimensional Ke3 phase space. The remaining radiative corrections were taken into account by modifying the simulated Ke3 decay phase space density. Therefore, the kinematics of all the $K^+ \to \pi^0 e^+ \nu\gamma$ decays that were inside the two-dimensional Ke3 phase space was simulated in the same way as for the three-particle Ke3 decay, i.e. the missing mass was equal to zero. This is certainly not the case in the data. Since we do not expect the radiative Ke3 decays that are inside the two-dimensional phase space to affect the form of the E_{π^0} distribution significantly, all of the events (both data and Monte Carlo) were used for the λ_+ fit.

As the Ke3 decay rate is proportional to the $f_+^2(q^2)$ (Equation 1.8), we can write

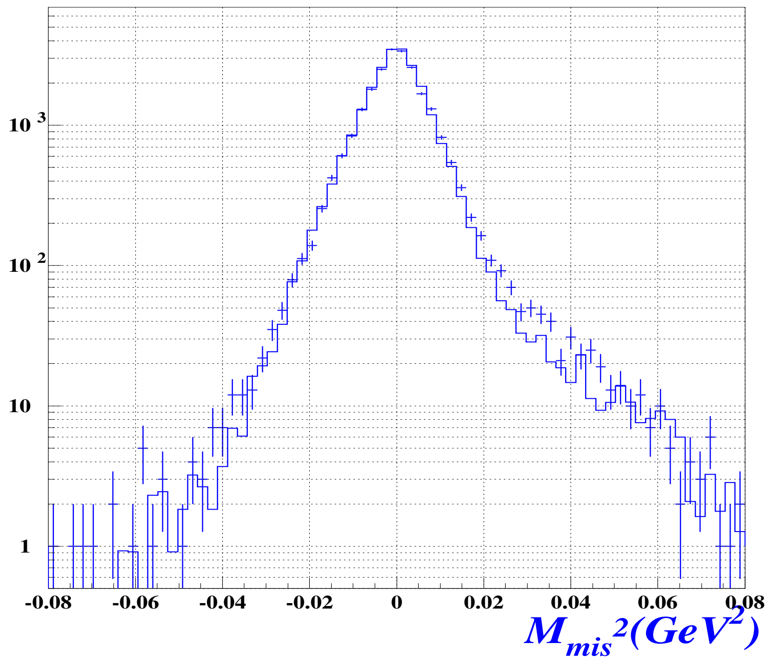

Figure 10.4: Square of the missing mass (M_ν^2) for the selected Ke3 sample. The histogram represents Monte Carlo, while points with errors represent data.

$$\Gamma(Ke3) \propto f_+(0)^2)(1. + 2.(q^2/m_\pi^2)\lambda_+ + (q^4/m_\pi^4)\lambda_+^2) \tag{10.5}$$

The λ_+ fit was done in the following way: First, we created three histograms (h1,h2,h3) of the reconstructed q^2/m_π^2 distribution from the Monte Carlo. Each Monte Carlo event had the weight equal to

$$\begin{aligned} w_{h1} &= 1/(1+\lambda_0 * (q_0^2/m_\pi^2))^2 \\ w_{h2} &= 2.(q_0^2/m_\pi^2)/(1+\lambda_0 * (q_0^2/m_\pi^2))^2 \\ w_{h3} &= (q4/m_\pi^4)/(1+\lambda_0 * (q_0^2/m_\pi^2))^2 \end{aligned} \tag{10.6}$$

for the three histograms respectively. Here λ_0 is the slope parameter used originally for generating Monte Carlo events and q_0^2 is the simulated (as opposed to reconstructed) value of q^2 of the event. After that we minimize the χ^2 function:

$$\chi^2 = \sum_i \frac{((N_{Di} - norm(h1_i + h2_i\lambda_+ + h3_i\lambda_+^2))^2}{\sigma_i^2} \tag{10.7}$$

where sum goes over the bins (i); N_{Di}, $h1_i$, $h2_i$, $h3_i$ are the number of events in the i^{th} bin for the data and the three Monte Carlo histograms respectively, *norm* and λ_+ are the fit parameters, and σ_i is the statistical error of the difference in the numerator. The simulated backgrounds were added bin by bin to the Monte Carlo.

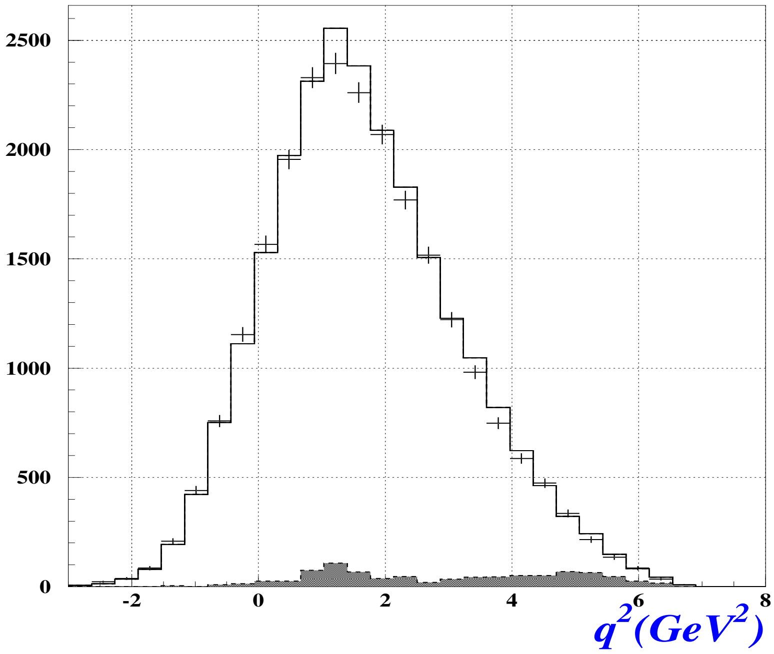

Figure 10.5: Square of the momentum transfer $q^2 = (P_K - P_{\pi^0})^2$ divided by $M^2_{\pi^0}$ of the Monte Carlo events (histogram) after the λ_+ fit was performed. Points with errors represent data. Shaded histogram shows simulated background (non-Ke3 decays).

In the result of the fit (Figure 10.5) we obtain:

$$\lambda_+ = 0.0324 \pm 0.0044 \tag{10.8}$$

In the minimum, the $\chi^2 = 28.39$ was obtained for the 25 degrees of freedom. The reconstructed q^2 value resolution was about 13MeV as obtained from the Monte Carlo.

The similar analysis of the 1997 Ke3 data yielded $\lambda_+ = 0.0290 \pm 0.0044$ with $\chi^2 = 26.67$ per 25 degrees of freedom.

The PDG fit of the previous experimental results gives $\lambda_+ = 0.0282 \pm 0.0027$. The agreement of the λ_+ value extracted from the two independent samples of our data with that from the previous experiments improves our confidence in the obtained result for the $K^+ \to \pi^0 e^+ \nu / Kdal$.

One- and two-dimensional comparisons of the data and Monte Carlo reconstructed phase-space density distributions are shown in figures A.5, A.6, A.7, and A.8.

CHAPTER 11
RESULTS

11.1 BR($K^+ \to \pi^0 e^+ \nu$)/Kdal

The observed ratio of the number of the collected Ke3 to the number of the collected Kdal events can be presented as:

$$\begin{aligned}
\frac{N_D^{Ke3}}{N_D^{Kdal}} &= \frac{BR(Ke3)Acc_{Ke3}^{Ke3} + C^{Ke3}}{Kdal Acc_{Kdal}^{K^+\to\pi^+\pi^0} + BR(Ke3)Acc_{Kdal}^{Ke3} + C^{Kdal}} \qquad (11.1)\\
Kdal &= BR(K^+ \to \pi^+\pi^0)\\
&+ (Acc_{Kdal}^{K^+\to\pi^0\mu^+\nu}/Acc_{Kdal}^{K^+\to\pi^+\pi^0}) \times BR(K^+ \to \pi^0\mu^+\nu)\\
&+ (Acc_{Kdal}^{K^+\to\pi^+\pi^0\pi^0}/Acc_{Kdal}^{K^+\to\pi^+\pi^0}) \times BR(K^+ \to \pi^+\pi^0\pi^0)\\
C^{Ke3} &= \sum_{i\neq 4} BR(i)Acc_{Ke3}^{i}\\
C^{Kdal} &= \sum_{i=5}^{10} BR(i)Acc_{Kdal}^{i}
\end{aligned}$$

where $Acc_{Ke3/Kdal}^{mode}$ is the probability (acceptance) of the decay *mode* to be selected into the Ke3 or Kdal samples, and the sums' index corresponds to the row number in Table 11.1. Table 11.1 lists the pertinent decay chains and their probabilities to be selected in the Ke3 or Kdal samples. The positron from the Ke3 was identified with the (2/3) e^+ PID; the pion/muon from the Kdal was identified with the .not.(2/2) PID. As a result, most of the Ke3 decays selected into the Kdal sample are present in the Ke3 sample as well.

Any decay chains that did not include single $\pi^0 \to e^+e^-\gamma$ decay were viewed as a background that had to be subtracted. Note that in Table 11.1, the decay $K^+ \to \pi^0 e^+ \nu\gamma$ corresponds to the radiative Ke3 decay with kinematics such that, when projected to the two-dimensional phase space (e.g., E_{e^+}; E_{π^0}), events are located outside the borders of the three particle Ke3 phase-space (see Section 6.3.2). These events were treated as a background.

Using Equation 11.1, branching ratios and acceptances from Table 11.1 we can write:

Table 11.1: Branching ratios of the pertinent K^+ decays, and probabilities of them to be selected in the Ke3 or Kdal samples. Probabilities were determined from the Monte Carlo simulation and their errors are statistical. Branching ratios and their errors are taken from [2]. All branching ratios are relative to the $BR(\pi^0 \to e^+e^-\gamma) = (1.198 \pm 0.032)\%$. $K^+ \to \pi^0 e^+ \nu\gamma$ decay corresponds to the radiative Ke3 decays which were outside of the borders of the two-dimensional Ke3 phase-space. The listed $K^+ \to \pi^+\pi^0\pi^0$ acceptance takes into account that any of the two π^0 in the final state can decay into $e^+e^-\gamma$.

Decay Chain	B.R.	Probability to be selected into the Ke3 sample (%)	Probability to be selected into the Kdal sample (%)
$K^+ \to \pi^+\pi^0$; $\pi^0 \to e^+e^-\gamma$	$(21.16 \pm 0.14)\%$	$(0.00133 \pm 0.00008)\%$	$(1.159 \pm 0.002)\%$
$K^+ \to \pi^0\mu^+\nu$; $\pi^0 \to e^+e^-\gamma$	$(3.18 \pm 0.08)\%$	$(0.0014 \pm 0.0001)\%$	$(1.160 \pm 0.003)\%$
$K^+ \to \pi^+\pi^0\pi^0$ with one $\pi^0 \to e^+e^-\gamma$	$(1.73 \pm 0.04)\%$	$(0.0070 \pm 0.0006)\%$	$(1.209 \pm 0.008)\%$
$K^+ \to \pi^0 e^+\nu$; $\pi^0 \to e^+e^-\gamma$		$(0.738 \pm 0.002)\%$	$(0.0312 \pm 0.0004)\%$
$K^+ \to \pi^+\pi^0\pi^0$ with two $\pi^0 \to e^+e^-\gamma$	$(0.0207 \pm 0.0007)\%$	$(0.1 \pm 0.01)\%$	$(0.62 \pm 0.02)\%$
$K^+ \to \pi^+\pi^0$; $\pi^0 \to e^+e^-e^+e^-$	$(0.066 \pm 0.005)\%$	$(0.32 \pm 0.02)\%$	$(1.86 \pm 0.04)\%$
$K^+ \to \pi^0\mu^+\nu$; $\pi^0 \to e^+e^-e^+e^-$	$(0.0100 \pm 0.0008)\%$	$(0.27 \pm 0.02)\%$	$(1.90 \pm 0.06)\%$
$K^+ \to \pi^+\pi^0\pi^0$; $\pi^0 \to e^+e^-e^+e^-$	$(0.0054 \pm 0.0005)\%$	$(0.34 \pm 0.04)\%$	$(2.05 \pm 0.09)\%$
$K^+ \to \pi^0 e^+\nu$; $\pi^0 \to e^+e^-e^+e^-$	$(0.015 \pm 0.001)\%$	$(1.54 \pm 0.06)\%$	$(0.06 \pm 0.01)\%$
$K^+ \to \pi^0 e^+\nu\gamma$; $\pi^0 \to e^+e^-\gamma$	$(0.0245 \pm 0.001)\%$	$(0.26 \pm 0.02)\%$	$(0.012 \pm 0.03)\%$

$$\frac{BR(K^+ \to \pi^0 e^+ \nu)}{KDAL} = \frac{N_D^{Ke3} Acc_{Kdal}^{K^+ \to \pi^+ \pi^0}}{N_D^{Kdal} Acc_{Ke3}^{Ke3}} \times \frac{1}{(1 + A - B)}; \qquad (11.2)$$

$$KDAL = \frac{1}{Acc_{Kdal}^{K^+ \to \pi^+ \pi^0}} \sum_{i \neq 4,9,10} BR(i)(Acc_{Kdal}^i - (N_D^{Kdal}/N_D^{Ke3})Acc_{Ke3}^i);$$

$$A = \frac{BR(DD)Acc_{Ke3}^{Ke3DD} + BR(IB)Acc_{Ke3}^{K^+ \to \pi^0 e^+ \nu \gamma}}{Acc_{Ke3}^{Ke3}};$$

$$B = \frac{N_{Ke3}^D(Acc_{Kdal}^{Ke3} + BR(DD)Acc_{Kdal}^{Ke3DD} + BR(IB)Acc_{Kdal}^{K^+ \to \pi^0 e^+ \nu \gamma})}{N_D^{Kdal} Acc_{Ke3}^{Ke3}}$$

where $BR(DD)$ stands for the $BR(\pi^0 \to e^+e^-e^+e^-)/BR(\pi^0 \to e^+e^-\gamma)$, and $BR(IB) = BR(K^+ \to \pi^0 e^+ \nu \gamma)/BR(Ke3)$. The sum is taken over all decay chains involving the three kaon decay modes that comprised the original $Kdal$ (all decay chains from Table 11.1 except for the $Ke3$, $Ke3\gamma$, and the $Ke3$ decay followed by the Double Dalitz). The values of A and B are small and are calculated using the branching ratios and acceptances from Table 11.1. Note that even though the denominator in the left side of Equation 11.2 looks more complicated than original $Kdal$, it still can be expressed as the linear combination of the branching ratios of the $K^+ \to \pi^+\pi^0$, $K^+ \to \pi^0\mu^+\nu$, and $K^+ \to \pi^+\pi^0\pi^0$ decays. The use of $KDAL$ as the normalizer allows me to eliminate any dependence of the right side of Equation 11.2 on any decay's branching ratio. The two exception are $BR(DD)$ and $BR(IB)$, but both of them are small (less than 1% compared to the Ke3 branching ratio), and therefore their uncertainty affects the result at the level below 0.1%.

The number of the finally selected data events was 71,204 and 558,186 for the Ke3 and Kdal samples respectively. Using the branching ratios and acceptance values from Table 11.1 we obtain

$$\begin{aligned} KDAL &= 0.990 \times BR(K^+ \to \pi^+\pi^0) \qquad (11.3) \\ &+ 0.990 \times BR(K^+ \to \pi^0\mu^+\nu) \\ &+ 0.995 \times BR(K^+ \to \pi^+\pi^0\pi^0) = (25.82 \pm 0.18)\% \\ \frac{BR(K^+ \to \pi^0 e^+ \nu)}{KDAL} &= 0.1998 \pm 0.0008_{stat} \pm 0.0036_{sys} \end{aligned}$$

The error in the KDAL value comes solely from the uncertainties of the relevant branching ratios, since the error connected with the statistical and systematic uncertainties of the acceptances is already included in the error of the $BR(K^+ \to \pi^0 e^+ \nu)/KDAL$. The first error of the $BR(K^+ \to \pi^0 e^+ \nu)/KDAL$ ratio is statistical and is dominated by the size of the collected Ke3 sample; the second error is systematic.

Note that while the $K^+ \to \pi^0 e^+ \nu \gamma$ decays were subtracted as a background, the remaining part of the radiative corrections was taken into account by weighting Monte Carlo Ke3 events with $(E_{e^+}; E_{\pi^0})$ dependent weight calculated based on [12]. Since the $BR(K^+ \to \pi^0 e^+ \nu)/KDAL$ is inversely proportional to the Ke3 acceptance, the application of the radiative correction weight only to the reconstructed Monte Carlo Ke3 events, combined with the subtraction of the aforementioned $K^+ \to \pi^0 e^+ \nu \gamma$ decays, led to the final result, reflecting the branching ratio of the 'bare' $K^+ \to \pi^0 e^+ \nu$ decay (i.e., with all radiative corrections already taken into account).

The $BR(K^+ \to \pi^0 e^+ \nu)/KDAL$ ratio is the final result of this analysis. Because of the small contamination of the Ke3 sample, this result is insensitive to the values of the branching ratios of the decays other than the Ke3 itself. Using the branching ratios from the Particle Data Group, we can calculate the Ke3 branching ratio inferred from our result.

$$BR(K^+ \to \pi^0 e^+ \nu) = (5.16 \pm 0.02_{stat} \pm 0.09_{sys} \pm 0.04_{norm})\% \tag{11.4}$$

The last (normalizer) error is determined by the uncertainty of the rates of the decays comprising the KDAL mix.

The Particle Data Group fit of the results of the previous K^+ decay experiments yields $BR(K^+ \to \pi^0 e^+ \nu) = (4.82 \pm 0.06)\%$ [2]. Our inferred branching ratio differs by more than three standard deviations from the PDG fit. Comparison with the separate experiments is less straightforward, as most of them measure only relative branching ratios. The one experiment that measured the Ke3 decay absolute rate [35] yielded $BR(K^+ \to \pi^0 e^+ \nu) = (4.86 \pm 0.10)\%$, which disagrees with ours by about 2.5 standard deviations. While this difference is intriguing, its exact reasons are beyond the scope of this analysis, where our main goal was to produce an independent measurement. Having said that, I would like to remark that the analysis [35] did not seem to include radiative corrections. In our case, the total radiative corrections amounted to about 1.1% increase in the final result caused primarily by the change in the decay phase-space density due to the soft and virtual radiative corrections that resulted in a "shift" of the positron energy spectrum towards lower energies. The exact effect of the radiative corrections depends ultimately on the acceptance and while 1% is certainly not enough to explain the almost 6-7% difference observed in the results, it decreases it.

11.2 Implications for the CKM matrix unitarity

Table 11.2: The table shows the relative (compared to the current PDG fit) Ke3 branching ratio calculated assuming CKM matrix unitarity and following prescription of [1]. Errors are connected with the uncertainty of the V_{ud} value used and of the $f_+(t)$ form-factor slope, and its value at the zero momentum transfer.

$\lvert V_{ud}\rvert$ value	Obtained from	$\frac{BR(Ke3)_{CKM}}{BR(Ke3)_{PDG}}$
0.9740 ± 0.0005	Superallowed Nuclear Beta Decays [8]	(1.053 ± 0.027)
0.9740 ± 0.0010	Superallowed Nuclear Beta Decays [2]	(1.053 ± 0.044)
0.9728 ± 0.0012	Neutron Decays Average [2]	(1.101 ± 0.052)
0.9735 ± 0.0012	Neutron and Beta Decays Average [2]	(1.073 ± 0.052)
0.9713 ± 0.0013	New Neutron Decays Result [9]	(1.161 ± 0.056)

Table 11.2 repeats the one in the beginning of the thesis and shows the value of the Ke3 branching ratio inferred from CKM matrix unitarity for the values of the V_{ud} element measured or estimated in different ways. The ratio of our inferred Ke3 branching ratio relative to the PDG fit is

$$\frac{BR(K^+ \to \pi^0 e^+ \nu)}{BR(K^+ \to \pi^0 e^+ \nu)_{PDG}} = (1.071 \pm 0.004_{stat} \pm 0.018_{sys} \pm 0.007_{norm}) \tag{11.5}$$

One can see that our result agrees well with the unitarity predictions based on both superallowed nuclear decay, and the neutron decay V_{ud} results. The only disagreement (of about 1.5 standard deviations) is with the recent V_{ud} result from the neutron decays[9].

11.3 Conclusions

A new high statistics $K^+ \to \pi^0 e^+ \nu$ branching ratio measurement was performed in the E865 experiment at the Brookhaven National Laboratory. The sample of ≈70,000 Ke3 events was collected in 1998. The E865 apparatus allowed only for a relative branching ratio measurement. We chose to use the mix of the following three kaon decays as the normalizer: $K^+ \to \pi^+ \pi^0$, $K^+ \to \pi^0 \mu^+ \nu$, and $K^+ \to \pi^+ \pi^0 \pi^0$.

The relative contribution of the decay modes to the mix was determined by their acceptances.

As the statistical accuracy of the result was small (0.4%), the estimate of the systematic uncertainty proved to be the largest challenge in the analysis. The final systematic error was estimated to be 1.8%. The two most significant contributions to the error were connected with the disagreement between the data and Monte Carlo in the distributions of the vertical coordinate/angle and of the momentum of the tracks. While I could not definitively determine the sources of these two discrepancies, connection of both of them with the spectrometer might be an indication of some residual problems connected with the spectrometer magnet field map, and/or PWC alignment.

The validity of our systematic error estimate was supported by our estimate of the $BR(K^+ \to \pi^+\pi^+\pi^-)/Kdal$ ratio which was more sensitive to systematic uncertainty sources, but differed from the Particle Data Group (PDG) prediction by only 1%.

An additional set of the Ke3 data collected earlier (in 1997) by E865 under different experimental conditions was used as a consistency check, and yielded a result different by only 0.6% from the one obtained from the 1998 data. While the vertical coordinate/angle discrepancy was observed in 1997 as well as in 1998, the momentum discrepancy was very different in the 1997 analysis. The fact that for the 1998 data both the PWC alignment and magnetic field map were calibrated in a different way than for 1997 indicates that the momentum distribution discrepancy might be connected with the spectrometer calibration.

The 0.6% difference in results between the two independent sets of data, and the estimated $BR(K^+ \to \pi^+\pi^+\pi^-)/KDAL$ agreement with the PDG prediction confirmed our confidence in the 1998 result systematic error estimate, and hence, in the result itself.

The E865 result for the $BR(K^+ \to \pi^0 e^+\nu)/KDAL$ is

$$\begin{aligned}
\frac{BR(K^+ \to \pi^0 e^+\nu)}{KDAL} &= 0.1998 \pm 0.0008_{stat} \pm 0.0036_{sys} \qquad (11.6)\\
KDAL &= 0.990 \times BR(K^+ \to \pi^+\pi^0)\\
&+ \; 0.990 \times BR(K^+ \to \pi^0\mu^+\nu)\\
&+ \; 0.995 \times BR(K^+ \to \pi^+\pi^0\pi^0)
\end{aligned}$$

Using the PDG values for the branching ratios in $KDAL$, one can infer that $BR(K^+ \to \pi^0 e^+\nu) = (5.16 \pm 0.02_{stat} \pm 0.09_{sys} \pm 0.04_{norm})\%$, where the last error comes from the uncertainties of the normalizer branching ratio values. This result is different by about 3 standard deviations from the PDG fit ($BR(K^+ \to \pi^0 e^+ \nu)_{PDG} = (4.82 \pm 0.06)$[2]).

The $K^+ \to \pi^0 e^+ \nu$ branching ratio inferred from the assumption of the CKM matrix unitarity is larger than the current PDG fit value by 5-16% (depending on the values of the V_{ud} matrix element used). While our result significantly reduces the discrepancy between the measured and the predicted (from the CKM matrix unitarity) $K^+ \to \pi^0 e^+ \nu$ branching ratio, it introduces the discrepancy with the previous $K^+ \to \pi^0 e^+ \nu$ branching ratio measurements, as well as with the measured branching ratio of the neutral Ke3 decay.

BIBLIOGRAPHY

BIBLIOGRAPHY

[1] H. Leutwyler, M. Ross, Z. Phys. C **25**, 91 (1984)

[2] D.E. Groom *et al.*, Eur. Phys. J. C **15**, 1 (2000)

[3] D. Griffiths, “Introduction to elementary particles”, Harper & Row, (1987)

[4] Q. Ho-Kim and P. Xuan Yem, “Elementary particles and their interactions”, Springer, (1999)

[5] V.V Barmin *et al.*, SJNP **45**, 62 (1987)

[6] Super-Kamiokande and Kamiokande Collaborations, talk at NEUTRINO98 (Takayama, Japan June 4-9, 1998), Nucl. Phys. Proc. Suppl. **77**, 123 (1999)

[7] Q.R. Ahmad *et al.*, Phys. Rev. Lett. **89**, (2002)

[8] J.C. Hardy and I.S. Towner, talk at WEIN98 (Santa Fe, June 14-21, 1998) and nucl-th/9809087

[9] H. Abele *et al.*, Phys. Rev. Lett. **88**, (2002)

[10] M. Amodello, R. Gatto, Phys. Rev Lett. **13**, 264 (1964)

[11] J. Bijnens *et al.*, in progress

[12] V. Cirigliano *et al.*, Eur. Phys. J. C **23**, 121 (2002)

[13] S.A. Akimenko *et al.*, Phys. Lett. **B259**, 225 (1991)

[14] R.J. Tesarek, Talk given at American Physical Society (APS) Meeting of the Division of Particle and Fields (DPF99), Los Angeles, CA, 5-9 Jan., 1999, hep-ex/9903069

[15] S. Shimizu *et al.*, Phys. Lett. **B495**, 33 (2000)

[16] I.V. Ajinenko, *et al.*, IHEP 2002-006, Protvino 2002, hep-ex/0202061

[17] D. Haidt, Phys. Rev. **D3**, 10 (1971)

[18] P.W. Lucas, H.D. Taft, W.J. Willis, Phys. Rev. **D8**, 727 (1973)

[19] D. Bergman, Ph. D. Thesis, Yale University, New Haven, 1997

[20] S. Pislak, Ph. D. Thesis, University of Zurich, 1997

[21] R. Appel, *et al.*, Nucl. Instr. and Meth. A **479**, 349 (2002)

[22] PCOS4: Proportional Chamber operating system, LeCroy Corp., Chestnut Ridge, NY 10977, USA; see http://www.lecroy.com/lrs/dsheets/pcos4.htm

[23] I.M. Bassett, *et al.*, Prog. Opt. **27**, 161 (1989)

[24] K. Abe, *et al.*, Nucl. Instr. and Meth. A **300**, 501 (1991)

[25] G.S. Atoyan, *et al.*, Nucl. Instr. and Meth. A **320**, 144 (1992)

[26] S. Pislak, "KAY, E865 Monte Carlo", E865 Internal Note, unpublished.

[27] R. Brun, *et al.*, "GEANT, Detector Description and Simulation Tool", CERN, Geneva (1994)

[28] J. Sandweiss, I.O. Skillicorn and M.S. Webster, "BETRAF, A program for ray tracing through a magnetic lens system.", 1962, 1967, Updated by H.N. Brown (1968, 1969, 1970, 1978, 1980).

[29] J. Bijnens, G. Ecker, J. Gasser, Nucl. Phys. **B396**, 81 (1993)

[30] K.O. Mikaelian and J. Smith, Phys. Rev. **D5**, 1763 (1972)

[31] J.B. Birks, "The theory and practice of scintillation counting", Pergamon Press, 1964

[32] C.N. Chou, "The Nature of saturation effect of fluorescent scintillators", Phys. Rev. **87**, 905 (1952)

[33] R.L. Craun, "Analysis of response data for several organic scintillators", Nucl. Instr. and Meth. **80**, 239 (1972)

[34] B.E. Lautrup, Phys. Rev. **D**, 1122 (1971)

[35] I.H. Chiang, *et al.*,Phys. Rev. **D8**, 1254 (1972)

Appendix

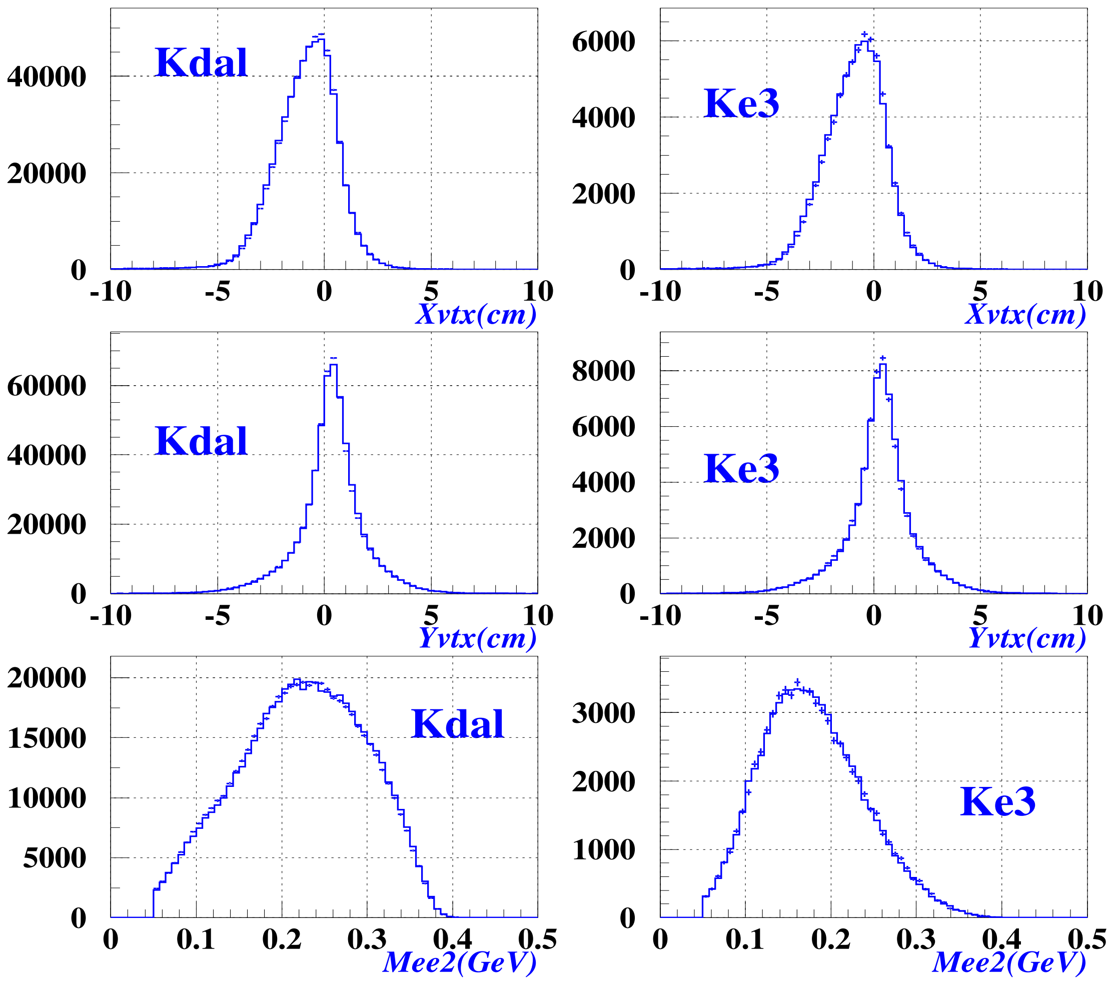

Figure A.1: Comparison between data and Monte Carlo for the X and Y positions of the reconstructed vertex, and for the invariant mass of the e^- and the second positive track (e^+ for the Ke3 and $(\pi/\mu)^+$ for the Kdal). The invariant mass was called Mee2, because for its calculation, the second positive track was considered to have an electron mass. Histograms represent Monte Carlo, while points with errors represent data.

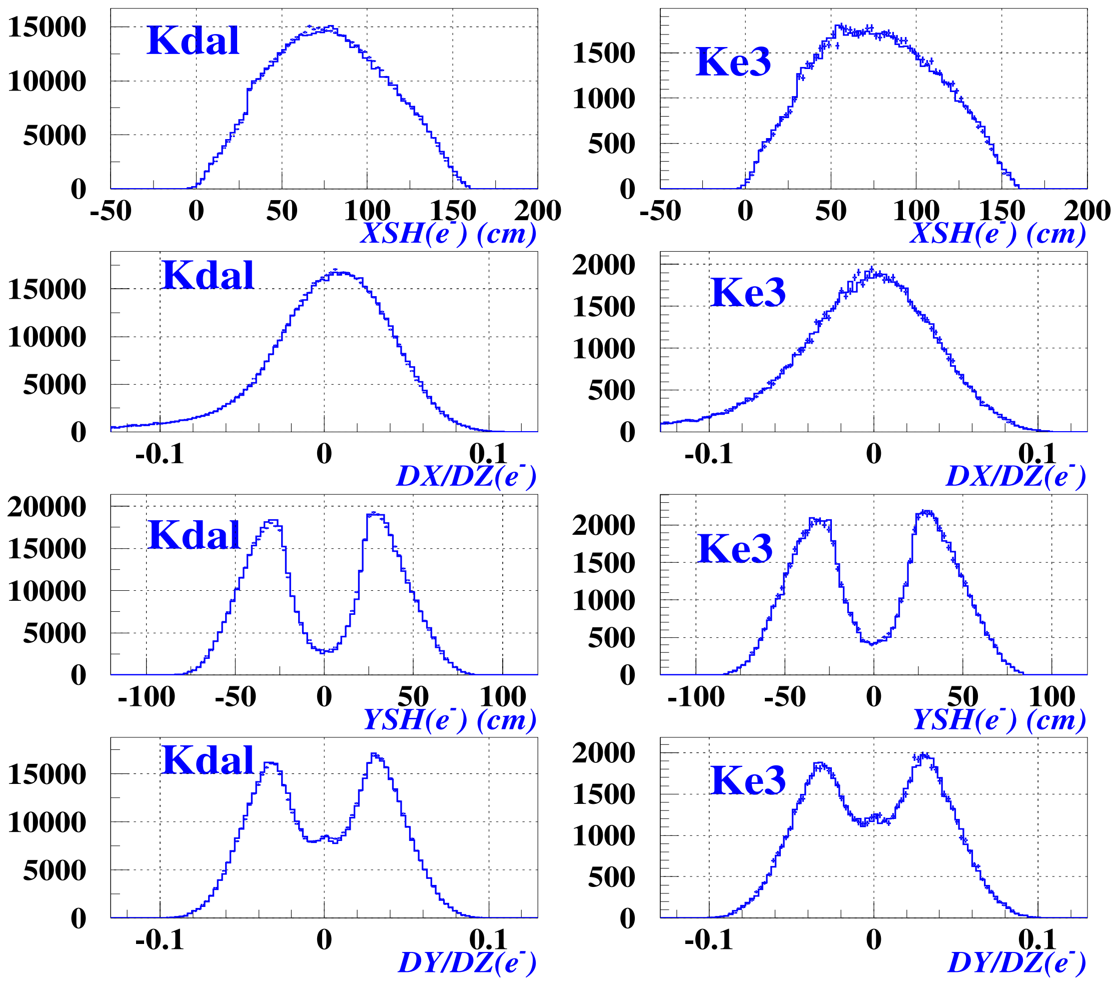

Figure A.2: Comparison between data and Monte Carlo for the X and Y positions, and DX/DZ and DY/DZ angles of the reconstructed e^-. Positions and angles were measured at the calorimeter plane. Histograms represent Monte Carlo, while points with errors represent data.

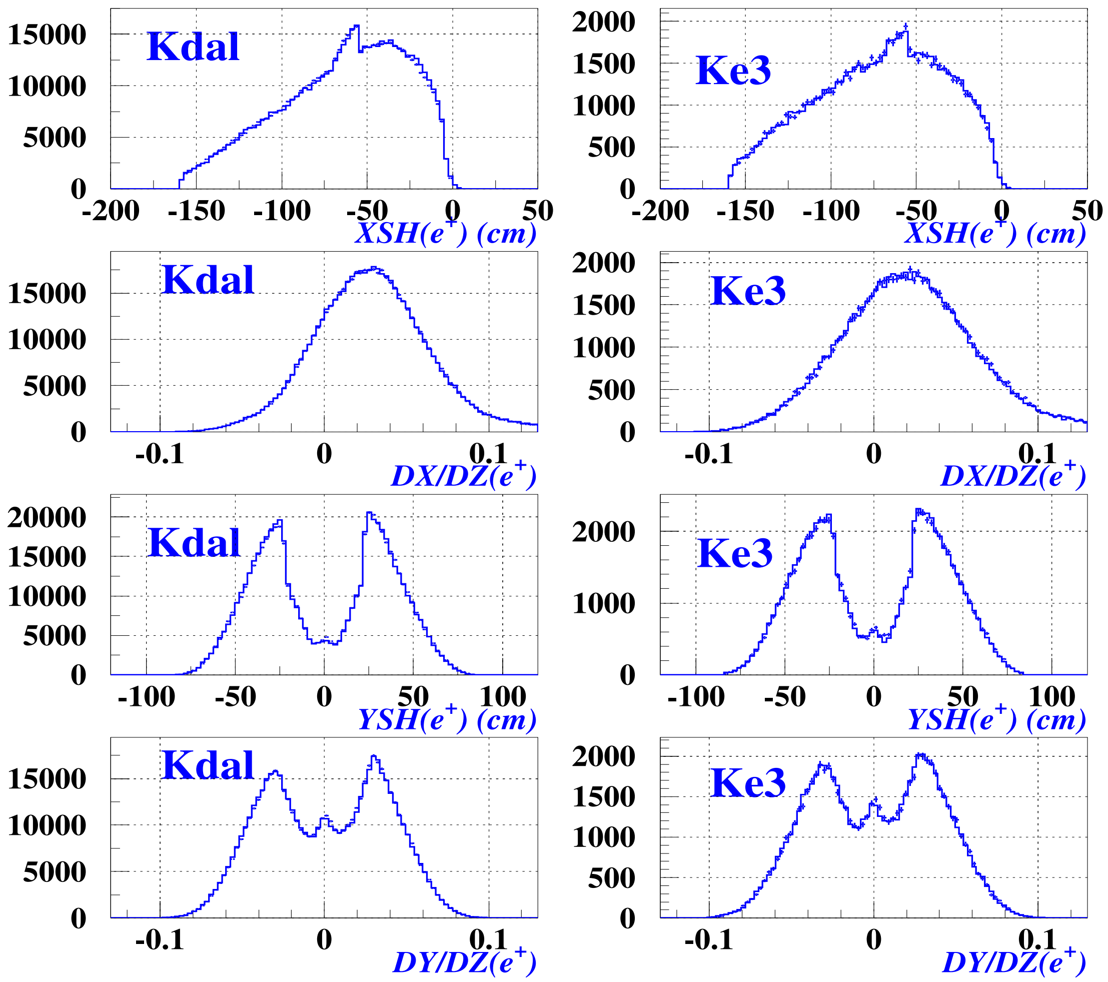

Figure A.3: Comparison between data and Monte Carlo for the X and Y positions, and DX/DZ and DY/DZ angles of the reconstructed e^+ (the one from the $\pi^0 \to e^+e^-\gamma$ decay). Positions and angles were measured at the calorimeter plane. Histograms represent Monte Carlo, while points with errors represent data.

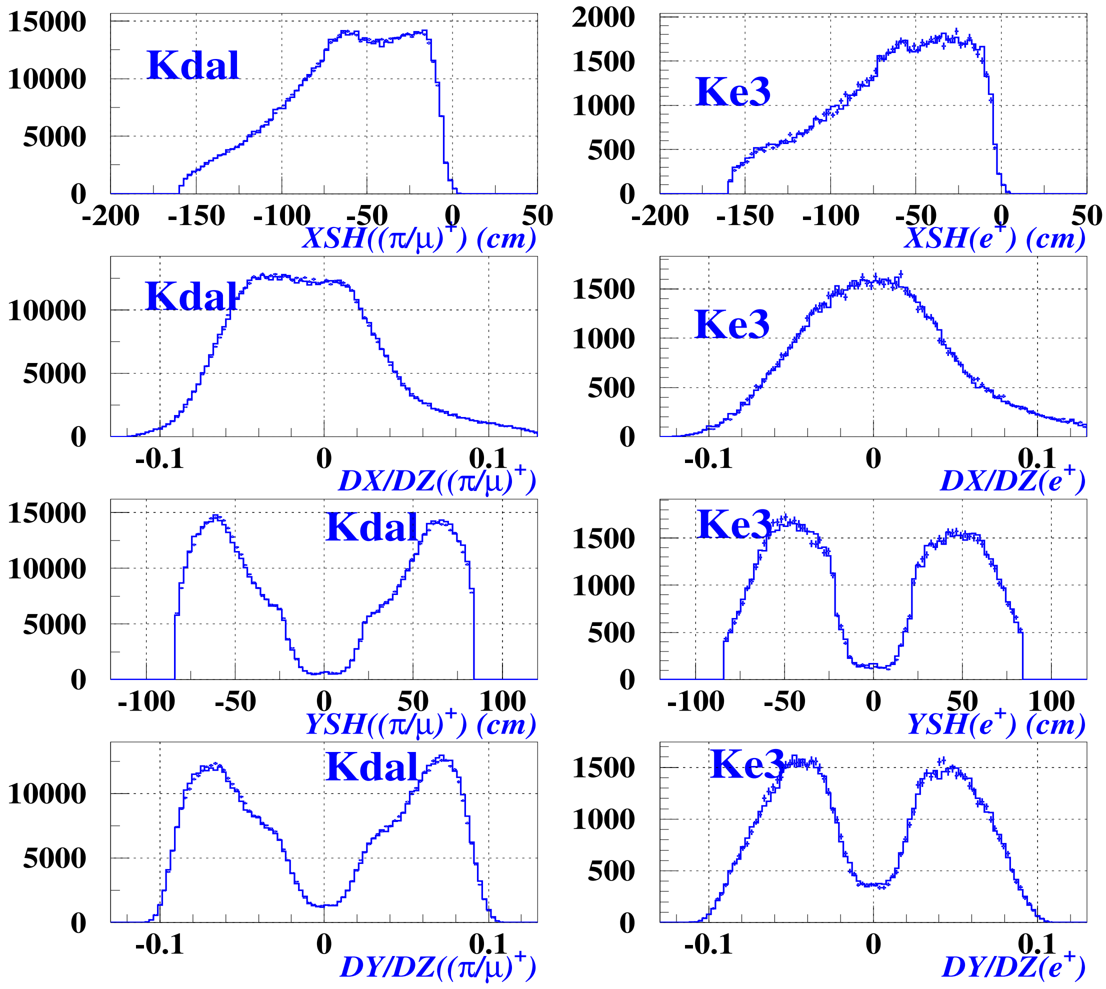

Figure A.4: Comparison between data and Monte Carlo for the X and Y positions, and DX/DZ and DY/DZ angles of the reconstructed second positive track (e^+ for the Ke3 and $(\pi/\mu)^+$ for the Kdal). Positions and angles were measured at the calorimeter plane. Histograms represent Monte Carlo, while points with errors represent data.

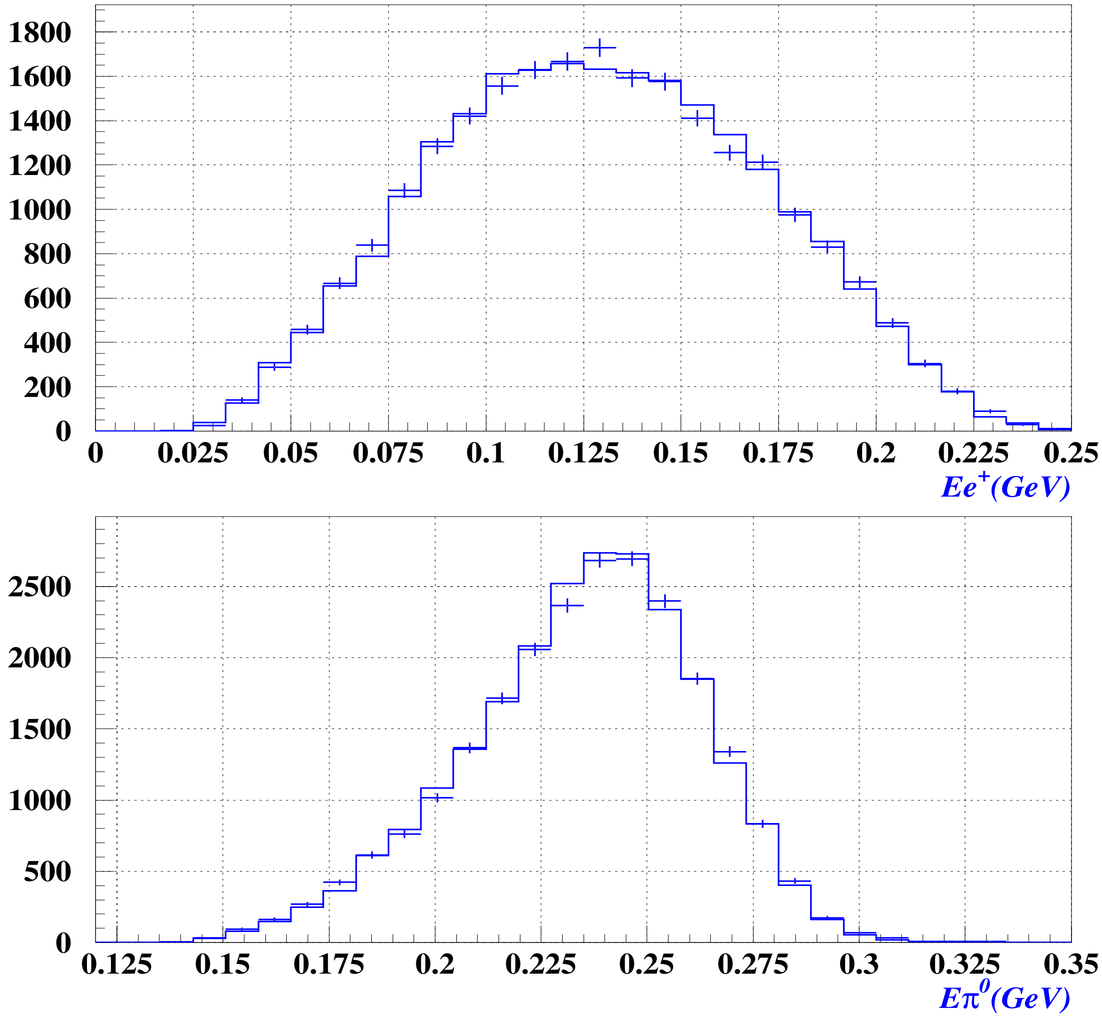

Figure A.5: Comparison between data and Monte Carlo for the reconstructed Ke3 positron (upper) and π^0 (lower plot) energies in the rest frame of the kaon. Histograms represent Monte Carlo, while points with errors represent data.

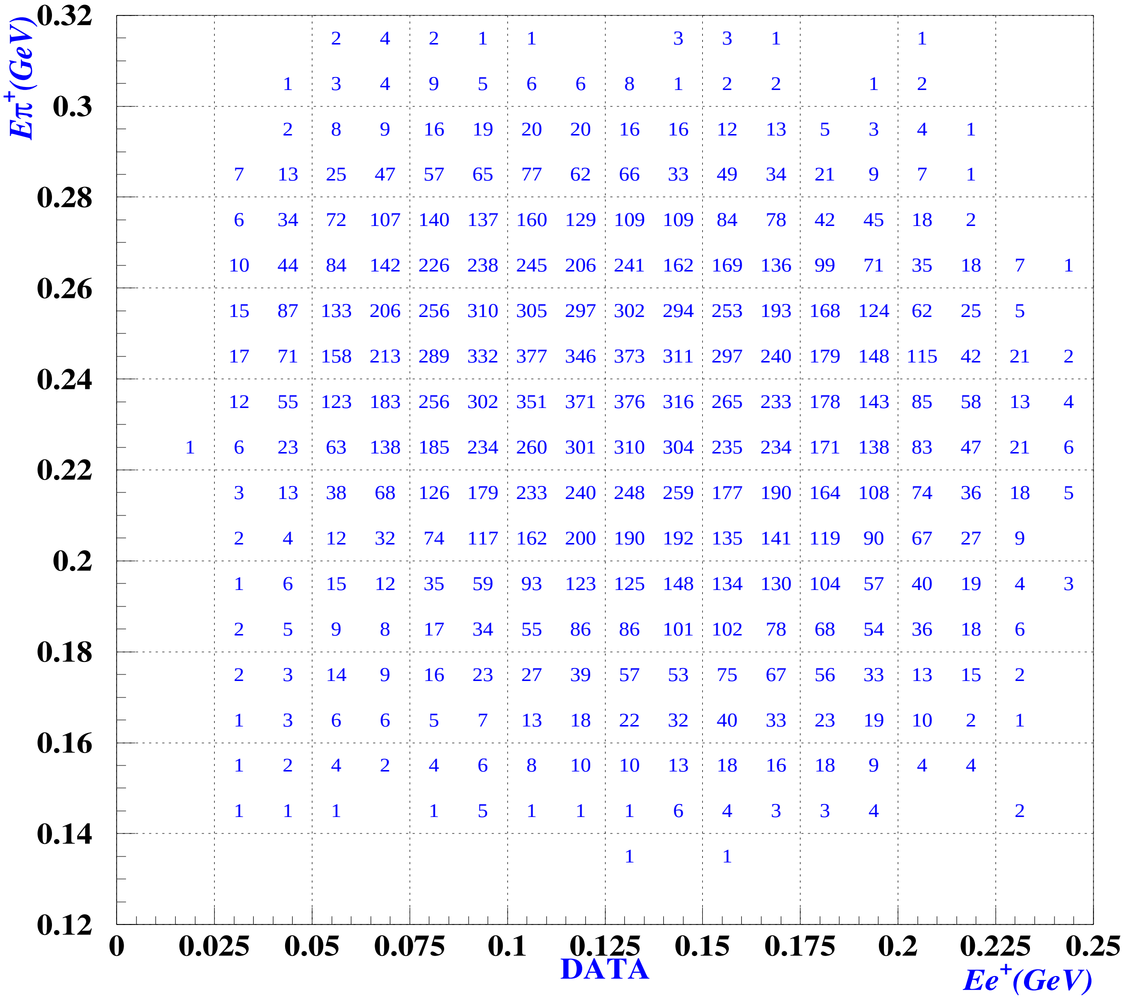

Figure A.6: The reconstructed (from the collected data) two-dimensional Ke3 phase-space distribution in the rest frame of the kaon.

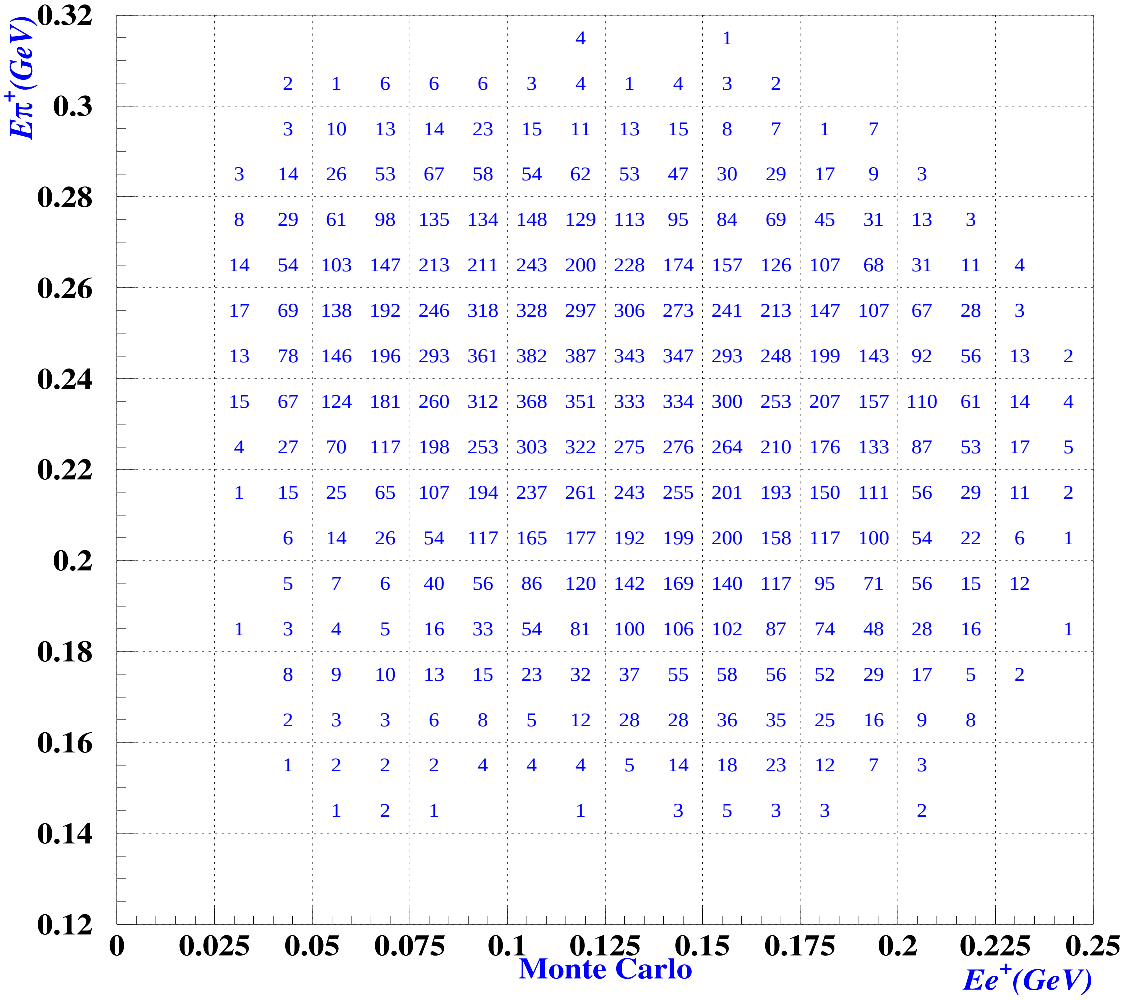

Figure A.7: Two-dimensional Ke3 phase-space distribution in the rest frame of the kaon reconstructed from the Monte Carlo simulation and normalized to have the same total number of events as in the selected data sample (Figure A.6).

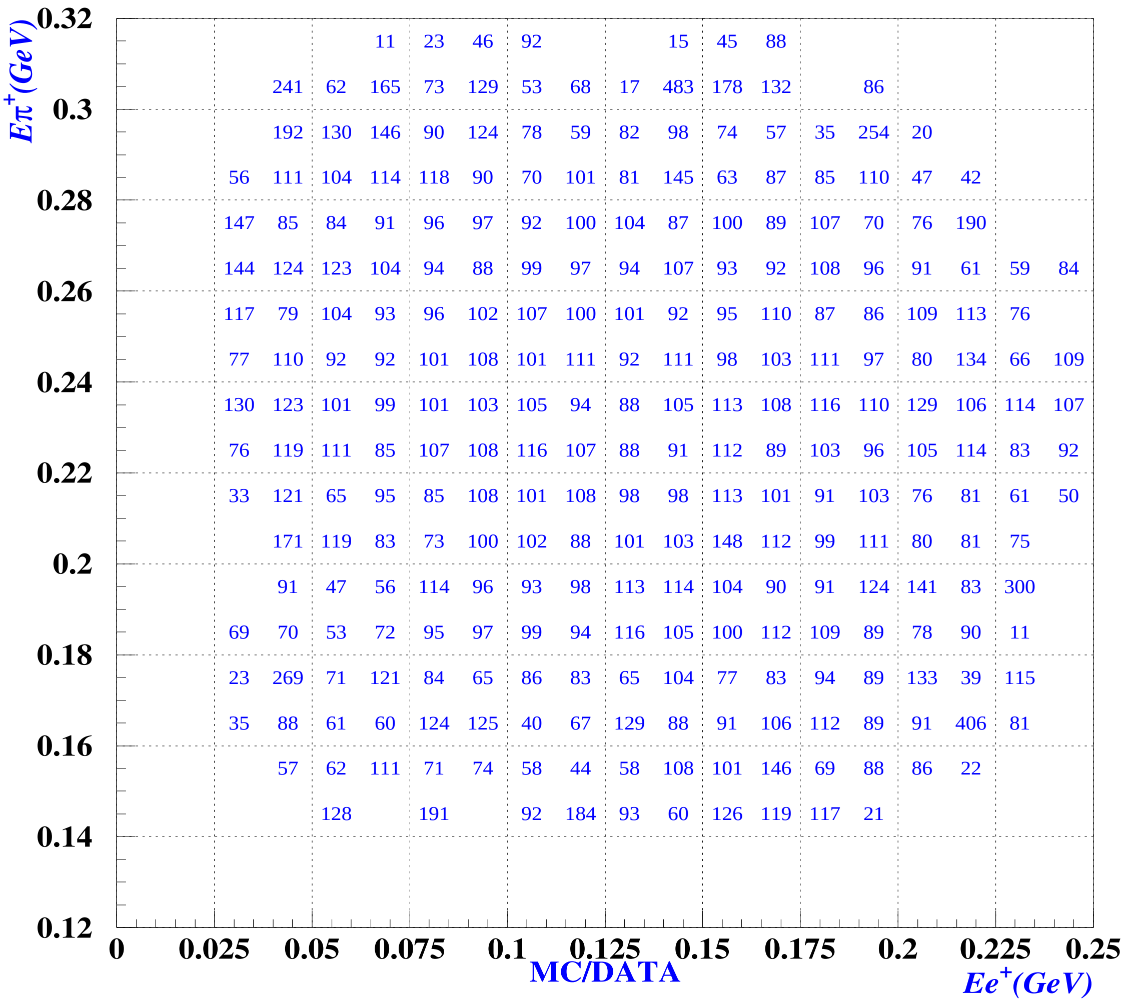

Figure A.8: Bin-by-bin ratio of the Monte-Carlo and data two-dimensional reconstructed Ke3 phase-space distributions (in percent). Statistical uncertainty of the ratio in each bin is determined by the number of data events in the bin (Figure A.6).